

# Global Biogeochemical Cycles®

## RESEARCH ARTICLE

10.1029/2022GB007475

### Key Points:

- Three decades of inverse modeling of meridional and vertical transports of  $C_{\text{anth}}$  in the Atlantic
- The change in the net transport of  $C_{\text{anth}}$  appear from the variability in upper layers
- Overturning and diffusion contribute almost equally to the interior storage of  $C_{\text{anth}}$

### Supporting Information:

Supporting Information may be found in the online version of this article.

### Correspondence to:

V. Caínzos,  
veronica.cainzos@ulpgc.es





### Citation:

Caínzos, V., Velo, A., Pérez, F. F., & Hernández-Guerra, A. (2022). Anthropogenic carbon transport variability in the Atlantic Ocean over three decades. *Global Biogeochemical Cycles*, 36, e2022GB007475. <https://doi.org/10.1029/2022GB007475>

Received 26 MAY 2022

Accepted 4 NOV 2022

## Anthropogenic Carbon Transport Variability in the Atlantic Ocean Over Three Decades

Verónica Caínzos<sup>1</sup> , Antón Velo<sup>2</sup> , Fiz F. Pérez<sup>2</sup> , and Alonso Hernández-Guerra<sup>1</sup> 

<sup>1</sup>Unidad Océano y Clima, Instituto de Oceanografía y Cambio Global, IOCAG, Universidad de Las Palmas de Gran Canaria, ULPGC, Unidad Asociada ULPGC-CSIC, Canary Islands, Spain, <sup>2</sup>Instituto de Investigaciones Marinas, CSIC, Vigo, Spain

**Abstract** The change in anthropogenic  $\text{CO}_2$  ( $C_{\text{anth}}$ ) in the Atlantic Ocean is linked to the Atlantic Meridional Overturning Circulation (AMOC), that redistributes  $C_{\text{anth}}$  meridionally and in depth. We have employed direct biogeochemical measurements and hydrographic data from the last 30 years, adjusted using inverse models for each decade with both physical and biogeochemical constraints. We then have computed the meridional transports and the vertical transports between two sections at the interphases by advection and diffusion. We have focused on the repeated sections at three latitudes—30°S, 24, and 55°N, dividing the Atlantic into two boxes. We have divided the net transport into upper, deep and abyssal layers, with an upper and abyssal northward transport of  $C_{\text{anth}}$  and a southward component in deep layers. The change in time in the net transports of  $C_{\text{anth}}$  appears to be mainly due to modifications in the transport of upper layers. The lower layer of the AMOC, a combination of deep and abyssal waters, maintain more consistent transports in time. Vertical advection plays an important role in the North Atlantic, exporting  $C_{\text{anth}}$  from upper to deep layers. In the South Atlantic, the newly formed Antarctic Bottom Water exports  $C_{\text{anth}}$  from abyssal to deep layers. The strong gradient in  $C_{\text{anth}}$  concentration at the interphase of upper and deep layers results in a strong vertical diffusion.

**Plain Language Summary** Rising levels of  $\text{CO}_2$  in seawater may affect the calcifying organisms that depend on the balance of different carbon species. Therefore, the amount of anthropogenic carbon ( $C_{\text{anth}}$ ) that is captured by the ocean has been closely monitored. Using hydrographic and biogeochemical observations from a set of oceanographic cruises covering the Atlantic basin for the last three decades, we have built three models to investigate the state and evolution of  $C_{\text{anth}}$  at different depths of the Atlantic Ocean. Those results helped us determine the strength of the meridional circulation of  $C_{\text{anth}}$  in the Atlantic and the importance of vertical fluxes in the sequestering of  $C_{\text{anth}}$  in the ocean.

## 1. Introduction

Human activities have dispersed  $650 \pm 65$  Gt of carbon to the atmosphere since 1850, of which about 30% has been sequestered by the oceans (Friedlingstein et al., 2020; Gruber et al., 2019; Khatiwala et al., 2013), leading to a continuous increase in total inorganic carbon concentration ( $C_T$ ). The rise in  $C_T$  has, in turn, led to a decrease in surface seawater pH of approximately 0.1 from the pre-industrial era to the present, which implies an increase of approximately 30% in hydrogen ion concentration (Doney et al., 2020; Gattuso et al., 2015). This decline in pH leads to a reduction in the saturation state of calcium carbonate and consequently a serious threat to calcareous marine organisms such as pteropods and corals (Doney et al., 2020; Guinotte et al., 2006; Pérez et al., 2018).

The increase in  $C_T$  is very small compared to its concentrations in the ocean (<0.1% per year), so most studies quantify the anthropogenic  $\text{CO}_2$  ( $C_{\text{anth}}$ ) storage rate rather than the  $C_T$  change (Gruber et al., 2019; Khatiwala et al., 2013; Mikaloff Fletcher et al., 2006). The largest  $C_{\text{anth}}$  water column inventories are found in the subpolar North Atlantic (SPNA; Khatiwala et al., 2013; Sabine, Felly, Gruber, et al., 2004). This is due to the combination of (a) convective processes that cause significant ventilation and subduction of  $C_{\text{anth}}$ -enriched surface water into the interior ocean (Sabine, Felly, Gruber, et al., 2004) and (b) a large amount of  $C_{\text{anth}}$  advected by the northward currents from tropical latitudes (Brown et al., 2021; Pérez et al., 2013).

Both processes are embedded in the Atlantic Meridional Overturning Circulation (AMOC), which drives the net upper northward transport of  $C_{\text{anth}}$ -enriched waters throughout the North Atlantic, maintaining a positive correlation between the intensity of the AMOC and the  $C_{\text{anth}}$  storage rate in the SPNA (DeVries et al., 2017; Pérez et al., 2013; Racapé et al., 2018). Deep-ocean ventilation has been largely related to the strength of the AMOC and controls the connection between the time scales of heat uptake and carbon storage (Kersalé et al., 2020). In

© 2022 The Authors.

This is an open access article under the terms of the [Creative Commons Attribution-NonCommercial License](https://creativecommons.org/licenses/by-nc/4.0/), which permits use, distribution and reproduction in any medium, provided the original work is properly cited and is not used for commercial purposes.

the tropical North Atlantic, the rise in  $C_{\text{anth}}$  concentrations in thermocline waters is the main cause of the slight increase of northward  $C_{\text{anth}}$  transport from 1992–1993 to 2010–2011, attenuated by the weakening of the circulation (Hernández-Guerra et al., 2014; Zunino et al., 2015).

Several studies have described the North Atlantic transport, storage and uptake of  $C_{\text{anth}}$ , benefitting from monitoring projects such as the RAPID/MOCHA/WBTS array (hereafter the RAPID array; Cunningham et al., 2007; Johns et al., 2011; McCarthy et al., 2015) and OVIDE (Lherminier et al., 2010; Mercier et al., 2015). Biogeochemical observations and early estimations of  $C_{\text{anth}}$  have been combined with ocean circulation models in inverse schemes to estimate air-sea fluxes,  $C_{\text{anth}}$  storage rate and  $C_{\text{anth}}$  transport in the ocean interior (DeVries, 2014; Gruber et al., 2019; Mikaloff Fletcher et al., 2006).

However, the South Atlantic has not been subject to such an extensive study, despite representing the region of the Atlantic Ocean with a higher exchange with other ocean basins. The upper limb of the AMOC in the South Atlantic is connected via Drake Passage to the Pacific Ocean, and via the Agulhas Current System to the Indian Ocean. Evans et al. (2017) evaluated the  $C_{\text{anth}}$  divergence in the South Atlantic and found that the  $C_{\text{anth}}$  that entered the South Atlantic through Drake Passage was then exported northwards and eastwards, associated with the Antarctic Circumpolar Current and, to a lesser extent, the Agulhas Current System. Thus, this interbasin exchange supplies the Atlantic and the Indian sector of the Southern Ocean with  $C_{\text{anth}}$ . Decadal variability in  $C_{\text{anth}}$  concentration has been studied at 30°S, with a net increase in  $C_{\text{anth}}$  concentration in Sub Antarctic Mode Waters and Antarctic Intermediate Waters, mainly west of the Mid-Atlantic Ridge (Murata et al., 2008).

In this study, we provide a detailed perspective on the transport of  $C_{\text{anth}}$ , both from observational and inverse modeling circulation data, and attending to the different components of the meridional circulation, to assess changes for the last three decades, providing a regional perspective. We have also evaluated the contribution of the different water masses that occupy the whole Atlantic basin, using the best available information for different time periods. Thus, we propose a basin solution to anthropogenic transports obtained from hydrographic observations and based on the mass transports determined with inverse models for the last 30 years of the Atlantic Ocean (Caínzos et al., 2022).

## 2. Data and Methods

### 2.1. Hydrographic Data

We have selected zonal hydrographic sections for the last 30 years and grouped them by decade (1990–1999, 2000–2009, and 2010–2019). These sections occupy the Atlantic basin, from 45°S to 55°N in the first decade and from 30°S to 55°N for the last two decades (Figure 1). Three sections appear in all three decades: A10 (30°S), A05 (24°N) and AR07W + AR07E (55°N).

Biogeochemical data for most of the cruises, including water sample values for oxygen, nutrients (nitrate, phosphate, silicate), alkalinity ( $A_T$ ),  $C_T$ , and pH, have been obtained from the Global Ocean Data Analysis Project version 2.2021 (GLODAPv2; Key et al., 2015; Lauvset et al., 2021; Olsen et al., 2016). The data included in GLODAPv2 are subject to primary and secondary quality control to correct the measurements. Sections A02 1993 (47°N), AR07W 1990 (55°N) and AR07E 1991 (58°N) are not available in GLODAPv2, so we have used the biogeochemical data provided by the CLIVAR and Carbon Hydrographic Data Office (CCHDO). Data for sections AR07W 2014 (55°N) and AR07E 2014 (58°N) were recovered from the British Oceanographic Data Centre (BODC) with measurement values for  $A_T$  and  $C_T$ . Variables not provided by these datasets were filled with the Bayesian neural network CANYON-B (Bittig et al., 2018), solving for nutrient concentrations (nitrate, silicate and phosphate),  $A_T$  and  $C_T$  using temperature, salinity, oxygen concentration, and geolocation data. Table S1 in Supporting Information S1 summarizes this information.

Biogeochemical samples naturally underrepresent the water column, typically with a maximum of 24 samples in the water column. We have interpolated all the available biogeochemical parameters every 2 dbar (to mirror the resolution of the hydrographic CTD casts) for each station using a 2D linear interpolation on scattered data employing a Delaunay triangulation, with a nearest extrapolation method. We have interpolated in a neutral density ( $\gamma^\theta$ ) framework, with the computed values of  $\gamma^\theta$  for each 2 dbar, allowing to interpolate along the interphase of the water masses and distributing the deeper values more evenly.

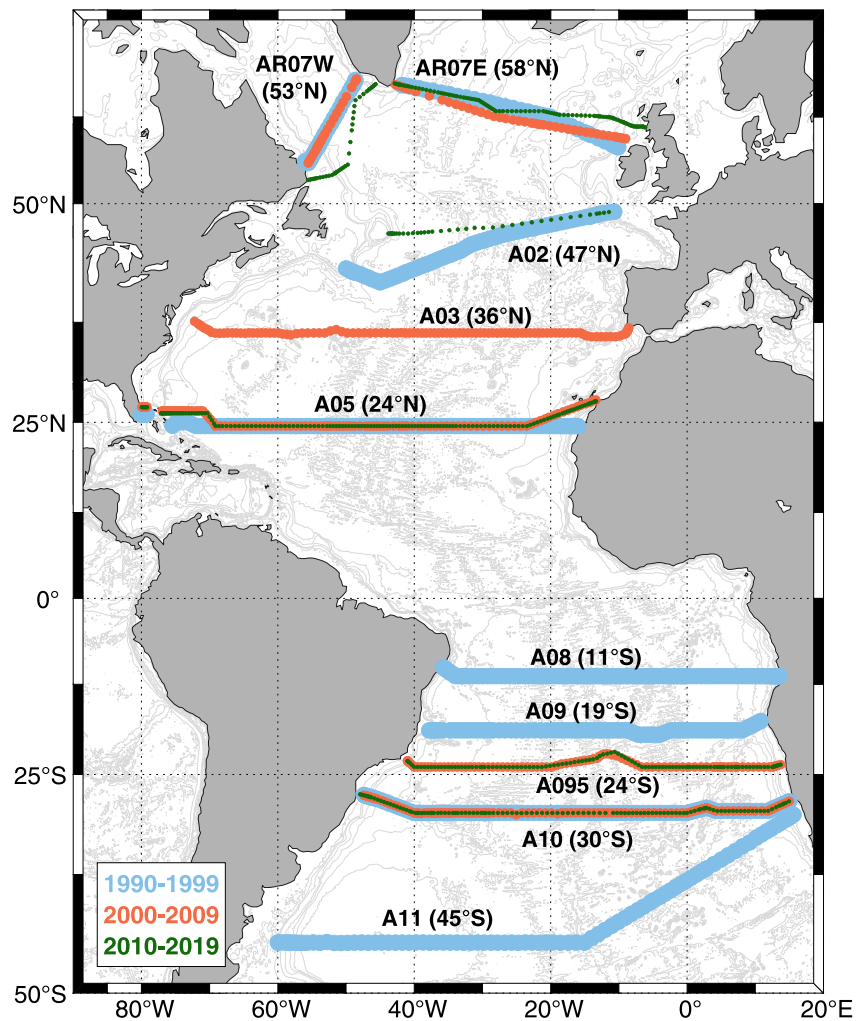


**Figure 1.** Map of the zonal sections included in each decade for the inverse model. Each section is accompanied by its world ocean circulation experiment name and its nominal latitude (between parenthesis), and the colors represent each decade, blue for 1990–1999, orange for 2000–2009, and green for 2010–2019. Three sections have been repeated in every decade (A10—30°S, A05—24°N, AR07W and AR07E—55°N).

## 2.2. Inverse Model

The initial geostrophic estimation of mass transport for each station pair is computed assuming a null velocity at a reference level. But this level of no motion, chosen as the interphase of water masses flowing in opposite directions, has a velocity different from zero. Inverse models can solve for these velocities at the reference level for each station pair, applying constraints and uncertainties, mainly related to mass conservation (Ganachaud & Wunsch, 2000; Hernández-Guerra et al., 2019; Wunsch, 1996). Caínzos et al. (2022) constructed three inverse models, one for each of the last decades, imposing mass conservation for each box between adjacent sections, and for each single section, mass and salinity content were conserved, on top of regional constraints of independent measurements and topographic features.

Building on their methodology, we have constructed three similar inverse models combining the sections for each decade, in which we have included constraints for the conservation of oxygen, nitrate, silicate and phosphate (Fontela et al., 2019; Maze et al., 2012). For each of these biogeochemical variables, we have applied a balance for each layer of neutral density between adjacent sections. Since these are not conservative variables and there are sources and sinks at play, we have included an input of oxygen from the atmosphere in the first layer and a consumption rate of oxygen for each layer of the water column. Therefore, using these initial estimates, the method allows for an adjustment on both the oxygen production in the surface layers and its consumption along

the water column. For nitrate, phosphate and silicate, we have applied the Redfield ratio used previously in similar studies ( $-150 \text{ O}_2$ :  $16 \text{ N}$ :  $1 \text{ P}$ :  $16 \text{ Si}$ ; Anderson, 1995; Maze et al., 2012) to the consumption rate of oxygen for each layer of the water column.

The estimates of  $\text{O}_2$  surface flux are computed as the average from five different Earth System Models (CESM, CCSM, MOM4, NEMO-Control and NEMO-WSTIR) and a semi-empirical data set based on indirect observations (Morgan et al., 2021). For each box between two sections, we have obtained an oxygen flux for the whole area.

The concentration of dissolved oxygen and nutrients changes in the water column, affected not only by the pattern of circulation but also due to biogeochemical processes. Therefore, we have included a term to integrate the changes in tracer concentrations in time in each layer of the water column. We have used as a priori estimates the rates of oxygen consumption obtained by Stendardo and Gruber (2012) that are compatible with the model outputs from NorESMO1C and then applied the Redfield ratio to obtain the sinks and sources of nitrate, silicate and phosphate.

The combination of all these equations conforms an underdetermined system, which can be solved using the Gauss-Markov estimator. The entire matrix system can be found in Text S1 in Supporting Information S1. This method provides an estimate from all the possible solutions of the system that minimizes the error with the real value using the initial and noise information. It also gives a measure of the uncertainties for the solution and the noise (Wunsch, 1996), which is described in more detail in Text S2 in Supporting Information S1. Sensitivity tests were also carried out to determine the effect of different parameters in the configuration of the inverse model and the concentration of  $C_{\text{anth}}$  at the surface (Text S3 in Supporting Information S1).

The results for mass, heat and freshwater transports are not different compared to the results from the previous inverse model without considering the biogeochemical equations (Caínzos et al., 2022). However, the conservations of oxygen, nitrate, silicate and phosphate provide adjusted values after the model that are in balance. As a consequence, these added biogeochemical equations improve the determination of the biological pump, constraining the flux of  $C_T$ , and, therefore, of  $C_{\text{anth}}$  (Tables S2–S10 in Supporting Information S1). One of the main issues when obtaining results from inverse models with multiple sections is how accurately they represent the average circulation of the decade. Composing box models with several hydrographic sections result in circulation schemes that can help average out the local and small-scale variability that is found on a single hydrographic section (Ganachaud & Wunsch, 2000; Lumpkin & Speer, 2007; Macdonald & Wunsch, 1996; Reid, 1989, 1994).

### 2.3. $C_{\text{anth}}$ Estimations

#### 2.3.1. $C_{\text{anth}}$ Concentration

$C_{\text{anth}}$  concentration cannot be measured in the ocean, thus it is derived from other direct water sample values. There are several methods of  $C_{\text{anth}}$  computation, all based on two different techniques. These methods rely on the assumption that the ocean is in steady state. The first is based on back calculation, with methodologies such as  $\Delta C^*$  (Gruber et al., 1996), tracer combining oxygen, inorganic carbon and total alkalinity (TrOCA; Touratier et al., 2007) or  $\varphi C_T^0$  (Pérez et al., 2008; Vázquez-Rodríguez, Touratier, et al., 2009). The second technique is based on transit time distributions (Waugh et al., 2006).

In this study, we have computed  $C_{\text{anth}}$  using the back-calculation  $\varphi C_T^0$  method (Guallart et al., 2015; Pérez et al., 2008; Ríos et al., 2012; Vázquez-Rodríguez et al., 2012; Vázquez-Rodríguez, Padin, et al., 2009; Vázquez-Rodríguez, Touratier, et al., 2009), with an overall uncertainty of  $\pm 5.2 \mu\text{mol kg}^{-1}$ . This method is based on the same principles as the  $\Delta C^*$  method (Gruber et al., 1996) with some improvements. To determine the amount of  $C_{\text{anth}}$  in a parcel of water, the method back-calculates the  $C_T$  of a water sample to its initial (or preformed)  $C_T$  concentration when it was last at the surface layer, based on the changes in  $A_T$ , apparent oxygen utilization, salinity and potential temperature. This method, contrarily to the  $\Delta C^*$  method, considers the temporal variation of the  $\text{CO}_2$  air-sea disequilibrium, and uses sub-surface layer data of the Atlantic as the reference for its parameterizations (Matear et al., 2003; Thomas & Ittekkot, 2001), removing the seasonality present on the surface layer, thus making these parameterizations more representative of the water mass formation conditions. This approach delivers better results in areas of cold waters subject to strong and complex mixing processes. The back-calculation  $\varphi C_T^0$  method has been widely used to compute  $C_{\text{anth}}$  and has provided consistent results

with other back-calculation methods (Brown et al., 2021; Guallart et al., 2015; Vázquez-Rodríguez, Touratier, et al., 2009; see also Figure S1a in Supporting Information S1).

### 2.3.2. Transport of $C_{\text{anth}}$

The transport of any property ( $T_{\text{Prop}}$ ) is computed for each pair of consecutive hydrographic stations and between two neutral density interphases as

$$T_{\text{Prop}} = \iint C_{\text{Prop}} \rho \text{ vel } dx dy_n,$$

where  $C_{\text{Prop}}$  is the property concentration,  $\rho$  is the in situ density, vel is the velocity perpendicular to the section and  $dx dy_n$  is the area over which the computation occurs, considering the distance between stations and the width of each vertical level, respectively.

This initial transport of  $C_{\text{anth}}$  is adjusted with the velocities at the reference level for each station pair obtained from the inverse model solution. Positive values of meridional transport refer to northward fluxes and negative to southward. In a vertical framework, positive values are upward (or toward the atmosphere, release or efflux) and negative values are downward (toward the ocean, uptake).

To understand the underlying variability in  $C_{\text{anth}}$  concentration and remove the effect of the variation in mass transport, we have computed the transport-weighted  $C_{\text{anth}}$  (TW  $C_{\text{anth}}$ ) concentration (in  $\mu\text{mol kg}^{-1}$ ). For water masses flowing in the same direction, we can obtain TW  $C_{\text{anth}}$  as the ratio between  $C_{\text{anth}}$  and mass transport.

The vertical transport resulting from the diffusion of  $C_{\text{anth}}$  was computed using a diffusion coefficient of  $1.1 \text{ cm}^2 \text{ s}^{-1}$  for the whole basin and all depths, obtained as the average value at the interphase between upper and deep layers from the diffusion coefficients ( $\kappa_z$ ) computed for each box between adjacent sections. The diffusion processes included in  $\kappa_z$  are the remaining changes in vertical heat transport after compensating the horizontal imbalance in mass with a vertical transport associated to mass advection (Caínzos et al., 2022; Hernández-Guerra & Talley, 2016; Hogg et al., 1982; Morris et al., 2001; Munk, 1966). This diffusion coefficient was then multiplied by the area and by the vertical derivative at the interphase between different layers of the  $C_{\text{anth}}$  concentration times density.

### 2.3.3. Storage Rate of $C_{\text{anth}}$

To determine the amount of  $C_{\text{anth}}$  stored in  $\text{PgC yr}^{-1}$  (or  $\text{kmol s}^{-1}$ ) in each cell between adjacent sections and each two neutral density interphases, we have used, primarily, the storage rates of Gruber et al. (2019), supplemented with the inventories of Sabine, Feely, Gruber, et al. (2004). Both datasets have quantified the oceanic sink for  $C_{\text{anth}}$  over the period 1994 to 2007 for the former and 1800 to 1994 for the latter.

The storage rates were normalized by the volume of each box and then the value for each decade was computed. Tanhua et al. (2006) found that  $C_{\text{anth}}$  is in a transient steady state (TSS) in the North Atlantic by comparing observed changes in  $C_T$  and CFC fields with those predicted from an eddy-permitting ocean circulation model. This implies that the increase of  $C_{\text{anth}}$  concentration with time is related to the surface concentration. Changes in  $C_{\text{anth}}$  for a given time period can be calculated by applying the exponential expression  $C_t^0 = Ae^{\lambda t}$ , that reconstructs the history of atmospheric  $\text{CO}_2$  and  $C_{\text{anth}}$  since the Industrial Revolution. The rate of change of  $C_{\text{anth}}$  is included in the factor  $\lambda$  ( $\text{yr}^{-1}$ ), with an annual increase of 1.9%, based on a 28% increase between 1994 and 2007 (Gruber et al., 2019). The concentrations or the storage rate can be rescaled to the average year for each decade following the expression (Gruber et al., 2019; Steinfeldt et al., 2009):

$$C_{\text{anth}_{t2}} = C_{\text{anth}_{t1}} e^{\lambda(t2-t1)} = C_{\text{anth}_{t1}} (1 + 0.019)^{t2-t1} \quad (1)$$

where  $t1$  is the reference year and  $t2$  corresponds to the midpoint year for each decade (1995, 2005, and 2015). This expression can also be applied to  $C_{\text{anth}}$  transports by obtaining the  $C_{\text{anth}}$  concentration for the desired time and combining it with the mass transport estimates. The storage rates of Gruber et al. (2019) are referred to a  $t1 = 2000.5$  (the midpoint of the 1994–2007 inventory change).

Using the inventory of Sabine, Felly, Gruber, et al. (2004) for 1994 and the change in  $C_{\text{anth}}$  concentration of Gruber et al. (2019) between 1994 and 2007, we can obtain the storage rate for 2007 following the expression:

$$\text{Storage Rate } C_{\text{anth}2007} = 0.019 \cdot (C_{\text{anth}1994} + \Delta C_{\text{anth}2007-1994}) \quad (2)$$

Then, the storage rates can be normalized to the middle of each decade using the TSS expression (Equation 1), with 2007 as reference year. The uncertainties computed for the last decade are described in Text S2 in Supporting Information S1.

In general, we have used values from the Gruber estimate (Equation 1), but we have introduced some adjustments due to the difficulties associated to the methodology of  $\Delta C^* \text{MLR}$  to detect small changes in deep waters (Gruber et al., 2019). We have computed values from the combined inventory of Gruber et al. (2019) and Sabine, Felly, Gruber, et al. (2004) for 2007 (Equation 2), and then normalized to the midpoint of each decade using TSS (Equation 1). If the storage rate from Gruber et al. (2019) exceeded over 50% the combined storage rate, it was replaced by the combined estimation. That is the case of the cells marked with an asterisk in Figure 2. Most of the cells achieved a better  $C_{\text{anth}}$  balance between advection and storage with this replacement.

### 2.3.4. $C_{\text{anth}}$ Uptake

The net budget of  $C_{\text{anth}}$  within each cell, defined between two sections and two neutral density interphases, is the balance between the lateral advection of the meridional  $C_{\text{anth}}$  transport across each section, the storage of  $C_{\text{anth}}$  within the cell and the vertical fluxes of  $C_{\text{anth}}$  (Brown et al., 2021; Pérez et al., 2013; Racapé et al., 2018; Zunino et al., 2015). This vertical flux in the air-sea interphase is the uptake from the atmosphere. We have computed the  $C_{\text{anth}}$  uptake indirectly, inferring it from the other two terms of the balance in each cell.

### 2.3.5. $C_{\text{anth}}$ Components

The total transport of  $C_{\text{anth}}$  can be divided into its components, analogous to methods applied to heat and freshwater transport, attending to the mechanisms of vertical and meridional circulation (Brown et al., 2021; Bryden & Imawaki, 2001; Caínzos et al., 2022; McDonagh et al., 2015). Any property can be defined as a sum of their components, distinguishing between mechanisms of horizontal circulation and vertical overturning. For a zonal transoceanic section, a property  $P$  is expressed as:

$$P = P_0 + P'(x, \gamma_n) = P_0 + \langle P \rangle (\gamma_n) + P''(x, \gamma_n)$$

where  $P_0 = \frac{\iint P(x, \gamma_n) dx d\gamma_n}{\iint dx d\gamma_n}$  is the area-weighted section average,  $P'(x, \gamma_n) = P(x, \gamma_n) - P_0$  is the property anomaly,  $\langle P \rangle (\gamma_n) = \frac{\int (P(x, \gamma_n) - P_0) dx}{\int dx}$  are the area-weighted zonally averaged deviations from the property average  $P_0$ , and  $P''(x, \gamma_n) = P - P_0 - \langle P \rangle (\gamma_n)$  are the deviations from the zonal and section averages (the residual values). The last two terms are included in the anomaly term, so that  $P'(x, \gamma_n) = \langle P \rangle (\gamma_n) + P''(x, \gamma_n)$ . The  $x$  and  $\gamma_n$  coordinates refer to the zonal and vertical extent of the section, respectively.

The transport of this property can be broken up into its corresponding components, related to those of the property:

1. The barotropic component, which represents the net transport across the section at the section averaged property concentration. This term has been called “throughflow” (McDonagh et al., 2015) and “leakage” (Wijffels, 2001):

$$P_{\text{throughflow}} = T_{\text{BS}} (P_{\text{BS}} - P_0),$$

where  $T_{\text{BS}} = -0.8 \text{ Sv}$  is the interbasin mass transport, and  $P_{\text{BS}}$  is the average Bering Strait property value.

2. The baroclinic transport, due to zonally averaged vertical-meridional circulation, and associated with the overturning circulation across the section. This term is called “overturning”:

$$P_{\text{overturning}} = \iint \rho \langle P \rangle \langle \text{vel} \rangle dx d\gamma_n$$

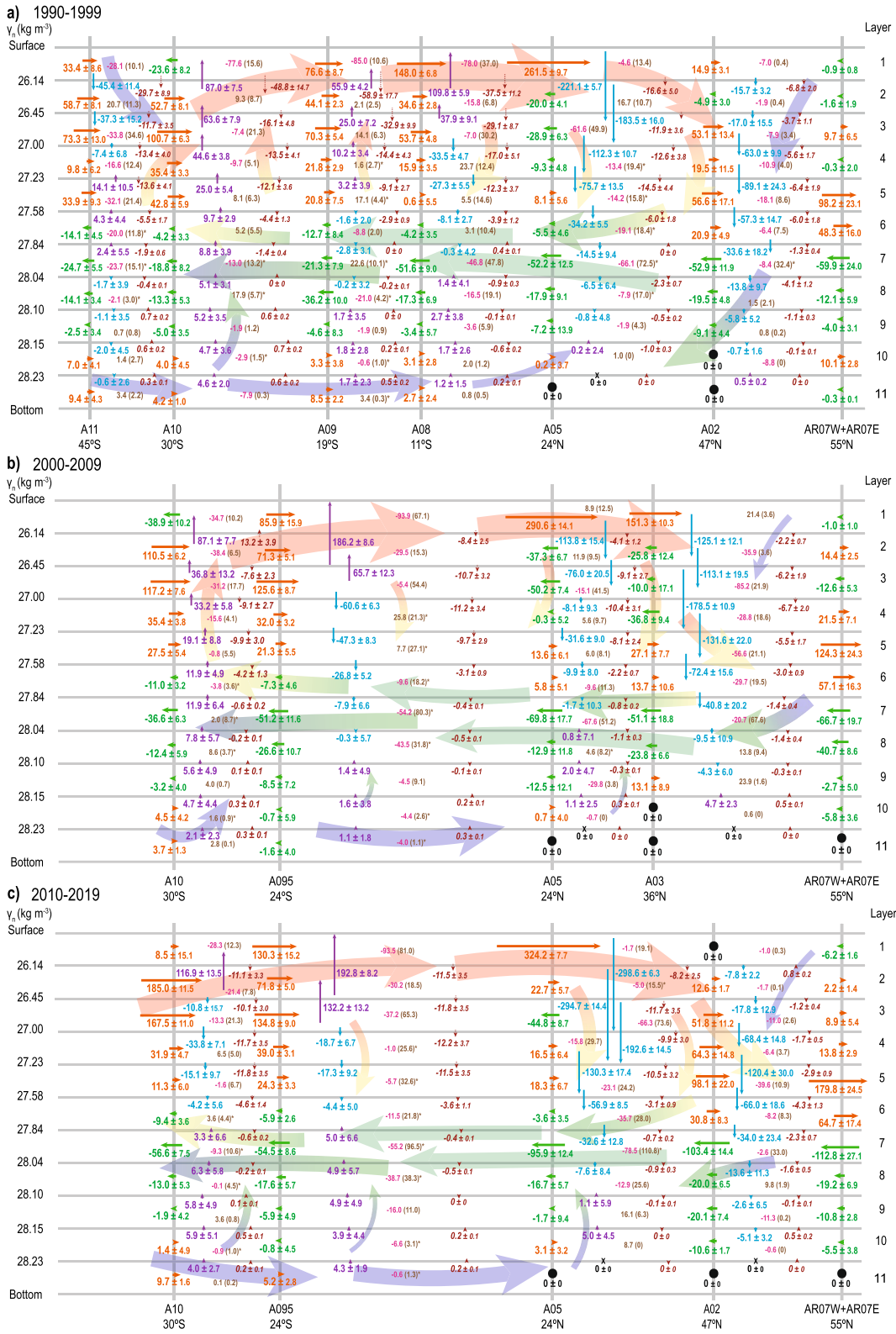


Figure 2.

3. The horizontal transport, due to the large-scale gyre circulation and smaller-scale eddies, which reflects correlations between residual velocity and property fields. This term is referred to as “horizontal” or “gyre”:

$$P_{\text{horizontal}} = \iint \rho P'' \text{vel}'' dx d\gamma_n$$

Applying these expressions to  $C_{\text{anth}}$  transport, we found negligible values for the throughflow component (with an average southward transport of  $-0.002 \text{ PgC yr}^{-1}$ ) and therefore are not shown.

### 3. Results

#### 3.1. Meridional Overturning Circulation and $C_{\text{anth}}$ Components

The meridional circulation in the Atlantic follows two-counter rotating cells (Caínzos et al., 2022; Kersalé et al., 2020). The balance in these cells involves northward transports of upper and abyssal layers, compensated by southward-flowing North Atlantic Deep Water (NADW) in between. The meridional advection of  $C_{\text{anth}}$  transport follows a similar pattern (Figure 2). For the South Atlantic, there is a layer of northward transport with stronger values between the surface and  $27.00 \text{ kg m}^{-3}$  for all decades. There is a subsurface maximum transport of  $C_{\text{anth}}$  associated with modal or central waters flowing between  $26.45$  and  $27.00 \text{ kg m}^{-3}$  at  $30^\circ\text{S}$  and  $24^\circ\text{S}$  and distributed more evenly on its way equatorward (sections 19 and  $11^\circ\text{S}$  in 1990–1999). At  $24^\circ\text{N}$  there is a shallowing of the northward transport of  $C_{\text{anth}}$ , delimited to the first layer, and, more specifically, to the Florida Straits Current, that dominates the upper flux (Figure 2). This transport is opposed by a southward normalized transport for the upper mid-ocean, computed as the upper transport discounting the Florida Straits transport (UMO;  $-0.333 \pm 0.015$ ,  $-0.376 \pm 0.019$ , and  $-0.309 \pm 0.016 \text{ PgC yr}^{-1}$ , for 1990–1999, 2000–2009, and 2010–2019, respectively) between  $26.14$  and  $27.84 \text{ kg m}^{-3}$  (Figure 3). In the SPNA (at  $47^\circ\text{N}$  and  $55^\circ\text{N}$ ) the core of the NAC (North Atlantic Current) gets  $\sim 4\%$  denser on its way northward (Caínzos et al., 2022), with stronger  $C_{\text{anth}}$  transports between  $27.23$  and  $27.58 \text{ kg m}^{-3}$ . Deep water formation in the Nordic and Labrador Seas offers a return southward flow of  $C_{\text{anth}}$  transport with stronger values in the upper limb of the NADW, between  $27.84$  and  $28.04 \text{ kg m}^{-3}$ , a pattern that is maintained as it is advected southward, despite decreasing its strength.

The division into components of  $C_{\text{anth}}$  transport reflects the importance of each component in the total transport (Figure 3). The total transport is a balance between the barotropic or throughflow component (which remains mainly unchanged), and the baroclinic (overturning) and horizontal (or gyre) transports. The overturning component of the  $C_{\text{anth}}$  transport provides the vertical circulation across the section, representing changes in the meridional structure of the water column. This is the principal component of the total  $C_{\text{anth}}$  transport, determining the importance of the vertical circulation in the distribution of  $C_{\text{anth}}$ , with a northward transport for the whole basin, carrying waters with high concentration of  $C_{\text{anth}}$  by the upper branch of the AMOC, contrasting with the southward transport of waters by the lower branch of the AMOC with lower concentration of  $C_{\text{anth}}$ . This overturning increases equatorward, following the increase in AMOC and heat transport, corroborated by the correlation between  $C_{\text{anth}}$  overturning transport and heat overturning transport (Figure 4). The slopes show a relationship between  $C_{\text{anth}}$  and heat increasing in time ( $0.183$ ,  $0.273$  and  $0.331 \text{ gC W}^{-1} \text{ yr}^{-1}$  for each decade, respectively), which persist, albeit slightly reduced, even when normalized ( $0.229$ ,  $0.268$ , and  $0.287 \text{ gC W}^{-1} \text{ yr}^{-1}$ , respectively, with an average value of  $0.261 \pm 0.030 \text{ gC W}^{-1} \text{ yr}^{-1}$ ). As a result, for the same overturning heat transport, the amount of  $C_{\text{anth}}$  transport carried by the overturning has been increasing (by  $\sim 0.0074 \pm 0.0030 \text{ gC W}^{-1} \text{ yr}^{-1}$ ). In the overturning  $C_{\text{anth}}$  transport, there is a leap between the first two decades and the last one in the subtropical gyres, with values between 1990–1999 and 2010–2019 around 50% larger at  $30^\circ\text{S}$  and  $24^\circ\text{N}$  and  $\sim 15\%$

**Figure 2.** Vertical and meridional schematic of  $C_{\text{anth}}$  circulation in the Atlantic Ocean for each decade. The gray horizontal lines mark the neutral density interphases, and the gray vertical lines are the position of each zonal section at their nominal latitude for the (a) 1990–1999 decade, (b) 2000–2009 decade, and (c) 2010–2019 decade. The meridional  $C_{\text{anth}}$  transport ( $\text{PgC yr}^{-1}$ ) is represented with horizontal arrows, in orange for northward (positive) transport and green for southward (negative) transport. Black dots in the North Atlantic appear in layers with null transport. The vertical transport due to the advection of mass between two sections in the interphase between two layers is represented with vertical arrows, in violet for upward (positive) transport and blue for downward (negative) transport. Black crosses represent layers with no vertical transport. The uncertainties associated with  $C_{\text{anth}}$  transport are part of the results of the inverse model using the Gauss-Markov estimator. The vertical transport due to the diffusion of  $C_{\text{anth}}$  appears with dashed brown arrows and values, with positive for upward diffusive transport and negative for downward diffusion. For each cell, the values within parenthesis indicate the storage of  $C_{\text{anth}}$  as computed from Gruber et al. (2019). Asterisks mark the cells where the modification from Sabine, Felly, Gruber, et al. (2004) had to be included. The numbers outside of the parenthesis indicate the imbalance within each cell, in ocre for a (positive) gain of  $C_{\text{anth}}$  and pink for a (negative) loss of  $C_{\text{anth}}$ . Background arrows manifest the presence of two counter-rotating overturning cells across the basin.



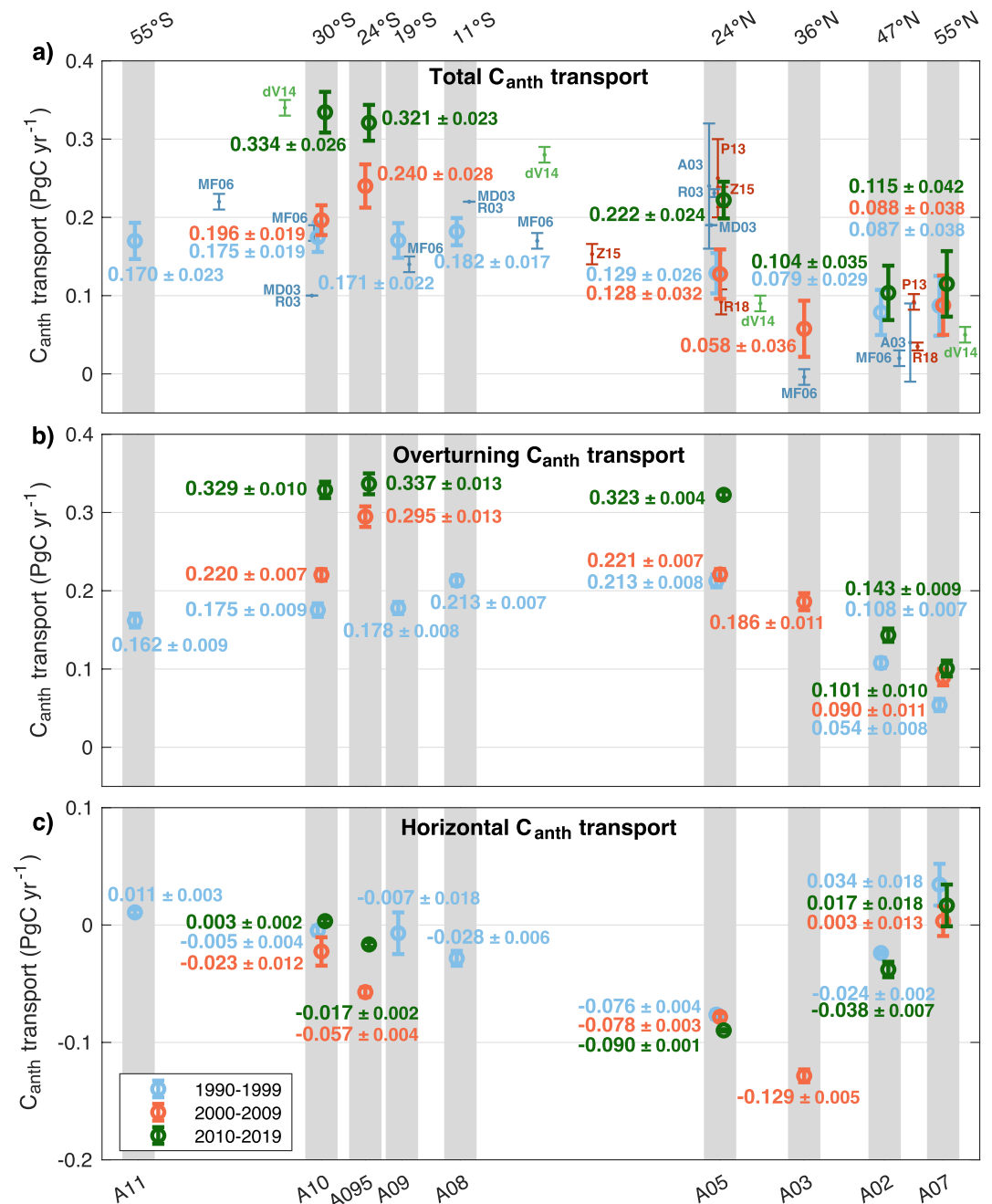


**Figure 3.**  $C_{anth}$  transport attending to its division into components (in  $PgC\ yr^{-1}$ ). The gray bars mark the nominal latitude of each zonal section, and the colors represent each decade, blue for 1990–1999, orange for 2000–2009, and green for 2010–2019. The total transport (a) is mainly divided into its principal components: overturning (b) and horizontal or gyre (c). The total  $C_{anth}$  transport is similar to the overturning transport, as the horizontal component is quite small. The uncertainties associated with the  $C_{anth}$  transports are part of the results of the inverse model solved using the Gauss-Markov estimator. Literature values (Figure S5 and Table S11 in Supporting Information S1) are added for comparison to the total  $C_{anth}$  transport: A03 (Álvarez et al., 2003), dV14 (DeVries, 2014), MD03 (Macdonald et al., 2003), MF06 (Mikaloff Fletcher et al., 2006), P13 (Pérez et al., 2013), R18 (Racapé et al., 2018), R03 (Rosón, 2003), Z15 (Zunino et al., 2015).

larger between 2000–2009 and 2010–2019 at 24°S. Moreover, in the SPNA, there is a slight increase between 1990–1999 and 2010–2019 at 47 and 55°N.

The horizontal or gyre component gives information of the role of large-scale gyre circulation and eddies, including the differences in the circulation along the section, both vertically and horizontally. The values are rather small

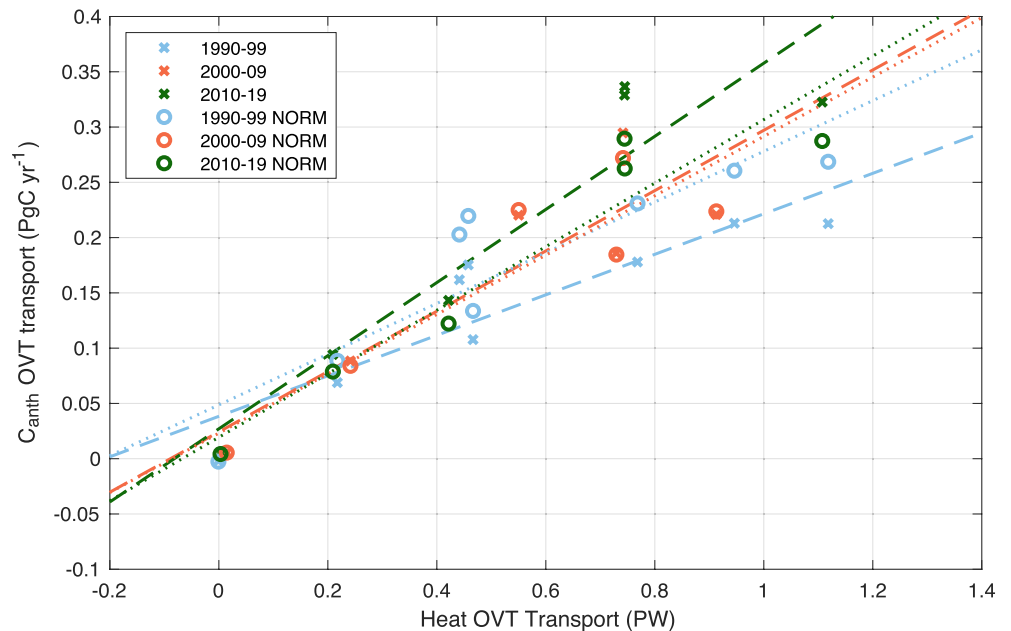


**Figure 4.** Relationship between the overturning components of heat (PW) and  $C_{\text{anth}}$  transport ( $\text{PgC yr}^{-1}$ ). Scatter plots of heat overturning transport against  $C_{\text{anth}}$  overturning transport, represented with their standard values (crosses) and normalized to 2005 (open circles), for each section and for the three decades. Each color represents a decade: blue for 1990–1999, orange for 2000–2009, and green for 2010–2019. Linear regressions were fitted for each decade in the colored dashed lines for the normal transport, and dotted lines represent the regressions using normalized  $C_{\text{anth}}$  transport.

and with low variability for the whole basin, with averages for all sections of  $-0.014 \pm 0.027$ ,  $-0.057 \pm 0.019$ , and  $-0.025 \pm 0.019 \text{ PgC yr}^{-1}$  for each decade, respectively. Of the total 17 sections, only the three cruises at  $24^\circ\text{N}$  and the one at  $36^\circ\text{N}$  show large negative values due to an eastern current transporting  $C_{\text{anth}}$ -enriched waters southwards. The contribution of the overturning and horizontal components to the transport of  $C_{\text{anth}}$  varies with latitude. An increase in the overturning would imply a stronger vertical pattern in the water column, so that the residuals along the section are lower and therefore, so is the horizontal component of the circulation. In the South Atlantic, the horizontal transport of  $C_{\text{anth}}$  represents less than 20% of the absolute overturning transport, whereas for  $24^\circ\text{N}$ , the percentages vary with the decades (36%, 35%, and 28%, respectively for each decade), with a related large percentage for  $36^\circ\text{N}$  in 2003 (69%) and a relatively high impact of the SPNA at  $47^\circ\text{N}$  (22% and 27%). There is an increase in the horizontal component for the 2000–2009 decade over the Atlantic, strengthening the southward horizontal transport at  $30^\circ\text{S}$ ,  $24^\circ\text{S}$ ,  $24^\circ\text{N}$ , and  $36^\circ\text{N}$ . This increase is counteracted by a reduction in the horizontal northward transport at  $55^\circ\text{N}$ , contributing only 4% of the overturning component. This could be associated with the reduction in the AMOC for this period at  $24^\circ\text{N}$ , due to an increase in the opposing upper mid-ocean (UMO) transport (Worthington et al., 2021).

### 3.2. Vertical Distribution of $C_{\text{anth}}$ Transports

Our results allow the study of the Atlantic Ocean from  $45^\circ\text{S}$  to  $55^\circ\text{N}$  in 1990–1999 and from  $30^\circ\text{S}$  to  $55^\circ\text{N}$  in 2000–2009 and 2010–2019. Attending to our repeating sections we can form two superboxes— $30^\circ\text{S}$  to  $24^\circ\text{N}$  and  $24^\circ\text{N}$  to  $55^\circ\text{N}$  that can be compared for the three decades. The former includes the South Atlantic subtropical gyre, the Intertropical convergence Zone and the North Atlantic equatorial region. The latter includes the North Atlantic subtropical gyre and the SPNA. We have computed the meridional transport, storage and air-sea influx of  $C_{\text{anth}}$  in  $\text{PgC yr}^{-1}$  within each box for the total depth, as well as for the division into upper and lower layers (Figure 5). With this division, the upper AMOC encompasses the northward upper layers of thermocline and intermediate waters, and the lower layer includes the combination of the deep southward layer and the northward abyssal layer of AMOC.

At  $30^\circ\text{S}$ , the net transport for the section increases in time ( $0.175 \pm 0.019$ ,  $0.197 \pm 0.019$ , and  $0.334 \pm 0.026 \text{ PgC yr}^{-1}$ , for each decade, respectively; Figure 5), with a large leap for the last decade, resulting

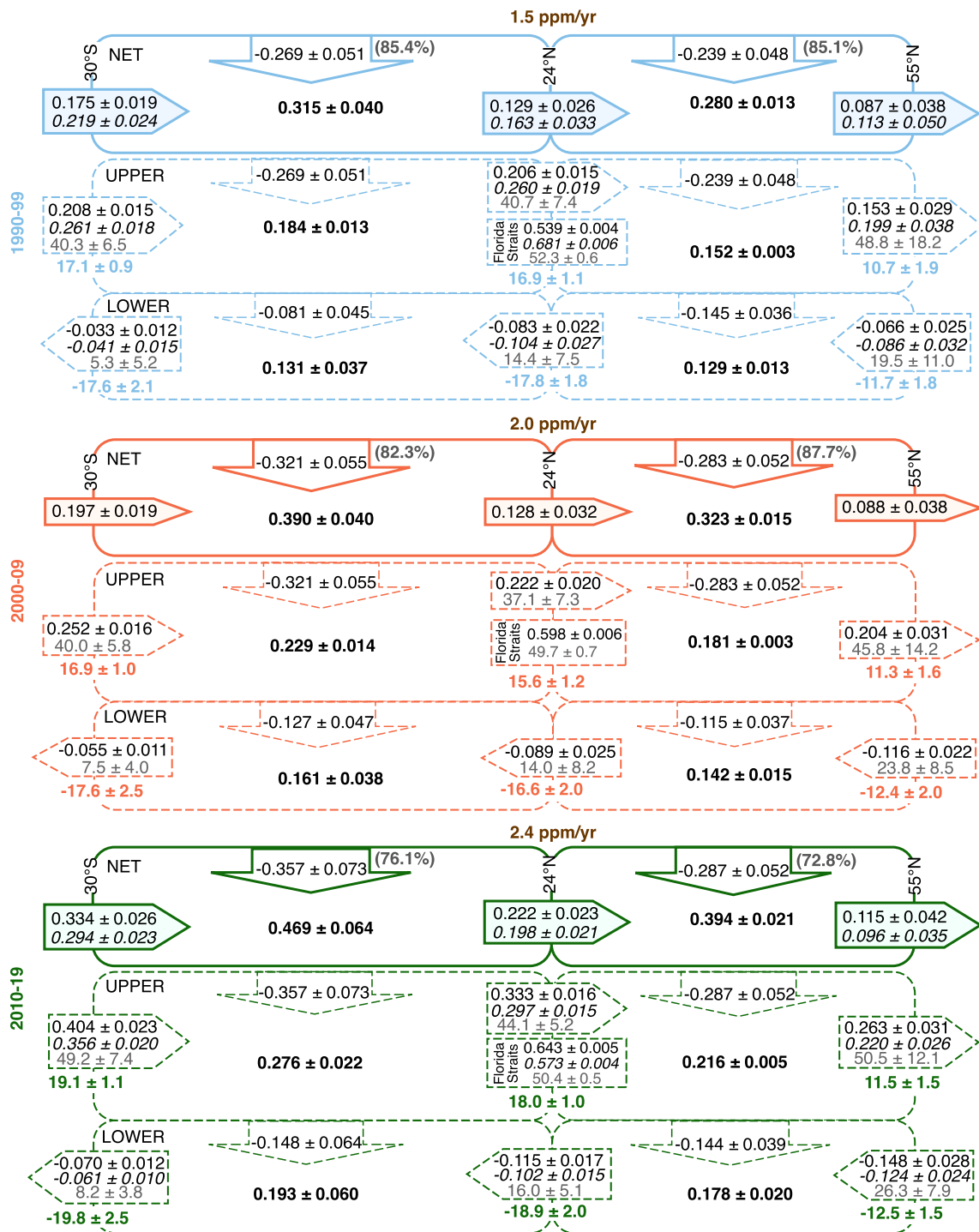


**Figure 5.**  $C_{\text{anth}}$  budget in the Atlantic Ocean for two superboxes— $30^{\circ}\text{S}$  to  $24^{\circ}\text{N}$  and  $24^{\circ}\text{N}$  to  $55^{\circ}\text{N}$  for each decade, represented by different colors (blue for 1990–1999, orange for 2000–2009, and green for 2010–2019). For each decade, the upper boxes, with continuous lines, represent the net values for the whole water column, whereas the dashed boxes represent the division into the upper and lower branches of the Atlantic Meridional Overturning Circulation. Each box is delimited on either side by the meridional transport across the section, specifying the transport of different properties:  $C_{\text{anth}}$  transport ( $\text{PgC yr}^{-1}$ ) appears with black regular values, normalized  $C_{\text{anth}}$  transport ( $\text{PgC yr}^{-1}$ ) are the black italic values, and the mass transport ( $\text{Sv}$ ) are the colored bold values outside the arrow. Moreover, the normalized transport-weighted  $C_{\text{anth}}$  ( $\mu\text{mol kg}^{-1}$ ) concentration is also included as the gray values. At  $24^{\circ}\text{N}$ , there is an extra meridional transport box for the values associated to the Florida Straits. Within each cell there is a bold black value that determines the  $C_{\text{anth}}$  storage ( $\text{PgC yr}^{-1}$ ) as obtained from Gruber et al. (2019) and Sabine, Feely, Gruber, et al. (2004) and normalized to the middle of each decade (1995, 2005, and 2015). The vertical arrows at the top of each box are the vertical influx of  $C_{\text{anth}}$  ( $\text{PgC yr}^{-1}$ ), namely the atmospheric input for the upper boxes. The bold gray values in parenthesis represent the percentage of uptake to the net storage of each box. The bold brown values at the top of each decade specifies the rate of increase of atmospheric  $\text{CO}_2$  for each decade.

from the ~55% strengthening of the second and third layers of surface and modal waters (Figure 2). This increase in the strength of the circulation in time is also evident in the northward transport of upper layers ( $0.208 \pm 0.015$ ,  $0.252 \pm 0.016$ , and  $0.404 \pm 0.023$  PgC yr<sup>-1</sup>, respectively per decade) and, to a lesser extent, in the southward lower layers ( $-0.033 \pm 0.012$ ,  $-0.055 \pm 0.011$ , and  $-0.070 \pm 0.012$  PgC yr<sup>-1</sup>, for each decade). To remove the effects of the expected marine C<sub>anth</sub> increase assuming TSS (Tanhua et al., 2006), we have normalized C<sub>anth</sub> transports to the same year (2005). The upper layers show similar values for the first decades (~0.26 PgC yr<sup>-1</sup>), with an increase of 40% over the expected for the last decade. However, the lower branch of the AMOC slightly increases with very similar transports. Values for the 2005-normalized transport-weighted (TW) C<sub>anth</sub> for upper layers ( $40.3 \pm 6.5$ ,  $40.0 \pm 5.8$ , and  $49.2 \pm 7.4$  μmol kg<sup>-1</sup>, respectively per decade; gray values in Figure 5) are comparable. The lower branch of the AMOC maintains a marginal increasing tendency with time ( $5.3 \pm 5.2$ ,  $7.5 \pm 4.0$ , and  $8.2 \pm 3.8$  μmol kg<sup>-1</sup>, respectively) with values slightly higher than those expected following TSS, although within uncertainties and therefore maybe not significant. Therefore, the change in the net transport is dominated by the transport of the upper layer, that in 2010–2019 has increased its mass transport and its TW-C<sub>anth</sub> concentration, resulting in the large value of C<sub>anth</sub> transport.

The net flux for the whole water column of the meridional C<sub>anth</sub> transport consistently decreases northward, with a reduction of 26%, 54%, and 34% between 30°S and 24°N for the decades 1990–1999, 2000–2009, and 2010–2019, respectively. The lower branch of the AMOC at 24°N show relatively consistent values with time ( $-0.083 \pm 0.022$ ,  $-0.089 \pm 0.025$ , and  $-0.115 \pm 0.017$  PgC yr<sup>-1</sup>, respectively). Considering TSS, the 2005-normalized TW C<sub>anth</sub> for the lower branch are  $14.4 \pm 7.5$ ,  $14.0 \pm 8.2$ , and  $16.0 \pm 5.1$  μmol kg<sup>-1</sup> per decade, which are relatively stable and almost double the concentrations at 30°S. The pattern of circulation at 24°N between decades shows similar values in transport and TW C<sub>anth</sub> concentration between 1990–1999 and 2000–2009, with a later recovery between 2000–2009 and 2010–2019 ( $0.129 \pm 0.026$ ,  $0.128 \pm 0.032$ , and  $0.222 \pm 0.023$  PgC yr<sup>-1</sup>, respectively), resulting from the low increase in the upper branch of the AMOC in 2000–2009 ( $0.206 \pm 0.015$ ,  $0.222 \pm 0.020$ , and  $0.333 \pm 0.016$  PgC yr<sup>-1</sup>, respectively). The higher northward upper transport for the first decade is associated with a larger value of the normalized Florida Strait (FS) transport ( $0.681 \pm 0.006$ ,  $0.598 \pm 0.006$ , and  $0.573 \pm 0.004$  PgC yr<sup>-1</sup>, respectively). This upper flux at 24°N is dominated by the FS transport in the first layer (Figure 2), with southward normalized transport for the UMO ( $-0.420 \pm 0.020$ ,  $-0.376 \pm 0.020$ , and  $-0.272 \pm 0.015$  PgC yr<sup>-1</sup>, for 1990–1999, 2000–2009, and 2010–2019, respectively). This transport of C<sub>anth</sub> by UMO partially reduces the net C<sub>anth</sub> transport of the total upper layer, although the decreasing trend is not apparent in the upper layer transport, dominated by the transport across the FS.

The northernmost section available, at 55°N, is composed by two subsections: the western one determining the transport across the Labrador Sea and the eastern one reflecting the northward transport by the NAC and the southward transport of the newly subducted deep waters in the sills and Nordic Seas. There is a weakening in the net C<sub>anth</sub> transport northward, with a reduction over the whole basin between 30°S and 55°N of 50%, 55%, and 66% for the decades 1990–1999, 2000–2009, and 2010–2019, respectively. This pattern resembles that from the lower branch of the AMOC, with a steady South-North increasing gradient in C<sub>anth</sub> transport ( $-0.066 \pm 0.025$ ,  $-0.116 \pm 0.022$ , and  $-0.148 \pm 0.028$  PgC yr<sup>-1</sup> for each decade at 55°N, respectively) maintained through the decades, with around 50% more at 55°N than at 30°S. The normalized TW C<sub>anth</sub> show C<sub>anth</sub>-enriched waters at 55°N ( $19.5 \pm 11.0$ ,  $23.8 \pm 8.5$ , and  $26.3 \pm 7.9$  μmol kg<sup>-1</sup>, per decade) that arrive at the south Atlantic subtropical gyre with ~30% of the original concentration. In the 2000–2009 and 2010–2019 decades, this southward decrease is also evident on the standard and normalized meridional transport, with a rather low C<sub>anth</sub> transport for the 1990–1999 decade. The upper AMOC transports central and intermediate waters with similar TW C<sub>anth</sub> concentration for the whole period ( $48.8 \pm 18.2$ ,  $45.8 \pm 14.2$ , and  $50.5 \pm 12.1$  μmol kg<sup>-1</sup>, respectively). However, the normalized upper C<sub>anth</sub> transports experience a very slight increase in the last decade ( $0.199 \pm 0.038$ ,  $0.204 \pm 0.031$ , and  $0.220 \pm 0.026$  PgC yr<sup>-1</sup>, respectively).

The northward transport of the Antarctic Bottom Water (AABW) appears in the southernmost sections (namely, 45°S for the 1990–1999 decade and 30°S for the 2000–2009 and 2010–2019 decades). There is a consistent pattern of reduction of northward C<sub>anth</sub> transport as the water masses travel north (Figure S2 in Supporting Information S1) for the three decades, accompanied by a decrease in the TW C<sub>anth</sub> concentration from 45°S ( $22.5 \pm 16.2$  μmol kg<sup>-1</sup>) to 30°S ( $8.9 \pm 6.8$  μmol kg<sup>-1</sup>) in the first decade. Despite observing similar transports of C<sub>anth</sub> at 30°S ( $0.008 \pm 0.005$ ,  $0.008 \pm 0.004$ , and  $0.011 \pm 0.005$  PgC yr<sup>-1</sup>, respectively), their normalized TW C<sub>anth</sub> concentration increase in time ( $8.9 \pm 6.8$ ,  $10.3 \pm 8.5$ , and  $11.0 \pm 8.2$  μmol kg<sup>-1</sup>, respectively), although not significantly due to the large uncertainties. The divergence of transports between adjacent sections is the major

component of the vertical flux of  $C_{\text{anth}}$ , which is mainly exported upwards to deep layers. Therefore, there is an enrichment of  $C_{\text{anth}}$  by the abyssal branch of the AMOC to the deep layers with nearly depleted  $C_{\text{anth}}$ , generating a deep ventilation of  $C_{\text{anth}}$ . This signal can be found in the South Atlantic, with a significant transport up to  $11^{\circ}\text{S}$  (in 1990–1999) and non-significant values at  $24^{\circ}\text{N}$ .

Defining the Atlantic basin with boundaries at  $30^{\circ}\text{S}$  and  $55^{\circ}\text{N}$  for all decades, we can detect an overall divergence over the basin, with a total storage and uptake from the atmosphere (Figure 5 and Figure S3 in Supporting Information S1). This divergence in the transport at the boundaries of the Atlantic box results in an accumulation in the storage of  $C_{\text{anth}}$  over the whole basin, due to a change at  $30^{\circ}\text{S}$  significantly larger than the relatively low transports at  $55^{\circ}\text{N}$ . The storage rate supplied by this divergence is 14.7%, 15.3%, and 25.3% per decade, with the increase in the last decade due to a  $\sim 13\%$  stronger overturning at  $30^{\circ}\text{S}$ .

### 3.3. Vertical Fluxes of $C_{\text{anth}}$

In the North Atlantic the downward vertical mass transport between upper and deep layers ( $-6.1 \pm 2.5$ ,  $-4.2 \pm 2.7$ , and  $-6.4 \pm 2.4$  Sv for each decade, respectively; Figure S4 in Supporting Information S1) represents a large part (57%, 37%, and 56%) of the meridional transport across  $24^{\circ}\text{N}$ , manifesting the significance of the vertical overturning within the box between  $24^{\circ}\text{N}$  and  $55^{\circ}\text{N}$ , with the remaining of the overturning north of  $55^{\circ}\text{N}$ .

The study of the balance of mass within each cell allows the estimation of the vertical transport of  $C_{\text{anth}}$  due to the vertical advection of mass. Accordingly, in the North Atlantic box ( $24^{\circ}\text{N}$ – $55^{\circ}\text{N}$ ), the  $C_{\text{anth}}$  transports across the interphases between upper and deep layers show consistent relatively large values for a downward transport of  $C_{\text{anth}}$  to deep layers ( $-0.033 \pm 0.014$ ,  $-0.025 \pm 0.016$ , and  $-0.050 \pm 0.019$  PgC yr $^{-1}$  for each decade, respectively).

In the South Atlantic, the upwelling of the recently ventilated AABW from the Southern Ocean results in an upward advection of  $C_{\text{anth}}$  transport from abyssal to deep layers. However, the vertical transport in the South Atlantic is dominated by the diffusive transport of  $C_{\text{anth}}$ , that appears due to the change at the interphase between layers from the vertical gradient of  $C_{\text{anth}}$  concentration along the water column. The larger concentration difference between upper and deep layers result in a larger diffusion transport at this interphase ( $-0.086 \pm 0.026$ ,  $-0.092 \pm 0.028$ , and  $-0.119 \pm 0.036$  PgC yr $^{-1}$  for each decade for the South Atlantic box, and  $-0.072 \pm 0.021$ ,  $-0.087 \pm 0.026$ , and  $-0.094 \pm 0.028$  PgC yr $^{-1}$  for the North Atlantic Box), with values around 40%–47% of the storage of the upper layer. Normalizing to the year 2005, we can find similar values among decades, for both the South Atlantic ( $-0.109 \pm 0.033$ ,  $-0.094 \pm 0.028$ , and  $-0.105 \pm 0.032$  PgC yr $^{-1}$ ) and North Atlantic ( $-0.090$ ,  $-0.089$ , and  $-0.083$  PgC yr $^{-1}$ ), supporting that these results follow the TSS in both boxes.

In the deep layers, there is a similar contribution from the north entrance of the AMOC and from the vertical fluxes from upper to deep layers (Figure S4 in Supporting Information S1). In the South Atlantic, the values are rather stable for all decades between the southward transport at the north boundary of the box at  $24^{\circ}\text{N}$  and the vertical fluxes due to the combination of vertical advection and diffusion caused by a vertical gradient in concentration of  $C_{\text{anth}}$  ( $-0.077 \pm 0.021$  and  $-0.086 \pm 0.026$ ,  $-0.095 \pm 0.025$  and  $-0.092 \pm 0.028$ , and  $-0.114 \pm 0.017$  and  $-0.119 \pm 0.036$  PgC yr $^{-1}$  for the horizontal deep transport and the vertical flux, respectively, for each decade). In the North Atlantic, these values are similar between the meridional deep transport and the total vertical flux ( $-0.066 \pm 0.025$  and  $-0.105 \pm 0.025$ ,  $-0.116 \pm 0.022$  and  $-0.112 \pm 0.017$ , and  $-0.148 \pm 0.028$  and  $-0.144 \pm 0.034$  PgC yr $^{-1}$ , respectively, for each decade) except for the first decade, when a weaker entrance from deep layers of the AMOC is overshadowed by the vertical input from the upper layers. Moreover, in the South Atlantic the main component of the vertical flux is the diffusion, and in the North Atlantic it accounts for  $\sim 70\%$ – $50\%$  of the total vertical flux.

### 3.4. Storage and Air-Sea Flux of $C_{\text{anth}}$

The storages within each box obtained from the inventories of Gruber et al. (2019) and Sabine, Felly, Gruber, et al. (2004) are stable for the South Atlantic (24% and 20% increase between 1990–1999 and 2000–2009 and between 2000–2009 and 2010–2019, respectively), whereas they have increased for the North Atlantic (15% and 22%; Figure 5). The values for the upper branch of the AMOC remain stable, and we can find the deceleration

with respect to TSS between the first two decades and the relative acceleration between the last two in the lower branch of the AMOC in the North Atlantic (10% and 25%, respectively).

Generally, the storage for the whole column is greater in the box occupying the South Atlantic, due to its larger volume. However, the changes in concentrations are lower in the South Atlantic ( $164 \pm 8$ ,  $201 \pm 9$  and  $243 \pm 9 \mu\text{mol m}^{-3} \text{ yr}^{-1}$ , respectively per decade) than in the North Atlantic ( $317 \pm 6$ ,  $372 \pm 7$ , and  $450 \pm 6 \mu\text{mol m}^{-3} \text{ yr}^{-1}$ , respectively).

The storage of upper layers contributes to  $\sim 59\%$  of the net storage between  $30^\circ\text{S}$  and  $24^\circ\text{N}$  and  $55\%$ – $56\%$  between  $24^\circ\text{N}$  and  $55^\circ\text{N}$ , manifesting the importance of deep layers in the storage of  $C_{\text{anth}}$ , although involved in processes occurring on longer timescales. For the whole region studied, the ratio between net uptake and storage is high ( $>70\%$ ), indicating that the storage of  $C_{\text{anth}}$  happens mostly as a result of the gain of  $C_{\text{anth}}$  from the atmosphere (Figure 5). Part of the uptake arriving to upper layers propagates downward and contributes significantly to the storage by deep layers. The vertical advection in the North Atlantic driven by the AMOC also provides to the storage in deep waters. The values in the South Atlantic increase with time, responding to the increase in the atmospheric  $p\text{CO}_2$  which causes larger values of  $C_{\text{anth}}$  storage.

## 4. Discussion

### 4.1. South Atlantic Box

A net  $C_{\text{anth}}$  transport of  $0.10 \text{ PgC yr}^{-1}$  entering the South Atlantic across  $30^\circ\text{S}$  has been reported from hydrographic data for 1993 (Holfort et al., 1998; Macdonald et al., 2003, Figure 3 and Figure S5 in Supporting Information S1). Our results for the same cruise are substantially larger ( $0.175 \pm 0.019 \text{ PgC yr}^{-1}$ ), consistently increasing for the following decades. These values can be evaluated against model results that have yielded comparably similar ( $0.18 \pm 0.01$  for 1995; Mikaloff Fletcher et al., 2006) and larger estimates ( $0.34 \pm 0.01$  at  $35^\circ\text{S}$  for 2012; DeVries, 2014). These values reflect the northward transport of  $C_{\text{anth}}$  from the recently formed central and intermediate waters from the Southern Ocean, decreasing in strength on its way northward.

Our results for the South Atlantic  $C_{\text{anth}}$  storage are like other estimates for a similar latitudinal extension for the 1990–1999 decade ( $0.31 \pm 0.02 \text{ PgC yr}^{-1}$  from  $30^\circ\text{S}$  to  $18^\circ\text{N}$ , Mikaloff Fletcher et al., 2006;  $0.250 \text{ PgC yr}^{-1}$  from  $30^\circ\text{S}$  to  $25^\circ\text{N}$ , Macdonald et al., 2003;  $0.265 \pm 0.011 \text{ PgC yr}^{-1}$ , Rosón, 2003), and agree with the value from DeVries et al. (2014) for 2012 from  $30^\circ\text{S}$  to  $30^\circ\text{N}$  ( $0.460 \text{ PgC yr}^{-1}$ ).

Moreover, the weaker value at  $30^\circ\text{S}$  from Holfort et al. (1998) creates a negative divergence within the South Atlantic box, with stronger meridional transports at  $24^\circ\text{N}$ , turning into an intensified uptake from the atmosphere ( $-0.340 \text{ PgC yr}^{-1}$ , Macdonald et al., 2003;  $-0.394 \pm 0.107 \text{ PgC yr}^{-1}$ , Rosón, 2003). However, sections with a decreasing northward transport and positive divergence present a consistent weaker uptake from the atmosphere ( $-0.160 \pm 0.017 \text{ PgC yr}^{-1}$ , Mikaloff Fletcher et al., 2006;  $-0.220 \text{ PgC yr}^{-1}$ , DeVries, 2014). Therefore, the strength of the meridional transport across the southern boundary of the Atlantic Ocean is an important factor in determining the role of meridional advection in the budget of  $C_{\text{anth}}$  in the South Atlantic.

Evans et al. (2017), using hydrographic sections from 2008 to 2009, have found a net northward  $C_{\text{anth}}$  transport at  $24^\circ\text{S}$  of  $0.28 \pm 0.16 \text{ PgC yr}^{-1}$  that is similar to our results at the same latitude in 2000–2009 of a net northward transport of  $0.24 \pm 0.03 \text{ PgC yr}^{-1}$ . This northward transport coming from surface, intermediate and abyssal layers arrive to the South Atlantic from the surface Agulhas Leakage and the whole-column input from Drake Passage, increasing the  $C_{\text{anth}}$  concentration at upper and abyssal layers (Figure 5 and Figure S2 in Supporting Information S1).

Deep ventilation in the South Atlantic assimilates  $C_{\text{anth}}$ -enriched waters to abyssal depths. The northward flow of AABW transports a part of the  $C_{\text{anth}}$  air-sea uptake happening in the Southern Ocean, estimated as a 40% of the global uptake (Khatiwala et al., 2009). Complementing the decrease in mass transport on its way northward, the AABW also gets mixed with the low-TW  $C_{\text{anth}}$  NADW above and decreases its concentration. The Atlantic sector of the Southern Ocean presents moderately high concentrations of  $C_{\text{anth}}$  in deep waters ( $\sim 10 \mu\text{mol kg}^{-1}$ ), with similar concentrations reported below 4,000 m between  $30$  and  $50^\circ\text{S}$  (Ríos et al., 2010) in 1994, which coincide with the TW  $C_{\text{anth}}$  estimates at  $30^\circ\text{S}$  for all decades, with a slightly larger value at  $45^\circ\text{S}$  for the first decade (Figure S2 in Supporting Information S1). The rate of increase for AABW determined by Ríos et al. (2012) of  $0.15 \pm 0.05 \mu\text{mol kg}^{-1} \text{ yr}^{-1}$  agrees with the change in TW  $C_{\text{anth}}$  for the abyssal layer at  $30^\circ\text{S}$  between the first

two decades, with  $1.4 \pm 10.8 \mu\text{mol kg}^{-1}$  difference between both cruises, although our values present large uncertainties arising from mass transport-weighted averaging. We have also found a non-significant slowing in the trend between 2000–2009 and 2010–2019, with a net change in concentration of  $0.7 \pm 11.8 \mu\text{mol kg}^{-1}$ . Orsi et al. (2002) determined a 21-Sv flow out of the Southern Ocean by the upper and lower Circumpolar Deep Waters and the AABW. Knowing that our contribution to the abyssal Atlantic basin is only 11% of this estimation for the whole basin ( $2.4 \pm 1.2 \text{ Sv}$ ), the transport of  $C_{\text{anth}}$  by abyssal layers results in  $0.011 \text{ PgC yr}^{-1}$ , a value like our estimations at  $45^\circ$  and  $30^\circ\text{S}$ .

#### 4.2. North Atlantic Box

$C_{\text{anth}}$  transports at  $24^\circ\text{N}$  present similar strengths for the 1990–1999 and 2000–2009 periods, that then recuperate in the last decade. The value in the 2004 cruise at  $24^\circ\text{N}$  is lower than expected, coinciding with a period of strong UMO (Worthington et al., 2021) as estimated by empirical models using observational data. This strong southward UMO, in turn, reduces the strength of the AMOC for this period, with stable values for the Florida Strait, Ekman, and deep layer transports. Therefore, the low  $C_{\text{anth}}$  transport at  $24^\circ\text{N}$  can be a result of a strengthening in the opposing southward transport carried by the UMO, accompanied by a reduction in the weighted  $C_{\text{anth}}$  concentration, as shown by the relatively low, although not significantly, values of  $\text{TW } C_{\text{anth}}$  for this period.

Brown et al. (2021) have published a time series reconstruction of  $C_{\text{anth}}$  transports across  $24^\circ\text{N}$  using data from the RAPID/MOCHA/WBTS mooring array and hydrographic observations. In the upper limb of the AMOC, decreasing northward mass transports were compensated by increasing  $C_{\text{anth}}$  concentration, resulting in a compensated northward  $C_{\text{anth}}$  transport for the 8.5-year period. We have compared our included cruises for 2000–2009 and 2010–2019 decades to the time series, and we have found similar values at the time of the cruise for each of the decompositions of the transport. The overturning  $C_{\text{anth}}$  transport (Figure S1b in Supporting Information S1) dominates the mean and variability of the total  $C_{\text{anth}}$  transport, with consistent negative values for the horizontal component for all the time series. Similarly, the upper layer of the water column, above 1,100 m, holds this variability (Figure S1c in Supporting Information S1), with small values for deep and abyssal transports, the latter almost negligible. The increasing trend in our results is also present in the 8.5-year timeseries, that can be attributed to the increase in the Florida Straits  $C_{\text{anth}}$  transport, while there is a stabilization in the Ekman transport across the section, resulting in the decrease of transport of the UMO.

The North Atlantic has been closely monitored, especially at the center of the subtropical gyre at  $24^\circ\text{N}$  and at the OVIDE section in the SPNA (Figure 3a and Figure S5 in Supporting Information S1). We have found meridional transports at  $24^\circ\text{N}$  similar to the estimates by ocean inversions that combine  $C_{\text{anth}}$  observations with results from general circulation models ( $0.12 \pm 0.01 \text{ PgC yr}^{-1}$  at  $18^\circ\text{N}$  for 1995, Mikaloff Fletcher et al., 2006;  $0.09 \pm 0.01 \text{ PgC yr}^{-1}$  at  $30^\circ\text{N}$  for 2012, DeVries, 2014), and by results from global biogeochemical ocean general circulation models ( $0.092 \pm 0.016 \text{ PgC yr}^{-1}$  at  $25^\circ\text{N}$  for 2003–2011, Racapé et al., 2018). Solutions from hydrographic data for  $24^\circ\text{N}$  present stronger meridional transports ( $0.19 \text{ PgC yr}^{-1}$  for 1992–1998, Macdonald et al., 2003;  $0.23 \pm 0.01 \text{ PgC yr}^{-1}$  for 1990–1999, Rosón, 2003;  $0.24 \pm 0.08 \text{ PgC yr}^{-1}$  for 1995, Álvarez et al., 2003;  $0.23 \pm 0.01 \text{ PgC yr}^{-1}$  for 2001, Zunino et al., 2015;  $0.25 \pm 0.05 \text{ PgC yr}^{-1}$  for 2004, Pérez et al., 2013).

For our northernmost sections, at  $55^\circ\text{N}$ , we are closer to the estimations supporting strong lateral transports at these latitudes ( $0.09 \text{ PgC yr}^{-1}$  at  $76^\circ\text{N}$  for 1995, Mikaloff Fletcher et al., 2006;  $0.063 \pm 0.019 \text{ PgC yr}^{-1}$  at  $63\text{--}66^\circ\text{N}$  for 2004, Pérez et al., 2013), marking a strong overturning that carries  $C_{\text{anth}}$  into the Nordic Seas via the deep convection taking place in this region.

The estimated amount of  $C_{\text{anth}}$  stored in the North Atlantic is quite similar to other studies, but we can find differences in the value of  $C_{\text{anth}}$  acquired from the atmosphere (Table S11 in Supporting Information S1), with low values for results from ocean general circulation models (Racapé et al., 2018), ocean inversions (DeVries et al., 2017) and hydrographic estimations (Macdonald et al., 2003; Pérez et al., 2013; Rosón, 2003; Álvarez et al., 2003).

#### 4.3. $C_{\text{anth}}$ in the Atlantic Basin and Connection to the Arctic Ocean

Using the estimations from Pérez et al. (2013) of  $-0.008 \pm 0.003 \text{ PgC yr}^{-1}$  of  $C_{\text{anth}}$  transport referenced to 2004 for the Bering Strait we have constructed a box between  $55^\circ\text{N}$  and the Bering Strait. The storages for this box were

divided into the box between 55°N and the Greenland-Iceland-Scotland Sills (~63°N–66°N), and the combined results north of the Sills from Pérez et al. (2013). North of the Sills the values comprised  $0.018 \pm 0.04$  PgC yr<sup>-1</sup> in the Nordic Seas between 63–66 and 78°N (Jeansson et al., 2011) and  $0.043 \pm 0.04$  PgC yr<sup>-1</sup> in the Arctic Seas between 78°N and the Bering Strait (Tanhua et al., 2009). The storages for each decade within the box between 55°N and the Sills were computed following the same methodology applied to the rest of the Atlantic, using the storage rates of Gruber et al. (2019) and the inventories of Sabine, Felly, Gruber, et al. (2004), and then normalized to 2005 assuming TSS (Figure S3 in Supporting Information S1).

Contrary to the Atlantic basin, where there is an uptake of  $C_{\text{anth}}$  throughout the basin, north of the SPNA there is a small loss of  $C_{\text{anth}}$  to the atmosphere, as the upper water masses are carrying large amounts of  $C_{\text{anth}}$  that become saturated as they cool during their northward transport. These estimations agree with the values north of the sills in Pérez et al. (2013), in boxes where the meridional divergence of  $C_{\text{anth}}$  transport dominates over its storage. The selection of transport from the Bering Strait influences on the net divergence in the box and, therefore on the sign of the atmospheric uptake and whether gain or loss toward the atmosphere is happening.

These values are relatively small, comparable to the negligible uptake of  $C_{\text{anth}}$  from the atmosphere in the Nordic Seas from Jeansson et al. (2011). However, the overturning circulation occurring at these latitudes redistributes the  $C_{\text{anth}}$  in the region and returns the upper layers of  $C_{\text{anth}}$ -enriched waters to the deep ocean. In turn, they then go back to the North Atlantic as the part of the dense overflows, with a lower layer representing a 43%, 57%, and 56% of the transport in upper layers at 55°N for each decade, respectively (Figure 5).

#### 4.4. Vertical Transport of $C_{\text{anth}}$

The Atlantic Ocean is, proportionally, the basin accumulating more  $C_{\text{anth}}$  in the whole column ( $12.5$  gC m<sup>-2</sup> yr<sup>-1</sup> in the Atlantic and  $6.9$  gC m<sup>-2</sup> yr<sup>-1</sup> in the Pacific), and, especially, the basin accumulating more  $C_{\text{anth}}$  below 1,000 m, over four times the  $C_{\text{anth}}$  stored in the Pacific ( $6.5$  gC m<sup>-2</sup> yr<sup>-1</sup> in the Atlantic vs.  $1.5$  gC m<sup>-2</sup> yr<sup>-1</sup> in the Pacific; Gruber et al., 2019). The vertical transport of  $C_{\text{anth}}$  has been often overlooked or restricted to the upper layers of the water column. However, we have seen that vertical advection and diffusion take part in the redistribution of  $C_{\text{anth}}$  in the ocean interior. Exporting more  $C_{\text{anth}}$  from the surface to the bottom and at a higher rate favors a larger future uptake of  $C_{\text{anth}}$ .

Figure S4 in Supporting Information S1 shows both overturning and diffusive mixing playing an important role in the transfer of  $C_{\text{anth}}$  from the atmosphere to deep layers. These vertical processes contribute to a considerable percentage of the net uptake of  $C_{\text{anth}}$  from the atmosphere (51%, 53%, and 64% per decade, respectively), redistributing the newly-gained  $C_{\text{anth}}$  to deep layers. From the net uptake in the Atlantic Ocean ( $-0.508 \pm 0.060$ ,  $-0.604 \pm 0.061$ , and  $-0.644 \pm 0.084$  PgC yr<sup>-1</sup>), the overturning north of 55°N supplies the  $C_{\text{anth}}$  sequestered by the overflow waters ( $-0.066 \pm 0.025$ ,  $-0.116 \pm 0.022$ , and  $-0.148 \pm 0.028$  PgC yr<sup>-1</sup> for each decade, respectively). In the north Atlantic box, there is also downward flux of mass associated with the overturning, advecting  $C_{\text{anth}}$  with it to deep layers ( $-0.033 \pm 0.014$ ,  $-0.025 \pm 0.016$ , and  $-0.050 \pm 0.019$  PgC yr<sup>-1</sup>). Over the whole basin (30°S to 55°N), mixing diffuses  $C_{\text{anth}}$  from upper to deep layers ( $-0.158 \pm 0.033$ ,  $-0.179 \pm 0.029$ , and  $-0.213 \pm 0.046$  PgC yr<sup>-1</sup>).

Both advection and diffusion, involved in vertical transfer of properties, contribute almost equally to the interior storage of  $C_{\text{anth}}$ . These processes have not been described nor evaluated and are new parameters to include in the models. This could be relevant in the future to the simulations using different IPCC scenarios. Holzer et al. (2021) have highlighted the importance of diffusion transports in the control of Pacific carbon and nutrient storage.

DeVries et al. (2017) have previously manifested the importance of the changes in the strength of the overturning in the uptake of CO<sub>2</sub> by the ocean. They modeled the stronger and weaker overturning in the upper ocean for the 1990s and 2000s, respectively, and found that an intense AMOC results in and increased outgassing of natural CO<sub>2</sub>, while the uptake of  $C_{\text{anth}}$  by the ocean also grew. However, with a weaker overturning in the 2000s, both gas exchanges decline and there appear a reduced outgassing of natural CO<sub>2</sub> and reduced uptake of  $C_{\text{anth}}$ . The vertical transport of mass to deep layers (>1,000 m) found by DeVries et al. (2017) shows strong export to deep layers in the Nordic Seas, north of 55°N, with a small contribution from the SPNA of  $2 \pm 1$  Sv for the 1980s and 1990s and stronger for the 2000s ( $7 \pm 1$  Sv). The latter estimation is more similar to our vertical advection of mass between 24 and 55°N (Figure S4 in Supporting Information S1;  $-6.1 \pm 2.5$ ,  $-4.2 \pm 2.7$ , and  $-6.4 \pm 2.4$  Sv for each decade, respectively). Racapé et al. (2018) also evaluated the vertical transfer of  $C_{\text{anth}}$  from surface to deep waters



and found that it occurred mainly north of the OVIDE section (40°N–60°N), with  $-0.097 \pm 0.028$  PgC yr<sup>-1</sup> exported to deep layers between 1959 and 1994 and  $-0.175 \pm 0.021$  PgC yr<sup>-1</sup> between 1996 and 2011.

## 5. Conclusions

This study has evaluated the meridional and vertical transports of  $C_{\text{anth}}$  in the Atlantic Ocean for the whole water column, assessing the importance of the deep and bottom layers in the redistribution of  $C_{\text{anth}}$ . We have obtained our results from three inverse models for the last three decades combining continuity equations of mass and biogeochemical tracers for boxes bounded by contiguous across-ocean zonal sections.

Our results for the South Atlantic reflect the northward transport of  $C_{\text{anth}}$  from the water masses recently formed in the Southern Ocean, with increasing values with time. At 24°N, we have detected the lower-than-expected values in the overturning for the 2004 cruise, possibly due to a strengthening of the UMO at the time, and thus increasing the southward horizontal component of the  $C_{\text{anth}}$  transport. In general, changes in the net transport of  $C_{\text{anth}}$  appear due to differences in the upper layer, with values for the lower branch of the AMOC more consistent with time.

We have included not only the meridional transports, but also the vertical transfers between upper and deep and deep and abyssal layers, evaluating the contribution of these processes in the net uptake of  $C_{\text{anth}}$ . The overturning in the North Atlantic, and especially in the SPNA and Nordic Seas, plays an important role in the redistribution of the newly gained  $C_{\text{anth}}$  from the atmosphere, with relatively large fluxes exporting  $C_{\text{anth}}$  to deep layers. In the South Atlantic, the abyssal layers play a role in the introduction of  $C_{\text{anth}}$  from the AABW into the water column, and as a result provide an upward flux of  $C_{\text{anth}}$  from abyssal to deep layers. Mixing by diffusion processes occurs over the whole Atlantic, mainly in the interphase between upper and deep layers, where a stronger gradient is present, and is the main process exporting  $C_{\text{anth}}$  from upper to deep layers in the South Atlantic.

## Data Availability Statement

Hydrographic data were collected from the CCHDO website (<https://cchdo.ucsd.edu>) in the frame of International WOCE and GO-SHIP projects and from the BODC databases for each cruise: A11 1992 ([https://cchdo.ucsd.edu/cruise/74DI199\\_1](https://cchdo.ucsd.edu/cruise/74DI199_1)), A10 1992 ([https://cchdo.ucsd.edu/cruise/06MT22\\_5](https://cchdo.ucsd.edu/cruise/06MT22_5)), A09 1991 ([https://cchdo.ucsd.edu/cruise/06MT15\\_3](https://cchdo.ucsd.edu/cruise/06MT15_3)), A08 1994 ([https://cchdo.ucsd.edu/cruise/06MT28\\_1](https://cchdo.ucsd.edu/cruise/06MT28_1)), A05 1992 ([https://cchdo.ucsd.edu/cruise/29HE06\\_1](https://cchdo.ucsd.edu/cruise/29HE06_1)), A02 1993 ([https://cchdo.ucsd.edu/cruise/06GA226\\_2](https://cchdo.ucsd.edu/cruise/06GA226_2)), AR07W 1990 ([https://cchdo.ucsd.edu/cruise/18DA90012\\_1](https://cchdo.ucsd.edu/cruise/18DA90012_1)), AR07E 1991 ([https://cchdo.ucsd.edu/cruise/74AB62\\_1](https://cchdo.ucsd.edu/cruise/74AB62_1)), A10 2003 (<https://cchdo.ucsd.edu/cruise/49NZ20031106>), A095 2009 (<https://cchdo.ucsd.edu/cruise/740H20090307>), A05 2004 (<https://cchdo.ucsd.edu/cruise/74DI20040404>), A03 2005 ([https://www.bodc.ac.uk/data/bodc\\_database/ctd/search/](https://www.bodc.ac.uk/data/bodc_database/ctd/search/), searching for 36 North under “Project”), AR07W 2005 (<https://cchdo.ucsd.edu/cruise/18HU20050526>), AR07E 2007 (<https://cchdo.ucsd.edu/cruise/64PE20070830>), A10 2011 (<https://cchdo.ucsd.edu/cruise/33RO20110926>), A095 2018 (<https://cchdo.ucsd.edu/cruise/740H20180228>), A05 2011 (<https://cchdo.ucsd.edu/cruise/29AH20110128>), A02 2013 (<https://cchdo.ucsd.edu/cruise/06M220130509>), AR07W 2014 (<https://cchdo.ucsd.edu/cruise/74JC20140606>) and AR07E 2014 (<https://cchdo.ucsd.edu/cruise/74JC20140606>). GLODAPv2.2021 is available via <https://www.glodap.info/index.php/merged-and-adjusted-data-product-v22021/>. The cruises obtained from GLODAPv2 have the following DOIs: A11 1992 ([https://doi.org/10.3334/cdiac/otg.woce\\_a11\\_74di19921222](https://doi.org/10.3334/cdiac/otg.woce_a11_74di19921222)), A10 1992 (<https://doi.org/10.3334/CDIAC/otg.ndp066>), A09 1991 (<https://doi.org/10.3334/CDIAC/otg.ndp051>), A08 1994 (<https://doi.org/10.3334/CDIAC/otg.ndp079>), A05 1992 (<https://doi.org/10.3334/CDIAC/otg.ndp074>), A10 2003 (<https://doi.org/10.25921/gjsx-gy37>), A095 2009 ([https://doi.org/10.3334/cdiac/otg.clivar\\_a9.5\\_2009](https://doi.org/10.3334/cdiac/otg.clivar_a9.5_2009)), A05 2004 ([https://doi.org/10.3334/cdiac/otg.carina\\_74di20040404](https://doi.org/10.3334/cdiac/otg.carina_74di20040404)), A03 2005 ([https://doi.org/10.3334/cdiac/otg.carina\\_74ab20050501](https://doi.org/10.3334/cdiac/otg.carina_74ab20050501)), AR07W 2005 ([https://doi.org/10.3334/cdiac/otg.woce\\_ar07w\\_2005](https://doi.org/10.3334/cdiac/otg.woce_ar07w_2005)), AR07E 2007 ([https://doi.org/10.3334/cdiac/otg.clivar\\_ar07e\\_2007](https://doi.org/10.3334/cdiac/otg.clivar_ar07e_2007)), A10 2011 ([https://doi.org/10.3334/cdiac/otg.clivar\\_a10\\_2011](https://doi.org/10.3334/cdiac/otg.clivar_a10_2011)), A095 2018 (<https://doi.org/10.25921/xy1r-rx06>), A05 2011 ([https://doi.org/10.3334/cdiac/otg.clivar\\_a05\\_29ah20110128](https://doi.org/10.3334/cdiac/otg.clivar_a05_29ah20110128)), and A02 2013 (<https://doi.org/10.25921/43nw-j564>). The carbon transport data that support the findings of Brown et al. (2021) are available from the BODC at <http://doi.org/10.5285/b6bb9f45-f562-68a4-e053-6c86abc0e48b>. The carbon concentrations for the 2014 AR07W and AR07E cruises of Tynan et al. (2016) are available from the BODC at <http://doi.org/10.5285/29ea7e19-d89c-3ab1-e053-6c86abc0284b>. The

anthropogenic CO<sub>2</sub> estimates reported in Gruber et al. (2019) can be obtained through NCEI's Ocean Carbon Data System: [https://www.ncei.noaa.gov/access/ocean-carbon-acidification-data-system/oceans/ndp\\_100/ndp100.html](https://www.ncei.noaa.gov/access/ocean-carbon-acidification-data-system/oceans/ndp_100/ndp100.html). The anthropogenic CO<sub>2</sub> estimates reported in Sabine, Feely, Gruber, et al. (2004) can be also accessed via NCEI's Ocean Carbon Data System: Sabine, Feely, Key et al. (2004), Accessed (2022-09-13). Matlab and R code for CANYON-B are available at <https://github.com/HCBScienceProducts/>. Matlab code for C<sub>anth</sub> estimation using PHI-CT0 method is available at [http://oceanoo.iim.csic.es/\\_media/cantphict0\\_toolbox\\_20190213.zip](http://oceanoo.iim.csic.es/_media/cantphict0_toolbox_20190213.zip). Datasets for the monthly average air-sea fluxes of O<sub>2</sub>, CO<sub>2</sub>, and N<sub>2</sub> from Earth System Models are available at <https://doi.org/10.5281/zenodo.4716840> (Morgan, 2021).

#### Acknowledgments

V.C. acknowledges the Agencia Canaria de Investigación, Innovación y Sociedad de la Información (ACIISI) grant program of "Apoyo al personal investigador en formación" TESIS2019010015. V.C. and A.H.-G. were supported by the SAGA project (RTI2018-100844-B-C31) funded by the Ministerio de Ciencia, Innovación y Universidades of the Spanish Government. F.F.P. and A.V. were supported by the BOCATS2 (PID2019-104279GB-C21) project funded by MCIN/AEI/10.13039/501100011033 and contributing to WATER:iOS CSIC PTI.

#### References

- Álvarez, M., Ríos, A. F., Pérez, F. F., Bryden, H. L., & Rosón, G. (2003). Transports and budgets of total inorganic carbon in the subpolar and temperate North Atlantic. *Global Biogeochemical Cycles*, *17*(1), 1–21. <https://doi.org/10.1029/2002GB001881>
- Anderson, L. A. (1995). On the hydrogen and oxygen content of marine phytoplankton. *Deep Sea Research, Part I: Oceanographic Research Papers*, *42*(9), 1675–1680. [https://doi.org/10.1016/0967-0637\(95\)00072-e](https://doi.org/10.1016/0967-0637(95)00072-e)
- Bittig, H. C., Steinhoff, T., Claustre, H., Fiedler, B., Williams, N. L., Sauzède, R., et al. (2018). An alternative to static climatologies: Robust estimation of open ocean CO<sub>2</sub> variables and nutrient concentrations from T, S, and O<sub>2</sub> data using Bayesian neural networks. *Frontiers in Marine Science*, *5*, 1–29. <https://doi.org/10.3389/fmars.2018.00328>
- Brown, P. J., McDonagh, E. L., Sanders, R., Watson, A. J., Wanninkhof, R., King, B. A., et al. (2021). Circulation-driven variability of Atlantic anthropogenic carbon transports and uptake. *Nature Geoscience*, *14*(8), 571–577. <https://doi.org/10.1038/s41561-021-00774-5>
- Bryden, H. L., & Imawaki, S. (2001). Chapter 6.1 Ocean heat transport. In G. Siedler, J. Church, & J. Gould (Eds.), *Ocean circulation & climate: Observing and modelling the Global Ocean* (pp. 455–474). Academic Press. [https://doi.org/10.1016/S0074-6142\(01\)80134-0](https://doi.org/10.1016/S0074-6142(01)80134-0)
- Caínzos, V., Hernández-Guerra, A., McCarthy, G. D., McDonagh, E. L., Cubas Armas, M., & Pérez-Hernández, M. D. (2022). Thirty years of GOSHIP and WOCE data: Atlantic overturning of mass, heat, and freshwater transport. *Geophysical Research Letters*, *49*(4). <https://doi.org/10.1029/2021GL096527>
- Cunningham, S. A., Kanzow, T., Rayner, D., Baringer, M. O., Johns, W. E., Marotzke, J., et al. (2007). Temporal variability of the Atlantic Meridional Overturning Circulation at 26.5°N. *Science*, *317*(5840), 935–938. <https://doi.org/10.1126/science.1141304>
- DeVries, T. (2014). The oceanic anthropogenic CO<sub>2</sub> sink: Storage, air-sea fluxes, and transports over the industrial era. *Global Biogeochemical Cycles*, *28*(7), 631–647. <https://doi.org/10.1002/2013GB004739>
- DeVries, T., Holzer, M., & Primeau, F. (2017). Recent increase in oceanic carbon uptake driven by weaker upper-ocean overturning. *Nature*, *542*(7640), 215–218. <https://doi.org/10.1038/nature21068>
- Doney, S. C., Busch, D. S., Cooley, S. R., & Kroeker, K. J. (2020). The impacts of ocean acidification on Marine ecosystems and reliant human communities. *Annual Review of Environment and Resources*, *45*(1), 83–112. <https://doi.org/10.1146/annurev-environ-012320-083019>
- Doney, S. C., Fabry, V. J., Feely, R. A., & Kleypas, J. A. (2009). Ocean acidification: The other CO<sub>2</sub> problem. *Annual Review of Marine Science*, *1*(1), 169–192. <https://doi.org/10.1146/annurev.marine.010908.163834>
- Evans, G. R., McDonagh, E. L., King, B. A., Bryden, H. L., Bakker, D. C. E., Brown, P. J., et al. (2017). South Atlantic interbasin exchanges of mass, heat, salt and anthropogenic carbon. *Progress in Oceanography*, *151*, 62–82. <https://doi.org/10.1016/j.pocean.2016.11.005>
- Fontela, M., Mercier, H., & Pérez, F. F. (2019). Long-term integrated biogeochemical budget driven by circulation in the eastern subpolar North Atlantic. *Progress in Oceanography*, *173*, 51–65. <https://doi.org/10.1016/j.pocean.2019.02.004>
- Friedlingstein, P., O'Sullivan, M., Jones, M. W., Andrew, R. M., Hauck, J., Olsen, A., et al. (2020). Global carbon budget 2020. *Earth System Science Data*, *12*(4), 3269–3340. <https://doi.org/10.5194/essd-12-3269-2020>
- Ganachaud, A. S., & Wunsch, C. (2000). Improved estimates of global ocean circulation, heat transport and mixing from hydrographic data. *Nature*, *408*(6811), 453–456. <https://doi.org/10.1038/35044048>
- Gattuso, J.-P., Magnan, A., Billé, R., Cheung, W. W. L., Howes, E. L., Joos, F., et al. (2015). Contrasting futures for ocean and society from different anthropogenic CO<sub>2</sub> emissions scenarios. *Science*, *349*(6243). <https://doi.org/10.1126/science.aac4722>
- Gruber, N., Clement, D., Carter, B. R., Feely, R. A., van Heuven, S., Hoppema, M., et al. (2019). The oceanic sink for anthropogenic CO<sub>2</sub> from 1994 to 2007. *Science*, *363*(6432), 1193–1199. <https://doi.org/10.1126/science.aau5153>
- Gruber, N., Sarmiento, J. L., & Stocker, T. F. (1996). An improved method for detecting anthropogenic CO<sub>2</sub> in the oceans. *Global Biogeochemical Cycles*, *10*(4), 809–837. <https://doi.org/10.1029/96GB01608>
- Guallart, E. F., Schuster, U., Fajar, N. M., Legge, O., Brown, P., Pelejero, C., et al. (2015). Trends in anthropogenic CO<sub>2</sub> in water masses of the subtropical North Atlantic ocean. *Progress in Oceanography*, *131*, 21–32. <https://doi.org/10.1016/j.pocean.2014.11.006>
- Guinotte, J. M., Orr, J., Cairns, S., Freiwald, A., Morgan, L., & George, R. (2006). Will human-induced changes in seawater chemistry alter the distribution of deep-sea scleractinian corals? *Frontiers in Ecology and the Environment*, *4*(3), 141–146. [https://doi.org/10.1890/1540-9295\(2006\)004\[0141:WHCISC\]2.0.CO;2](https://doi.org/10.1890/1540-9295(2006)004[0141:WHCISC]2.0.CO;2)
- Hernández-Guerra, A., Pelegrí, J. L., Fraile-Nuez, E., Benítez-Barrios, V. M., Emelianov, M., Pérez-Hernández, M. D., & Véllez-Belchí, P. (2014). Meridional overturning transports at 7.5°N and 24.5°N in the Atlantic Ocean during 1992–93 and 2010–11. *Progress in Oceanography*, *128*, 98–114. <https://doi.org/10.1016/j.pocean.2014.08.016>
- Hernández-Guerra, A., & Talley, L. D. (2016). Meridional overturning transports at 30°S in the Indian and Pacific Oceans in 2002–2003 and 2009. *Progress in Oceanography*, *146*, 89–120. <https://doi.org/10.1016/j.pocean.2016.06.005>
- Hernández-Guerra, A., Talley, L. D., Pelegrí, J. L., Véllez-Belchí, P., Baringer, M. O., Macdonald, A. M., & McDonagh, E. L. (2019). The upper, deep, abyssal and overturning circulation in the Atlantic Ocean at 30°S in 2003 and 2011. *Progress in Oceanography*, *176*, 102136. <https://doi.org/10.1016/j.pocean.2019.102136>
- Hogg, N., Biscaye, P., Gardner, W., & Schmitz, W. J. (1982). On the transport and modification of Antarctic Bottom Water in the Vema Channel. *Journal of Marine Research*, *40*, 231–263.
- Holfort, J., Johnson, K. M., Schneider, B., Siedler, G., & Wallace, D. W. R. (1998). Meridional transport of dissolved inorganic carbon in the South Atlantic Ocean. *Global Biogeochemical Cycles*, *12*(3), 479–499. <https://doi.org/10.1029/98GB01533>
- Holzer, M., DeVries, T., & de Lavergne, C. (2021). Diffusion controls the ventilation of a Pacific Shadow Zone above abyssal overturning. *Nature Communications*, *12*(1), 4348. <https://doi.org/10.1038/s41467-021-24648-x>

- Jeansson, E., Olsen, A., Eldevik, T., Skjelvan, I., Omar, A. M., Lauvset, S. K., et al. (2011). The Nordic Seas carbon budget: Sources, sinks, and uncertainties. *Global Biogeochemical Cycles*, 25(4), GB4010. <https://doi.org/10.1029/2010GB003961>
- Johns, W. E., Baringer, M. O., Beal, L. M., Cunningham, S. A., Kanzow, T., Bryden, H. L., et al. (2011). Continuous, array-based estimates of Atlantic Ocean heat transport at 26.5°N. *Journal of Climate*, 24(10), 2429–2449. <https://doi.org/10.1175/2010JCLI3997.1>
- Kersalé, M., Meinen, C. S., Perez, R. C., le Hénaff, M., Valla, D., Lamont, T., et al. (2020). Highly variable upper and abyssal overturning cells in the South Atlantic. *Science Advances*, 6(32), eaba7573. <https://doi.org/10.1126/sciadv.aba7573>
- Key, R. M., Olsen, A., van Heuven, S., Lauvset, S. K., Velo, A., Lin, X., et al. (2015). *Global Ocean data Analysis project, version 2 (GLODAPv2). ORNL/CDIAC-162, NDP-093. In Oak Ridge, Tennessee: Carbon Dioxide Information Analysis Center* (Vol. 8). Oak Ridge National Laboratory, US Department of Energy. [https://doi.org/10.3334/CDIAC/OTG.NDP093\\_GLODAPv2](https://doi.org/10.3334/CDIAC/OTG.NDP093_GLODAPv2)
- Khatiwal, S., Primeau, F., & Hall, T. (2009). Reconstruction of the history of anthropogenic CO<sub>2</sub> concentrations in the ocean. *Nature*, 462(7271), 346–349. <https://doi.org/10.1038/nature08526>
- Khatiwal, S., Tanhua, T., Mikaloff Fletcher, S. E., Gerber, M., Doney, S. C., Graven, H. D., et al. (2013). Global ocean storage of anthropogenic carbon. *Biogeosciences*, 10(4), 2169–2191. <https://doi.org/10.5194/bg-10-2169-2013>
- Lauvset, S. K., Lange, N., Tanhua, T., Bittig, H. C., Olsen, A., Kozyr, A., et al. (2021). An updated version of the global interior ocean biogeochemical data product, GLODAPv2.2021. *Earth System Science Data*, 13(12), 5565–5589. <https://doi.org/10.5194/essd-13-5565-2021>
- Lherminier, P., Mercier, H., Huck, T., Gourcuff, C., Pérez, F. F., Morin, P., et al. (2010). The Atlantic Meridional Overturning Circulation and the subpolar gyre observed at the A25-OVIDE section in June 2002 and 2004. *Deep Sea Research Part I: Oceanographic Research Papers*, 57(11), 1374–1391. <https://doi.org/10.1016/j.dsr.2010.07.009>
- Lumpkin, R., & Speer, K. G. (2007). Global Ocean Meridional Overturning. *Journal of Physical Oceanography*, 37(10), 2550–2562. <https://doi.org/10.1175/jpo3130.1>
- Macdonald, A. M., Baringer, M. O., Wanninkhof, R., Lee, K., & Wallace, D. W. R. (2003). A 1998–1992 comparison of inorganic carbon and its transport across 24.5°N in the Atlantic. *Deep Sea Research Part II: Topical Studies in Oceanography*, 50(22–26), 3041–3064. <https://doi.org/10.1016/j.dsr2.2003.07.009>
- Macdonald, A. M., & Wunsch, C. (1996). An estimate of global ocean circulation and heat fluxes. *Nature*, 382(6590), 436–439. <https://doi.org/10.1038/382436a0>
- Matear, R. J., Wong, C. S., & Xie, L. (2003). Can CFCs be used to determine anthropogenic CO<sub>2</sub>? *Global Biogeochemical Cycles*, 17(1). <https://doi.org/10.1029/2001GB001415>
- Maze, G., Mercier, H., Thierry, V., Memery, L., Morin, P., & Perez, F. F. (2012). Mass, nutrient and oxygen budgets for the northeastern Atlantic Ocean. *Biogeosciences*, 9(10), 4099–4113. <https://doi.org/10.5194/bg-9-4099-2012>
- McCarthy, G. D., Smeed, D. A., Johns, W. E., Frajka-Williams, E., Moat, B. I., Rayner, D., et al. (2015). Measuring the Atlantic Meridional Overturning Circulation at 26°N. *Progress in Oceanography*, 130, 91–111. <https://doi.org/10.1016/j.pocean.2014.10.006>
- McDonagh, E. L., King, B. A., Bryden, H. L., Courtois, P., Szuts, Z., Baringer, M. O., et al. (2015). Continuous estimate of Atlantic oceanic freshwater flux at 26.5°N. *Journal of Climate*, 28(22), 8888–8906. <https://doi.org/10.1175/jcli-d-14-00519.1>
- Mercier, H., Lherminier, P., Sarafanov, A., Gaillard, F., Daniault, N., Desbruyères, D. G., et al. (2015). Variability of the meridional overturning circulation at the Greenland–Portugal OVIDE section from 1993 to 2010. *Progress in Oceanography*, 132, 250–261. <https://doi.org/10.1016/j.pocean.2013.11.001>
- Mikaloff Fletcher, S. E., Gruber, N., Jacobson, A. R., Doney, S. C., Dutkiewicz, S., Gerber, M., et al. (2006). Inverse estimates of anthropogenic CO<sub>2</sub> uptake, transport, and storage by the ocean. *Global Biogeochemical Cycles*, 20(2), GB2002. <https://doi.org/10.1029/2005GB002530>
- Morgan, E. J. (2021). Monthly average air-sea fluxes of O<sub>2</sub>, CO<sub>2</sub>, and N<sub>2</sub> from Earth System Models. *Zenodo*. <https://doi.org/10.5281/zenodo.4716840>
- Morgan, E. J., Manizza, M., Keeling, R. F., Resplandy, L., Mikaloff-Fletcher, S. E., Nevison, C. D., et al. (2021). An atmospheric constraint on the seasonal air-sea exchange of oxygen and heat in the extratropics. *Journal of Geophysical Research: Oceans*, 126(8), 1–20. <https://doi.org/10.1029/2021JC017510>
- Morris, M. Y., Hall, M. M., st. Laurent, L. C., & Hogg, N. G. (2001). Abyssal mixing in the Brazil Basin. *Journal of Physical Oceanography*, 31(11), 3331–3348. [https://doi.org/10.1175/1520-0485\(2001\)031<3331:AMITBB>2.0.CO;2](https://doi.org/10.1175/1520-0485(2001)031<3331:AMITBB>2.0.CO;2)
- Munk, W. H. (1966). Abyssal recipes. *Deep-Sea Research*, 13(4), 707–730. [https://doi.org/10.1016/0011-7471\(66\)90602-4](https://doi.org/10.1016/0011-7471(66)90602-4)
- Murata, A., Kumamoto, Y., Sasaki, K., Watanabe, S., & Fukasawa, M. (2008). Decadal increases of anthropogenic CO<sub>2</sub> in the subtropical South Atlantic Ocean along 30°S. *Journal of Geophysical Research*, 113(C6), C06007. <https://doi.org/10.1029/2007JC004424>
- Olsen, A., Key, R. M., van Heuven, S., Lauvset, S. K., Velo, A., Lin, X., et al. (2016). The Global Ocean Data Analysis project version 2 (GLODAPv2)—An internally consistent data product for the world ocean. *Earth System Science Data*, 8(2), 297–323. <https://doi.org/10.5194/essd-8-297-2016>
- Orsi, A. H., Smethie, W. M., Jr., & Bullister, J. L. (2002). On the total input of Antarctic waters to the deep ocean: A preliminary estimate from chlorofluorocarbon measurements. *Journal of Geophysical Research*, 107(C8), 3122. <https://doi.org/10.1029/2001JC000976>
- Pérez, F. F., Fontela, M., García-Ibáñez, M. I., Mercier, H., Velo, A., Lherminier, P., et al. (2018). Meridional Overturning Circulation conveys fast acidification to the deep Atlantic Ocean. *Nature*, 554(7693), 515–518. <https://doi.org/10.1038/nature25493>
- Pérez, F. F., Mercier, H., Vázquez-Rodríguez, M., Lherminier, P., Velo, A., Pardo, P. C., et al. (2013). Atlantic Ocean CO<sub>2</sub> uptake reduced by weakening of the Meridional Overturning Circulation. *Nature Geoscience*, 6(2), 146–152. <https://doi.org/10.1038/ngeo1680>
- Pérez, F. F., Vázquez-Rodríguez, M., Louarn, E., Padín, X. A., Mercier, H., & Ríos, A. F. (2008). Temporal variability of the anthropogenic CO<sub>2</sub> storage in the Irminger Sea. *Biogeosciences*, 5(6), 1669–1679. <https://doi.org/10.5194/bg-5-1669-2008>
- Racapé, V., Zunino, P., Mercier, H., Lherminier, P., Bopp, L., Pérez, F. F., & Gehlen, M. (2018). Transport and storage of anthropogenic C in the North Atlantic Subpolar Ocean. *Biogeosciences*, 15(14), 4661–4682. <https://doi.org/10.5194/bg-15-4661-2018>
- Reid, J. L. (1989). On the total geostrophic circulation of the South Atlantic Ocean: Flow patterns, tracers and transports. *Progress in Oceanography*, 23(3), 149–244. [https://doi.org/10.1016/0079-6611\(89\)90001-3](https://doi.org/10.1016/0079-6611(89)90001-3)
- Reid, J. L. (1994). On the total geostrophic circulation of the North Atlantic Ocean: Flow patterns, tracers and transports. *Progress in Oceanography*, 33, 1–92. [https://doi.org/10.1016/0079-6611\(94\)90014-0](https://doi.org/10.1016/0079-6611(94)90014-0)
- Ríos, A. F., Vázquez-Rodríguez, M., Padín, X. A., & Pérez, F. F. (2010). Anthropogenic carbon dioxide in the South Atlantic western basin. *Journal of Marine Systems*, 83(1–2), 38–44. <https://doi.org/10.1016/j.jmarsys.2010.06.010>
- Ríos, A. F., Velo, A., Pardo, P. C., Hoppema, M., & Pérez, F. F. (2012). An update of anthropogenic CO<sub>2</sub> storage rates in the western South Atlantic basin and the role of Antarctic Bottom Water. *Journal of Marine Systems*, 94, 197–203. <https://doi.org/10.1016/j.jmarsys.2011.11.023>
- Rosón, G. (2003). Carbon distribution, fluxes, and budgets in the subtropical North Atlantic Ocean (24.5°N). *Journal of Geophysical Research*, 108(C5), 3144. <https://doi.org/10.1029/1999JC000047>

- Sabine, C. L., Feely, R. A., Gruber, N., Key, R. M., Lee, K., Bullister, J. L., et al. (2004). The Oceanic sink for anthropogenic CO<sub>2</sub>. *Science*, 305(5682), 367–371. <https://doi.org/10.1126/science.1097403>
- Sabine, C. L., Feely, R. A., Key, R. M., Wanninkhof, R., Millero, F. J., & Kozyr, A. (2004). GLObal Ocean Data Analysis Project (GLODAP) version 1.1 (NCEI Accession 0001644) [Dataset]. NOAA National Centers for Environmental Information. <https://doi.org/10.25921/pkjs-5w29>
- Steinfeldt, R., Rhein, M., Bullister, J. L., & Tanhua, T. (2009). Inventory changes in anthropogenic carbon from 1997–2003 in the Atlantic Ocean between 20°S and 65°N. *Global Biogeochemical Cycles*, 23(3). <https://doi.org/10.1029/2008GB003311>
- Stendardo, I., & Gruber, N. (2012). Oxygen trends over five decades in the North Atlantic. *Journal of Geophysical Research*, 117(C11), C11004. <https://doi.org/10.1029/2012JC007909>
- Tanhua, T., Biastoch, A., Körtzinger, A., Lüger, H., Böning, C., & Wallace, D. W. R. (2006). Changes of anthropogenic CO<sub>2</sub> and CFCs in the North Atlantic between 1981 and 2004. *Global Biogeochemical Cycles*, 20(4). <https://doi.org/10.1029/2006GB002695>
- Tanhua, T., Jones, E. P., Jeansson, E., Jutterström, S., Smethie, W. M., Wallace, D. W. R., & Anderson, L. G. (2009). Ventilation of the Arctic Ocean: Mean ages and inventories of anthropogenic CO<sub>2</sub> and CFC-11. *Journal of Geophysical Research*, 114(C1), C01002. <https://doi.org/10.1029/2008JC004868>
- Thomas, H., & Ittekkot, V. (2001). Determination of anthropogenic CO<sub>2</sub> in the North Atlantic Ocean using water mass ages and CO<sub>2</sub> equilibrium chemistry. *Journal of Marine Systems*, 27(4), 325–336. [https://doi.org/10.1016/S0924-7963\(00\)00077-4](https://doi.org/10.1016/S0924-7963(00)00077-4)
- Touratier, F., Azouzi, L., & Goyet, C. (2007). CFC-11, Δ14C and 3H tracers as a means to assess anthropogenic CO<sub>2</sub> concentrations in the ocean. *Tellus B: Chemical and Physical Meteorology*, 59(2), 318–325. <https://doi.org/10.1111/j.1600-0889.2006.00247.x>
- Tynan, E., Griffiths, A. M., Fry, C. H., Garley, R., Clarke, J. S., Humphreys, M. P., & Achterberg, E. P. (2016). *Seawater dissolved inorganic carbon and total alkalinity for RAGNARoCC/OSNAP cruise JR302*. British Oceanographic Data Centre, Natural Environment Research Council. <https://doi.org/10.5285/29ea7e19-d89c-3ab1-e053-6c86abc0284b>
- Vázquez-Rodríguez, M., Padin, X. A., Pardo, P. C., Ríos, A. F., & Pérez, F. F. (2012). The subsurface layer reference to calculate preformed alkalinity and air–sea CO<sub>2</sub> disequilibrium in the Atlantic Ocean. *Journal of Marine Systems*, 94, 52–63. <https://doi.org/10.1016/j.jmarsys.2011.10.008>
- Vázquez-Rodríguez, M., Padin, X. A., Ríos, A. F., Bellerby, R. G. J., & Pérez, F. F. (2009). An upgraded carbon-based method to estimate the anthropogenic fraction of dissolved CO<sub>2</sub> in the Atlantic Ocean. *Biogeosciences Discussions*, 6(2), 4527–4571. <https://doi.org/10.5194/bgd-6-4527-2009>
- Vázquez-Rodríguez, M., Touratier, F., Io Monaco, C., Waugh, D. W., Padin, X. A., Bellerby, R. G. J., et al. (2009). Anthropogenic carbon distributions in the Atlantic Ocean: Data-based estimates from the Arctic to the Antarctic. *Biogeosciences*, 6(3), 439–451. <https://doi.org/10.5194/bg-6-439-2009>
- Waugh, D. W., Hall, T. M., McNeil, B. I., Key, R., & Matear, R. J. (2006). Anthropogenic CO<sub>2</sub> in the oceans estimated using transit time distributions. *Tellus B: Chemical and Physical Meteorology*, 58(5), 376–389. <https://doi.org/10.1111/j.1600-0889.2006.00222.x>
- Wijffels, S. E. (2001). Chapter 6.2 Ocean transport of fresh water. In G. Siedler, J. Church, & J. Gould (Eds.), *Ocean circulation & climate: Observing and modelling the Global Ocean* (pp. 475–488). Academic Press. [https://doi.org/10.1016/S0074-6142\(01\)80135-2](https://doi.org/10.1016/S0074-6142(01)80135-2)
- Worthington, E. L., Moat, B. I., Smeed, D. A., Mecking, J. v., Marsh, R., & McCarthy, G. D. (2021). A 30-year reconstruction of the Atlantic Meridional Overturning Circulation shows no decline. *Ocean Science*, 17(1), 285–299. <https://doi.org/10.5194/os-17-285-2021>
- Wunsch, C. (1996). *The Ocean circulation inverse problem*. Cambridge University Press.
- Zunino, P., Pérez, F. F., Fajar, N. M., Guallart, E. F., Ríos, A. F., Pelegrí, J. L., & Hernández-Guerra, A. (2015). Transports and budgets of anthropogenic CO<sub>2</sub> in the tropical North Atlantic in 1992–1993 and 2010–2011. *Global Biogeochemical Cycles*, 29(7), 1075–1091. <https://doi.org/10.1002/2014GB005075>

*Global Biogeochemical Cycles*

Supporting Information for

**Anthropogenic Carbon Transport Variability in the Atlantic Ocean over Three Decades**

Verónica Caínzos<sup>1</sup>, Antón Velo<sup>2</sup>, Fiz F. Pérez<sup>2</sup> and Alonso Hernández-Guerra<sup>1</sup>

<sup>1</sup> Unidad Océano y Clima, Instituto de Oceanografía y Cambio Global, IOCAG, Universidad de Las Palmas de Gran Canaria, ULPGC, Unidad Asociada ULPGC-CSIC, Canary Islands, Spain.

<sup>2</sup> Instituto de Investigaciones Marinas, CSIC, Eduardo Cabello 6, 36208 Vigo, Spain.

**Contents of this file**

Text S1 to S3

Figures S1 to S5

Tables S1 to S11

### **Text S1. Configuration of the inverse model**

Inverse models solve the equation  $\mathbf{Ax}=-\mathbf{Y}$ , where  $A$  is a matrix of mass and property concentrations with size  $M$  (number of layers) by  $N$  (number of unknowns),  $x$  is a column vector of length  $N$  that contains the unknowns of the system (i.e., velocities at the reference level, Ekman transport adjustment, biogeochemical budget adjustments, ...), and  $Y$  is a column vector of length  $M$  containing the initial unbalanced transports of mass and properties for each equation defined in  $A$ . This equation can be expressed in its matrix form as shown below. The matrix is a representation for a single box between two contiguous sections. Each property being conserved is represented with different colors. In this case,  $n$  is the number of pair of stations for section A;  $m$  is the number of pair of stations for section B;  $q$  is the number of layers. In the below matrix,  $e$  stands for mass and  $y$  for mass transport;  $s$  for salt and  $z$  for salt transport;  $f$  stands for oxygen and  $k$  for oxygen transport;  $g$  for nitrate and  $r$  for nitrate transport;  $h$  for silicate and  $t$  for silicate transport and, finally,  $j$  stands for phosphate and  $u$  for phosphate transport. For each single section, we applied regional constraints to mass ( $_{reg}$ ) and, in addition to mass, we have also constraint the salinity content of each single section A and B. Using this tracer instead of mass allows for changes in freshwater across the section while still conserving mass. For each box, the net transport of mass, oxygen, nitrate, silicate and phosphate is conserved.

The inverse solutions provide the velocities at the reference level ( $b$ ) for each pair station of each section. Ekman transport ( $T_{Ek}$ ) is applied for the equations of all properties balancing the net transport among both sections and the transport across the first layer of a single section. Its adjustment ( $\Delta T_{Ek}$ ) is part of the unknowns solved for each section. The oxygen influx from the air-sea interphase is included in the first layer of oxygen conservation ( $F_{a-s}$ ), and its adjustment included as part of the solutions ( $\Delta F_{a-s}$ ). To allow changes in the water column due to the non-conservative sources and sinks of oxygen we have added the term  $B_{O_2}$ , that reflects the changes in oxygen in the water column and estimated its adjustment  $\Delta B_{O_2}$ . We have associated changes in oxygen with those for nitrate, silicate and phosphate with the Redfield ratio ( $r_{NO}$ ,  $r_{SiO}$  and  $r_{PO}$  for nitrate, silicate and phosphate, respectively). More detail on the inverse model configuration can be found in Supporting Information Text S1 in Caínzos et al. (2022).

$$\begin{pmatrix}
e_{A_{t,1}} & \cdots & e_{A_{t,n}} & e_{B_{t,1}} & \cdots & e_{B_{t,m}} & 1 & 1 & 0 & 0 & 0 & \cdots & 0 & 0 \\
e_{A_{\text{reg}}} & \cdots & e_{A_{\text{reg}}} & 0 & \cdots & 0 & 0 & 0 & 0 & 0 & 0 & \cdots & 0 & 0 \\
0 & \cdots & 0 & e_{B_{\text{reg}}} & \cdots & e_{B_{\text{reg}}} & 0 & 0 & 0 & 0 & 0 & \cdots & 0 & 0 \\
e_{A_{1,1}} & \cdots & e_{A_{1,n}} & e_{B_{1,1}} & \cdots & e_{B_{1,m}} & 1 & 1 & 0 & 0 & 0 & \cdots & 0 & 0 \\
e_{A_{2,1}} & \cdots & e_{A_{2,n}} & e_{B_{2,1}} & \cdots & e_{B_{2,m}} & 0 & 0 & 0 & 0 & 0 & \cdots & 0 & 0 \\
\vdots & \ddots & \vdots & \vdots & \ddots & \vdots & \vdots & \vdots & \vdots & \vdots & \vdots & \ddots & \vdots & \vdots \\
e_{A_{q-1,1}} & \cdots & e_{A_{q-1,n}} & e_{B_{q-1,1}} & \cdots & e_{B_{q-1,m}} & 0 & 0 & 0 & 0 & 0 & \cdots & 0 & 0 \\
e_{A_{q,1}} & \cdots & e_{A_{q,n}} & e_{B_{q,1}} & \cdots & e_{B_{q,m}} & 0 & 0 & 0 & 0 & 0 & \cdots & 0 & 0 \\
s_{A_{t,1}} & \cdots & s_{A_{t,n}} & 0 & \cdots & 0 & \left(\frac{s_{A_1}}{e_{A_1}}\right) & 0 & 0 & 0 & 0 & \cdots & 0 & 0 \\
0 & \cdots & 0 & s_{B_{t,1}} & \cdots & s_{B_{t,m}} & 0 & \left(\frac{s_{B_1}}{e_{B_1}}\right) & 0 & 0 & 0 & \cdots & 0 & 0 \\
f_{A_{1,1}} & \cdots & f_{A_{1,n}} & f_{B_{1,1}} & \cdots & f_{B_{1,m}} & \left(\frac{f_{A_1}}{e_{A_1}}\right) & \left(\frac{f_{B_1}}{e_{B_1}}\right) & 1 & 1 & 0 & \cdots & 0 & 0 \\
f_{A_{2,1}} & \cdots & f_{A_{2,n}} & f_{B_{2,1}} & \cdots & f_{B_{2,m}} & 0 & 0 & 0 & 0 & 1 & \cdots & 0 & 0 \\
\vdots & \ddots & \vdots & \vdots & \ddots & \vdots & \vdots & \vdots & \vdots & \vdots & \vdots & \ddots & \vdots & \vdots \\
f_{A_{q-1,1}} & \cdots & f_{A_{q-1,n}} & f_{B_{q-1,1}} & \cdots & f_{B_{q-1,m}} & 0 & 0 & 0 & 0 & 0 & \cdots & 1 & 0 \\
f_{A_{q,1}} & \cdots & f_{A_{q,n}} & f_{B_{q,1}} & \cdots & f_{B_{q,m}} & 0 & 0 & 0 & 0 & 0 & \cdots & 0 & 1 \\
g_{A_{1,1}} & \cdots & g_{A_{1,n}} & g_{B_{1,1}} & \cdots & g_{B_{1,m}} & \left(\frac{g_{A_1}}{e_{A_1}}\right) & \left(\frac{g_{B_1}}{e_{B_1}}\right) & 0 & r_{\text{NO}} & 0 & \cdots & 0 & 0 \\
g_{A_{2,1}} & \cdots & g_{A_{2,n}} & g_{B_{2,1}} & \cdots & g_{B_{2,m}} & 0 & 0 & 0 & 0 & r_{\text{NO}} & \cdots & 0 & 0 \\
\vdots & \ddots & \vdots & \vdots & \ddots & \vdots & \vdots & \vdots & \vdots & \vdots & \vdots & \ddots & \vdots & \vdots \\
g_{A_{q-1,1}} & \cdots & g_{A_{q-1,n}} & g_{B_{q-1,1}} & \cdots & g_{B_{q-1,m}} & 0 & 0 & 0 & 0 & 0 & \cdots & r_{\text{NO}} & 0 \\
g_{A_{q,1}} & \cdots & g_{A_{q,n}} & g_{B_{q,1}} & \cdots & g_{B_{q,m}} & 0 & 0 & 0 & 0 & 0 & \cdots & 0 & r_{\text{NO}} \\
h_{A_{1,1}} & \cdots & h_{A_{1,n}} & h_{B_{1,1}} & \cdots & h_{B_{1,m}} & \left(\frac{h_{A_1}}{e_{A_1}}\right) & \left(\frac{h_{B_1}}{e_{B_1}}\right) & 0 & r_{\text{SiO}} & 0 & \cdots & 0 & 0 \\
h_{A_{2,1}} & \cdots & h_{A_{2,n}} & h_{B_{2,1}} & \cdots & h_{B_{2,m}} & 0 & 0 & 0 & 0 & r_{\text{SiO}} & \cdots & 0 & 0 \\
\vdots & \ddots & \vdots & \vdots & \ddots & \vdots & \vdots & \vdots & \vdots & \vdots & \vdots & \ddots & \vdots & \vdots \\
h_{A_{q-1,1}} & \cdots & h_{A_{q-1,n}} & h_{B_{q-1,1}} & \cdots & h_{B_{q-1,m}} & 0 & 0 & 0 & 0 & 0 & \cdots & r_{\text{SiO}} & 0 \\
h_{A_{q,1}} & \cdots & h_{A_{q,n}} & h_{B_{q,1}} & \cdots & h_{B_{q,m}} & 0 & 0 & 0 & 0 & 0 & \cdots & 0 & r_{\text{SiO}} \\
j_{A_{1,1}} & \cdots & j_{A_{1,n}} & j_{B_{1,1}} & \cdots & j_{B_{1,m}} & \left(\frac{j_{A_1}}{e_{A_1}}\right) & \left(\frac{j_{B_1}}{e_{B_1}}\right) & 0 & r_{\text{PO}} & 0 & \cdots & 0 & 0 \\
j_{A_{2,1}} & \cdots & j_{A_{2,n}} & j_{B_{2,1}} & \cdots & j_{B_{2,m}} & 0 & 0 & 0 & 0 & r_{\text{PO}} & \cdots & 0 & 0 \\
\vdots & \ddots & \vdots & \vdots & \ddots & \vdots & \vdots & \vdots & \vdots & \vdots & \vdots & \ddots & \vdots & \vdots \\
j_{A_{q-1,1}} & \cdots & j_{A_{q-1,n}} & j_{B_{q-1,1}} & \cdots & j_{B_{q-1,m}} & 0 & 0 & 0 & 0 & 0 & \cdots & r_{\text{PO}} & 0 \\
j_{A_{q,1}} & \cdots & j_{A_{q,n}} & j_{B_{q,1}} & \cdots & j_{B_{q,m}} & 0 & 0 & 0 & 0 & 0 & \cdots & 0 & r_{\text{PO}}
\end{pmatrix}
\begin{pmatrix}
b_{A_1} \\
\vdots \\
b_{B_n} \\
b_{B_1} \\
\vdots \\
b_{B_m} \\
\Delta T_{A_{\text{Ek}}} \\
\Delta T_{B_{\text{Ek}}} \\
\Delta F_{a-s} \\
\Delta B_{O_{21}} \\
\Delta B_{O_{22}} \\
\vdots \\
\Delta B_{O_{2q-1}} \\
\Delta B_{O_{2q}}
\end{pmatrix}
=
\begin{pmatrix}
y_{A_t} + y_{B_t} + T_{A_{\text{Ek}}} + T_{B_{\text{Ek}}} \\
y_{A_{\text{reg}}} \\
y_{B_{\text{reg}}} \\
y_{A_1} + y_{B_1} + T_{A_{\text{Ek}}} + T_{B_{\text{Ek}}} \\
y_{A_2} + y_{B_2} \\
\vdots \\
y_{A_{q-1}} + y_{B_{q-1}} \\
y_{A_q} + y_{B_q} \\
z_{A_t} + T_{A_{\text{Ek}}} \left(\frac{s_{A_1}}{e_{A_1}}\right) \\
z_{B_t} + T_{B_{\text{Ek}}} \left(\frac{s_{B_1}}{e_{B_1}}\right) \\
k_{A_1} + k_{B_1} + T_{A_{\text{Ek}}} \left(\frac{f_{A_1}}{e_{A_1}}\right) + T_{B_{\text{Ek}}} \left(\frac{f_{B_1}}{e_{B_1}}\right) + F_{a-s} + B_{O_{21}} \\
k_{A_2} + k_{B_2} + B_{O_{22}} \\
\vdots \\
k_{A_{q-1}} + k_{B_{q-1}} + B_{O_{2q-1}} \\
k_{A_q} + k_{B_q} + B_{O_{2q}} \\
r_{A_1} + r_{B_1} + T_{A_{\text{Ek}}} \left(\frac{g_{A_1}}{e_{A_1}}\right) + T_{B_{\text{Ek}}} \left(\frac{g_{B_1}}{e_{B_1}}\right) + B_{O_{21}} \cdot r_{\text{NO}} \\
r_{A_2} + r_{B_2} + B_{O_{22}} \cdot r_{\text{NO}} \\
\vdots \\
r_{A_{q-1}} + r_{B_{q-1}} + B_{O_{2q-1}} \cdot r_{\text{NO}} \\
r_{A_q} + r_{B_q} + B_{O_{2q}} \cdot r_{\text{NO}} \\
t_{A_1} + t_{B_1} + T_{A_{\text{Ek}}} \left(\frac{h_{A_1}}{e_{A_1}}\right) + T_{B_{\text{Ek}}} \left(\frac{h_{B_1}}{e_{B_1}}\right) + B_{O_{21}} \cdot r_{\text{SiO}} \\
t_{A_2} + t_{B_2} + B_{O_{22}} \cdot r_{\text{SiO}} \\
\vdots \\
t_{A_{q-1}} + t_{B_{q-1}} + B_{O_{2q-1}} \cdot r_{\text{SiO}} \\
t_{A_q} + t_{B_q} + B_{O_{2q}} \cdot r_{\text{SiO}} \\
u_{A_1} + u_{B_1} + T_{A_{\text{Ek}}} \left(\frac{j_{A_1}}{e_{A_1}}\right) + T_{B_{\text{Ek}}} \left(\frac{j_{B_1}}{e_{B_1}}\right) + B_{O_{21}} \cdot r_{\text{PO}} \\
u_{A_2} + u_{B_2} + B_{O_{22}} \cdot r_{\text{PO}} \\
\vdots \\
u_{A_{q-1}} + u_{B_{q-1}} + B_{O_{2q-1}} \cdot r_{\text{PO}} \\
u_{A_q} + u_{B_q} + B_{O_{2q}} \cdot r_{\text{PO}}
\end{pmatrix}$$

## Text S2. Uncertainty computation

The Gauss-Markov method solves this system of equations with a minimum error variance solution from the initial estimates of the unknowns (the velocities at the reference level,  $b$ , the corrections to the Ekman transport,  $\Delta T_{Ek}$ , the input of  $O_2$  from the atmosphere,  $F_{a-s}$ , and the rate of oxygen consumption along the water column,  $B_{O_2}$ ; Wunsch, 1996). To solve it, we first need a priori estimates and uncertainties that give an initial approximation to the actual value. The preliminary variance of the adjusted velocity at the reference level is  $8 \text{ cm}^2 \text{ s}^{-2}$  for the station pairs closer to coast, where shear is stronger and  $4 \text{ cm}^2 \text{ s}^{-2}$  in the deepest stations. The initial estimates for the mass transport are  $9 \text{ Sv}^2$  for the net mass transport between two sections, therefore allowing for compensation within each box. The a priori biogeochemical imbalances for each box are zero, with a priori uncertainties of  $(500 \text{ kmol s}^{-1})^2$  for oxygen,  $(100 \text{ kmol s}^{-1})^2$  for nitrate and silicate, and  $(10 \text{ kmol s}^{-1})^2$  for phosphate.

For layer conservation, the variance is between 13 and  $1 \text{ Sv}^2$ , decreasing towards deeper layers. The salinity uncertainties are computed as the square of the uncertainty of the Bering Strait transport ( $0.6 \text{ Sv}$ ) times the square of the ration between the total salt transport and the mass transport of each section.

Despite obtaining similar results, this study provides smaller uncertainties than other global inverse solutions (Ganachaud, 2003) and decadal studies (Fu et al., 2020). This was achieved by using physical constraints with a simpler model with only the velocities at the reference level and the Ekman adjustments as unknowns. Moreover, adding the biogeochemical equations has helped reduced these uncertainties by incorporating more information to the matrix without increasing its rank.

### STORAGE RATE UNCERTAINTIES

The storage rates provided by Gruber et al. (2019) are computed between 1994 and 2007. Therefore, the increase rate of 1.9% per decade is valid for this period. We have extended this rate also for the last decade, assuming a tendency in storing more  $C_{anth}$  into the ocean interior. However, recent studies are challenging this assumption, finding for the 2004-2014 decreasing rates in the storage of  $C_{anth}$  in the North Atlantic (Müller et al., 2022). To accommodate these discrepancies, we have decided to increase the uncertainties associated to the storage rates of  $C_{anth}$  for the last decade, without surpassing 15% of the mean value.



### **Text S3. Sensitivity tests**

Several sensitivity tests were conducted to determine the effect of different configurations of the inverse models.

#### **PHYSICAL CONSTRAINTS**

The physical constraints in the model have been assessed previously by Caínzos et al. (2022), where the initial physical-only configuration of the model is described.

For that model, several sensitivity tests were conducted to determine the best configuration of the inverse models. The tightness of the constraints on regional and topographic features of the Southern Hemisphere were assessed by removing the constraints on section A10 (30°S). The results for each constraint appear in the Supporting Information Table S6 from Caínzos et al. (2022). The boundary currents display some differences, but it has not been transmitted to the net heat and freshwater budget, which remain the same, and has not altered the values of the freshwater overturning. The importance of the temporal variability of the Bering Strait salinity and transport was also evaluated (Supporting Information Table S7; Caínzos et al., 2022). Changing the average salinity of the Bering Strait from 31.5 to 33.5 (Woodgate et al., 2005) and the Bering Strait transport for the last two decades from  $-0.8 \pm 0.6$  to  $-1.0 \pm 0.5$  Sv (Woodgate, 2018), only the throughflow component of the freshwater was affected, but not the overturning and horizontal components.

#### **INTERPOLATION OF BIOGEOCHEMICAL DATA IN WATER COLUMN**

The methodology of interpolation of biogeochemical data in the water column is a very important step in the computation of concentration and transports for each section. The selected methodology has been compared against several other methods before choosing the linear interpolation in a neutral density framework with a nearest neighbour extrapolation every 2 dbar. Linear interpolation avoids data appearing in a stair-like manner and nearest extrapolation prevents extreme values from appearing at the surface and bottom. Using a neutral density framework helps redistribute the importance of surface and deep layers in the water column, adjusting the levels by its density than rather just by its position in the water column, which would naturally underrepresent the upper layers. For comparison, we have included results for two different set of interpolation methods: the first one uses a nearest interpolation method instead of linear, and the second one replaces the neutral density framework for a pressure framework. The resulting values are included in Supporting Information Tables S2-S7 under the names 'near int' and 'prs int', respectively. As could be expected, the physical parameters in Supporting Information Tables S2-S4 show non-significant variations in either mass, heat or freshwater transports (with differences of  $\sim 0.1$  Sv,  $\sim 0.03$  PW and 0.03 Sv, respectively) for both interpolation tests. However, we can see differences for each box in the balance of oxygen, nutrients and  $C_T$  (Supporting Information Tables S5-S7). Nearest interpolation imposes large changes in the balance for each box, with a mean of 1100% change for oxygen, 665% for nitrate, 165% for silicate, 504% for phosphate and 8700% for total carbon. These values reduce for the interpolation in a pressure vertical framework, with changes of 378% for oxygen, 548% for nitrate, 103% for silicate, 263% for phosphate and 94% for total carbon.

#### **REDFIELD RATIOS**

The Redfield ratio chosen is consistent with a similar study from Maze et al. (2012), that uses the Redfield ratio reported by Anderson (1995). The inverse models are not very sensible to the Redfield

ratios applied, as it has been set to modulate the weights of the equations, with larger weight applied to physical constraints.

To try to assess the effect of the choice of Redfield ratio in the results, we have computed some sensitivity tests in the form of a Montecarlo experiment with 100 replicas changing the Redfield ratios randomly within 20% of its mean value. Afterwards, the 100 replicas were averaged, and are presented for comparison in Supporting Information Tables S2-S4 for the physical parameters and Tables S5-S7 for the biogeochemical parameters under the name 'TRedf'. We can see that the physical properties (net mass transport, ocean heat content and freshwater flux) for each section are mostly unchanged, and the variance found after the 100 replicas is quite small (with differences of less than 0.1 Sv of mass transport, less than 0.01 PW for heat transport and 0.01 Sv for the net freshwater flux). The mean variances of the mean value of the Montecarlo test over the Atlantic are 0.003 Sv for mass, 0.0007 PW for heat and 0.0005 Sv for freshwater. The biogeochemical properties applied to the model (oxygen, nitrate, silicate and phosphate) show more variability, with differences with respect to the mean of less than 5%, so that the values after the model are within the uncertainties and they have scarcely influenced the DIC budget. The mean variances for the mean value are 7.4 kmol s<sup>-1</sup> for oxygen, 2.5 kmol s<sup>-1</sup> for nitrate, 4.1 kmol s<sup>-1</sup> for silicate, 0.17 kmol s<sup>-1</sup> for phosphate and 0.01 kmol s<sup>-1</sup> for total carbon.

#### SURFACE CONCENTRATION OF C<sub>anth</sub>

Uncertainties for C<sub>anth</sub> transports are obtained after the inverse model results, applying the correction in the velocities at the reference level that modify the mass transport. No Carbon species has been constrained in the model, so any changes in the surface layer are not inherently reproduced in the model-derived uncertainties.

We have tried to investigate how different values in the surface would affect the net C<sub>anth</sub> transports, and therefore have computed other Montecarlo experiment that modifies the surface (depth less than 100 m) C<sub>anth</sub> concentration randomly by 20% and then obtained the net values of C<sub>anth</sub> transport per layer for each section, shown in Supporting Information Tables S8-S10. We can see mainly changes in the upper layer, with very small differences reaching 0.005 PgC yr<sup>-1</sup>. With these results we feel that we have proved that changes in the surface concentration of C<sub>anth</sub> are not affecting significantly to the overall transport of C<sub>anth</sub>.

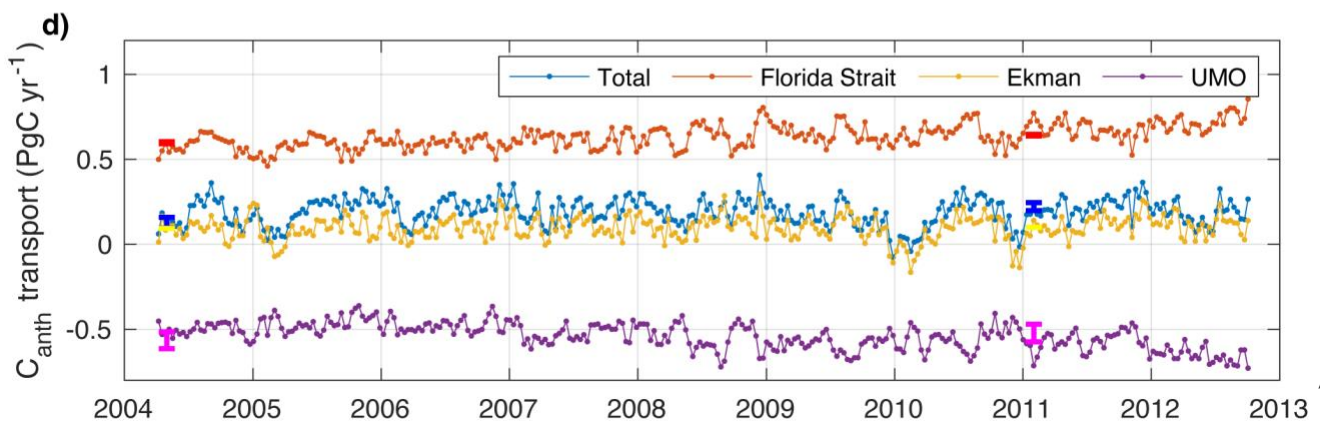
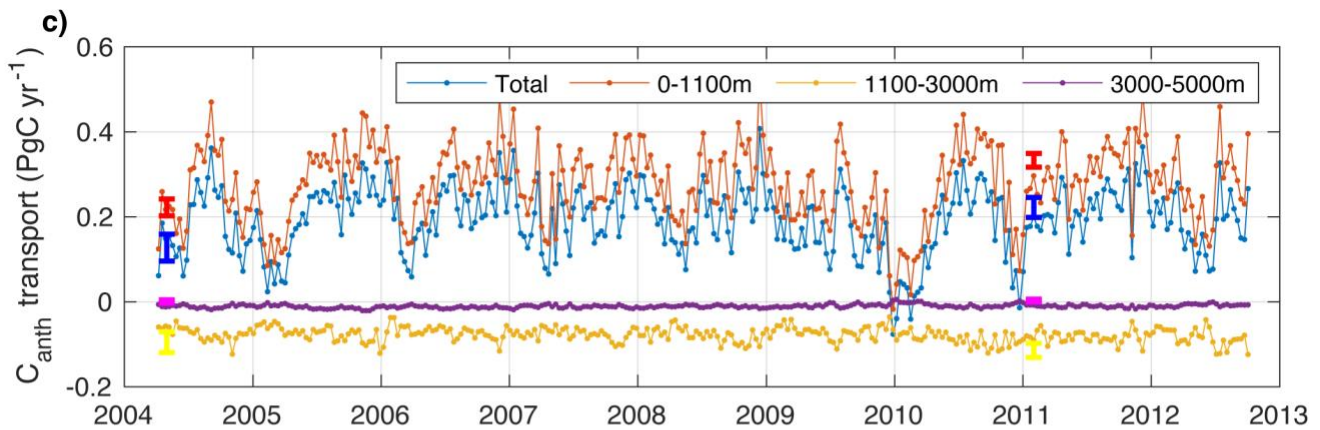
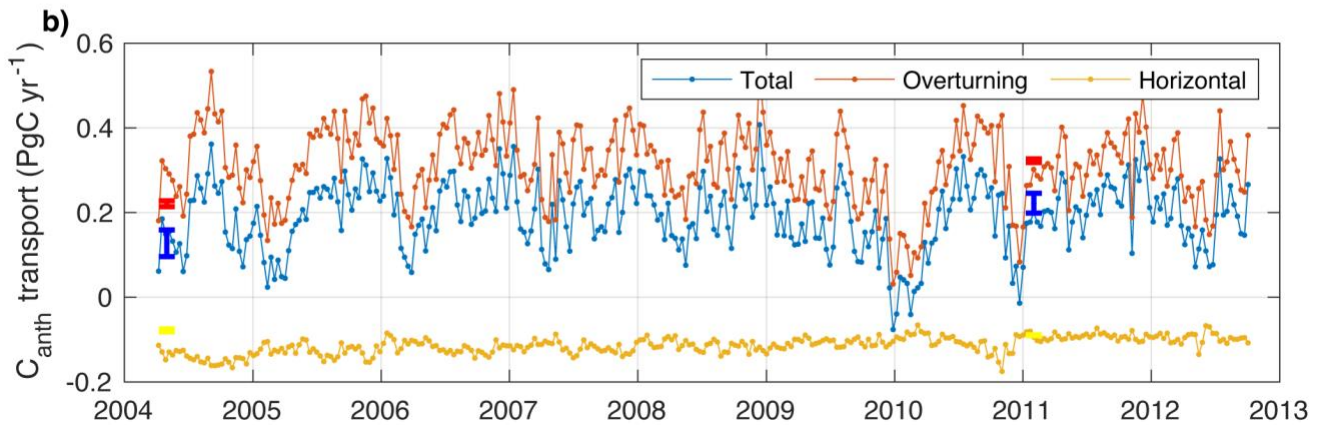
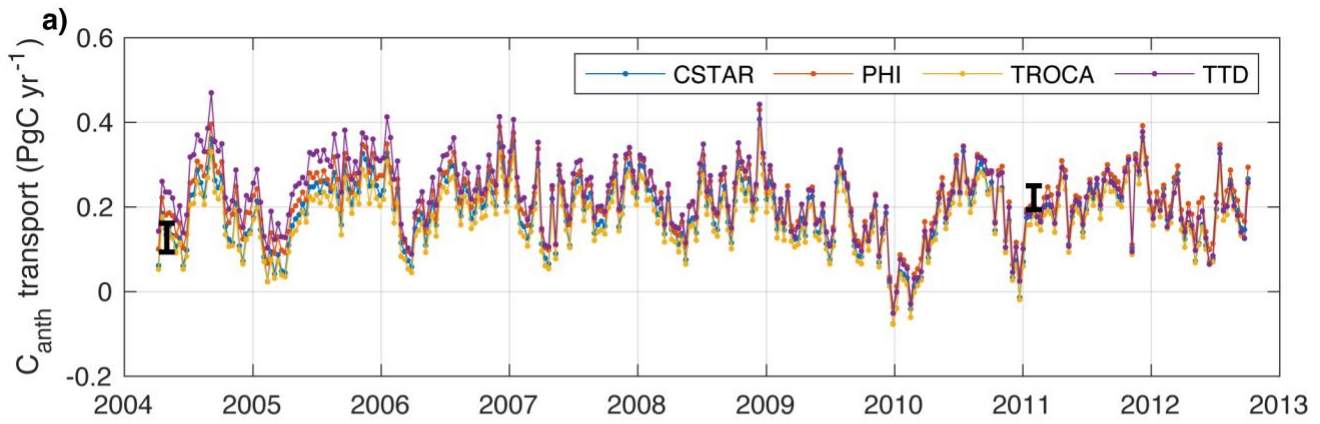


**Figure S1.** Comparison of  $C_{\text{anth}}$  transport for section 24°N of the continuous values from the time series of Brown et al. (2021) from 2004 to 2012 with the inverse solution of this study for 24°N cruises in 2004 and 2011. The comparisons are made attending to different components of the transport (in  $\text{kmol s}^{-1}$ ): a) net  $C_{\text{anth}}$  transport across 24°N compared with time series of  $C_{\text{anth}}$  transport obtained with different methodologies of computation of  $C_{\text{anth}}$  concentration (TTD-methods, and other backcalculation methods as Cstar, TROCA and  $\varphi C_{\text{T}}^0$ ); b) division of  $C_{\text{anth}}$  into its components – overturning and horizontal; c) division into layers attending to the water masses – 0 to 1100 m for upper and thermocline layers, 1100 to 3000 m for deep layers and 3000 to 5000 m for bottom layers; and d) the importance of Florida Straits and Ekman transport to the total  $C_{\text{anth}}$  transport.

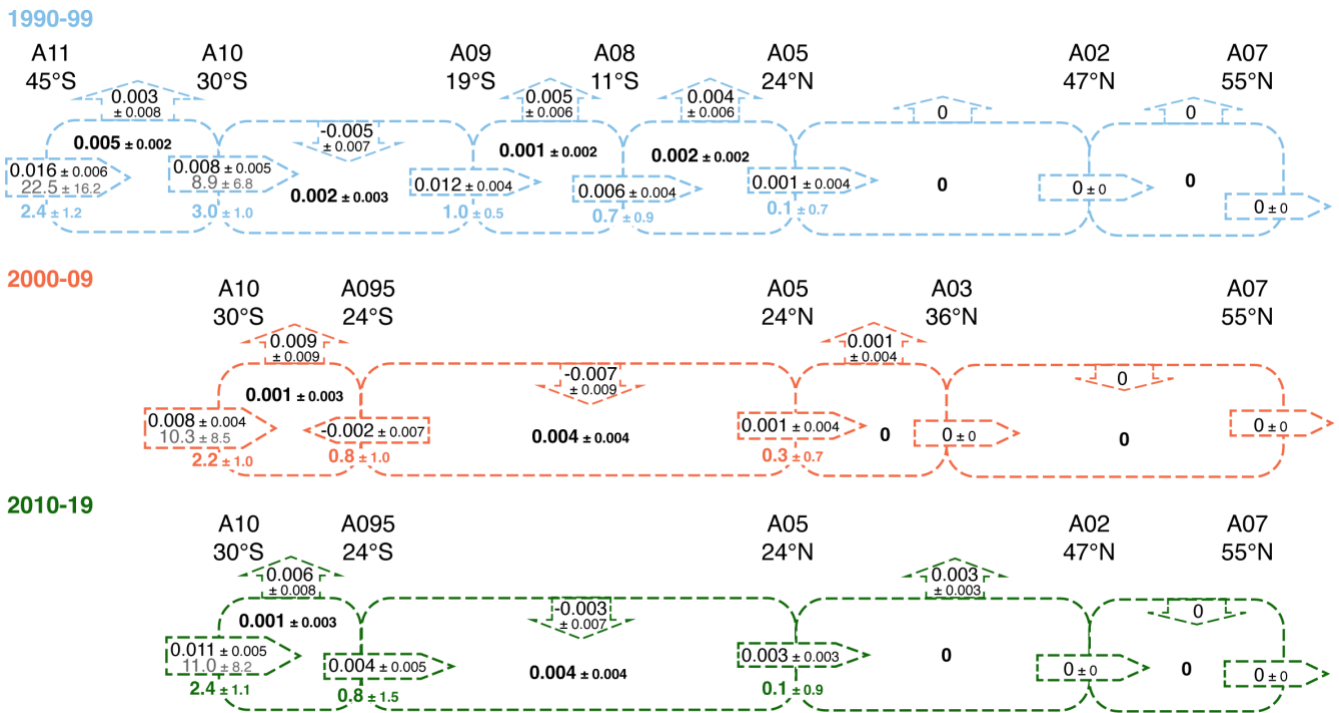


**Figure S2.**  $C_{\text{anth}}$  budget for abyssal layers in the Atlantic Ocean for each box between adjacent sections for each decade, represented by different colors (blue for 1990–99, orange for 2000–09, and green for 2010–19). Each box is delimited on either side by the horizontal  $C_{\text{anth}}$  transport ( $\text{PgC yr}^{-1}$ ) across the section with black regular values, and the mass transport ( $S_v$ ) are the colored bold values outside the arrow. Moreover, the normalized transport-weighted  $C_{\text{anth}}$  ( $\mu\text{mol kg}^{-1}$ ) concentration is also included as the grey values. Within each cell there is a bold black value that determines the  $C_{\text{anth}}$  storage ( $\text{PgC yr}^{-1}$ ) as obtained from Gruber et al. (2019) and Sabine et al. (2004) normalized to the middle of each decade (1995, 2005 and 2015). The vertical arrows at the top of each box are the vertical influx of  $C_{\text{anth}}$  ( $\text{PgC yr}^{-1}$ ).

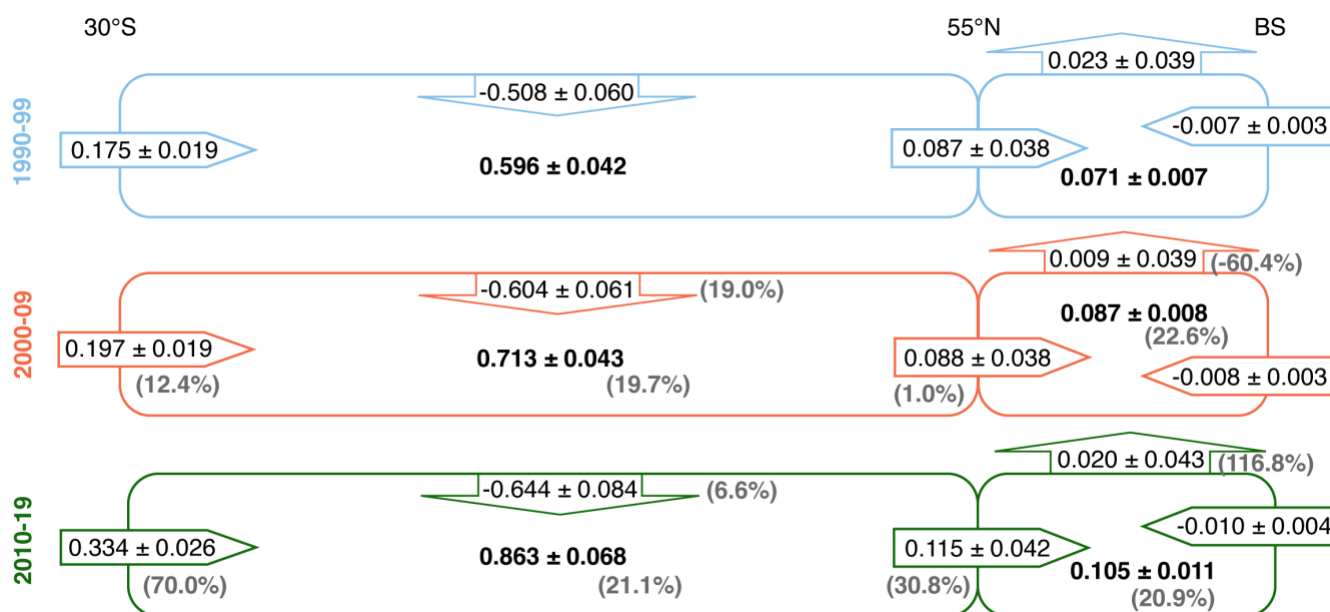


**Figure S3.**  $C_{anth}$  budget for the Atlantic Ocean box and for the box north of 55°N for each decade represented by different colors (blue for 1990–99, orange for 2000–09, and green for 2010–19). Each box is delimited on either side by the horizontal  $C_{anth}$  transport ( $\text{PgC yr}^{-1}$ ) across the section with black regular values. In the cells of the Atlantic box the bold black values determine the  $C_{anth}$  storage ( $\text{PgC yr}^{-1}$ ) as obtained from Gruber et al. (2019) and Sabine et al. (2004) normalized to the middle of each decade (1995, 2005 and 2015). North of 55°N, the  $C_{anth}$  storage is the combination of the estimations from Gruber et al. (2019) and Sabine et al. (2004) between 55°N and the Sills (~63-66°N), and the values of  $0.018 \pm 0.04 \text{ PgC yr}^{-1}$  in the Nordic Seas between 63-66 and 78°N (Jeansson et al., 2011) and  $0.043 \pm 0.04 \text{ PgC yr}^{-1}$  in the Arctic Seas between 78°N and the Bering Strait (Tanhua et al., 2009), normalized to 2005. The vertical arrows at the top of each box are the vertical influx of  $C_{anth}$  ( $\text{PgC yr}^{-1}$ ). The grey numbers within parenthesis represent the percentage of change between the 2000-09 and 1990-99 decades for the ones in the middle panel for the horizontal transport, storage and air-sea flux, and the change between the 2010-19 and 2000-09 decades for the bottom panel.

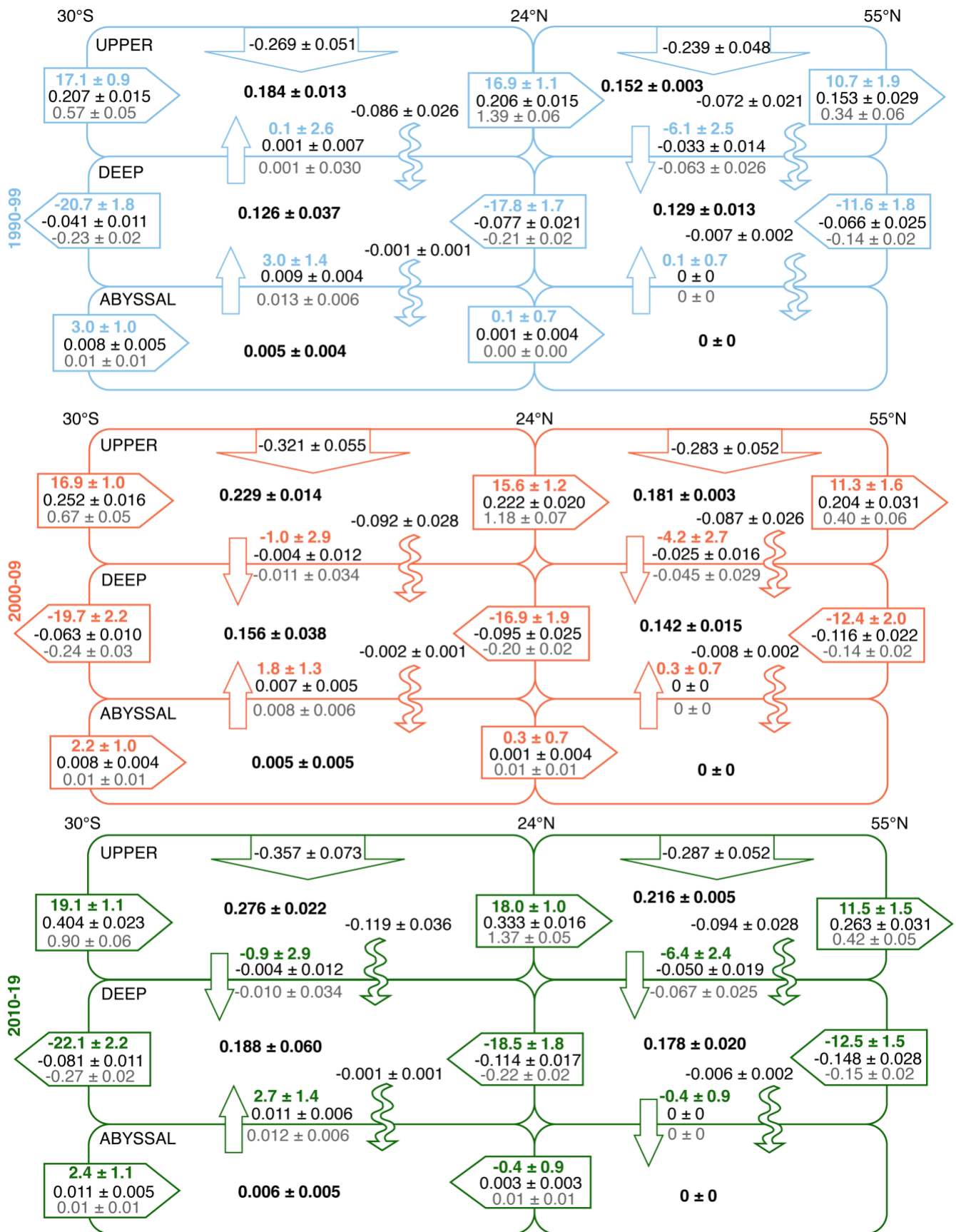


**Figure S4.**  $C_{\text{anth}}$  budget in the Atlantic Ocean for two superboxes – 30°S to 24°N and 24 to 55°N for each decade, represented by different colors (blue for 1990–99, orange for 2000–09, and green for 2010–19). For each decade, the upper boxes, represent the values for the upper layer, the middle boxes the deep layers and the bottom boxes represent the abyssal layers. Each box is delimited on either side by the horizontal transport across the section, specifying the transport of different properties:  $C_{\text{anth}}$  transport ( $\text{PgC yr}^{-1}$ ) appears with black regular values, heat transport (PW) are the grey regular values, and the mass transport (Sv) are the colored bold values. The strait arrows at the interphase between upper and deep and deep and abyssal layers represent the exchange due to the vertical advection of mass across the layers. The properties associated to this vertical advection are the same as for the horizontal transport. The wiggly arrows correspond to the vertical diffusion across the interphase due to differences in the vertical derivative of  $C_{\text{anth}}$  concentration, with the values for  $C_{\text{anth}}$  diffusion transport in black regular font. Within each cell there is a bold black value that determines the  $C_{\text{anth}}$  storage ( $\text{PgC yr}^{-1}$ ) as obtained from Gruber et al. (2019) and Sabine et al. (2004) normalized to middle of each decade (1995, 2005 and 2015). The vertical arrows at the top of the upper box are the vertical influx of  $C_{\text{anth}}$  ( $\text{PgC yr}^{-1}$ ), namely the atmospheric input for the net and upper boxes.



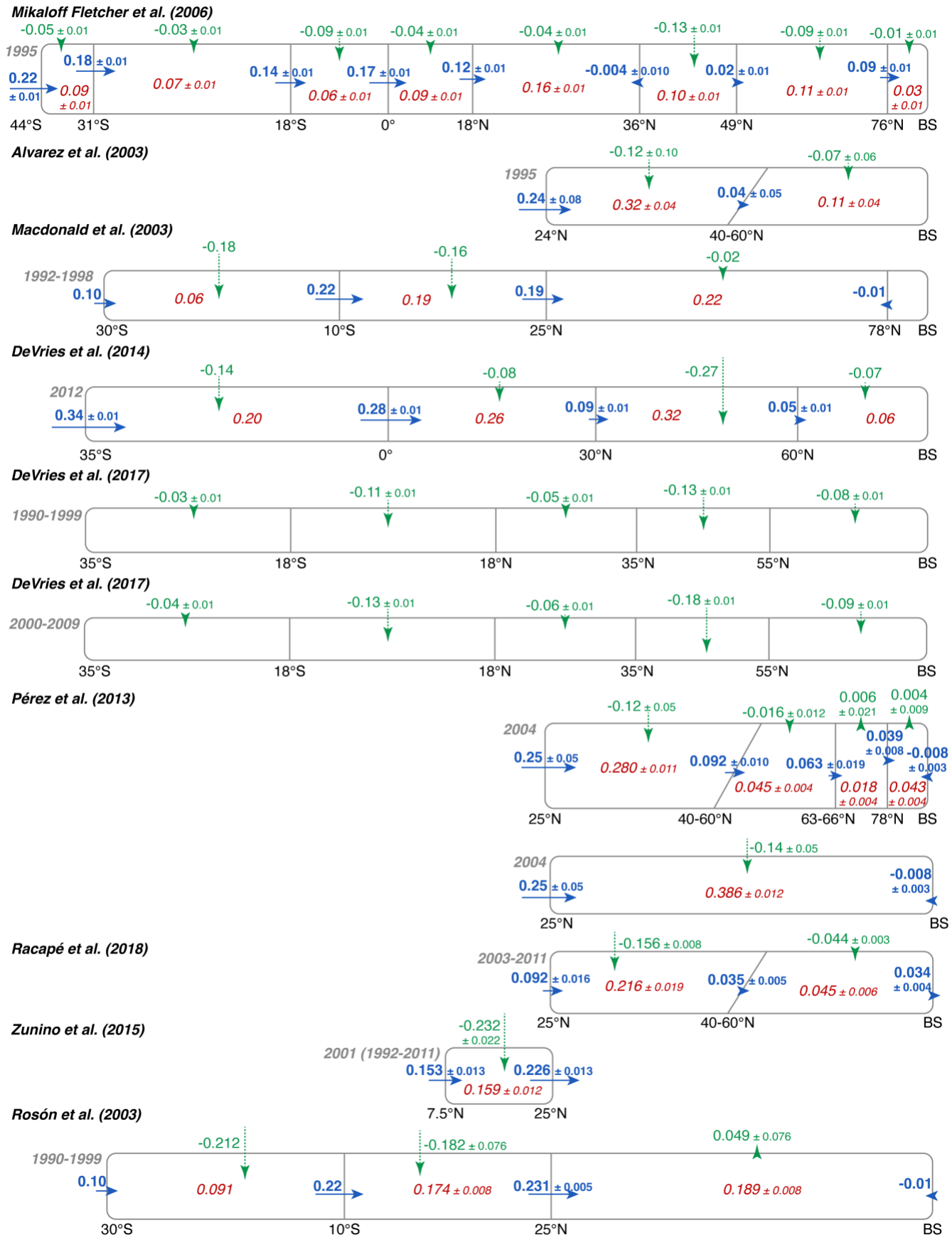


**Figure S5.** Horizontal transports (blue), storages (red) and vertical fluxes (green) of  $C_{anth}$  obtained from the literature, with reference to the years in grey at the top left of the box.

**Table S1.** Summary of the sections used in each model and the dataset from which they were recovered.

Latitude	Section	Year	Code	Dataset	NCEI DOI	References
45°S	A11	1992	74DI19921222	GLODAPv2	10.3334/cdiac/otg.woce_a11_74di19921222	
30°S	A10	1992-93	06MT19921227	GLODAPv2	10.3334/CDIAC/otg.ndp066	Johnson et al., (1998)
19°S	A09	1991	06MT19910210	GLODAPv2	10.3334/CDIAC/otg.ndp051	Johnson et al., (1995)
11°S	A08	1994	06MT19940329	GLODAPv2	10.3334/CDIAC/otg.ndp079	Johnson et al., (2002)
24°N	A05	1992	29HE19920714	GLODAPv2	10.3334/CDIAC/otg.ndp074	Millero et al., (2000)
24°N	Florida	1992	29HE19920714	GLODAPv2	10.3334/CDIAC/otg.ndp074	Millero et al., (2000)
47°N	A02	1993	06GA19930612	CCHDO		
55°N	AR07W	1990	18DA90012	CCHDO		
55°N	AR07E	1991	74AB62	CCHDO		
30°S	A10	2003	49NZ20031106	GLODAPv2	10.25921/gjsx-gy37	Uchida et al., (2005)
24°S	A095	2009	740H20090307	GLODAPv2	10.3334/cdiac/otg.clivar_a9.5_2009	Schuster et al., (2014)
24°N	A05	2004	74DI20040404	GLODAPv2	10.3334/cdiac/otg.carina_74di20040404	Cunningham, (2005)
24°N	Florida	2004	74DI20040404	GLODAPv2	10.3334/cdiac/otg.carina_74di20040404	Cunningham, (2005)
36°N	A03	2005	74AB20050501	GLODAPv2	10.3334/cdiac/otg.carina_74ab20050501	McDonagh, (2007)
55°N	AR07W	2005	18HU20050526	GLODAPv2	10.3334/cdiac/otg.woce_ar07w_2005	
55°N	AR07E	2007	64PE20070830	GLODAPv2	10.3334/cdiac/otg.clivar_ar07e_2007	
30°S	A10	2011	33RO20110926	GLODAPv2	10.3334/cdiac/otg.clivar_a10_2011	
24°S	A095	2018	740H20180228	GLODAPv2	10.25921/xy1r-rx06	
24°N	A05	2011	29AH20110128	GLODAPv2	10.3334/cdiac/otg.clivar_a05_29ah20110128	
24°N	Florida	2011	29AH20110128	GLODAPv2	10.3334/cdiac/otg.clivar_a05_29ah20110128	
47°N	A02	2013	06M220130509	GLODAPv2	10.25921/43nw-j564	
55°N	AR07W	2014	74JC20140606	BODC		
55°N	AR07E	2014	74JC20140606	BODC		

**Table S2.** Net values for each section of different parameters for different configurations of the inverse model for 1990-99 and the values before the adjustments of the inverse model (initial). The inverse solution applying only mass and salt conservation is noted as IM phys, and IM bgq represents the inverse solution with the added biogeochemical constraints. Positive values of MT (mass transport, in Sv), OHC (ocean heat content, in PW) and FW (freshwater flux, in Sv) indicate a northward transport, with negative values for a southward transport. For each variable, the 'TRedf' label indicates a sensitivity tests with a 20% variation of the values of the original Redfield ratio using a 100 repetition Montecarlo experiment. The values indicate the mean of the magnitude and the mean of the uncertainty, whereas the values within parenthesis indicate the standard deviation of the mean and uncertainty, multiplied by  $10^3$ . The 'near int' and 'prs int' labels indicate sensitivity tests to compare the results after using different interpolation methods: the former by using a nearest interpolation method instead of linear, and the latter by replacing the neutral density framework by pressure.

	<b>A11</b> <b>55°S</b>	<b>A10</b> <b>30°S</b>	<b>A09</b> <b>19°S</b>	<b>A08</b> <b>11°S</b>	<b>A05</b> <b>24°N</b>	<b>A02</b> <b>47°N</b>	<b>A07</b> <b>55°N</b>
<b>MT initial</b>	10.2	25.0	43.9	13.1	16.3	6.1	6.7
<b>MT IM phys</b>	-0.8 ± 3.5	-0.5 ± 2.7	-0.8 ± 2.7	-1.2 ± 2.5	-1.0 ± 2.6	-0.9 ± 2.8	-0.9 ± 3.5
<b>MT IM bgq</b>	-0.8 ± 2.7	-0.6 ± 2.3	-0.7 ± 2.2	-1.1 ± 2.1	-0.9 ± 2.1	-0.9 ± 2.4	-1.0 ± 2.6
<b>MT TRedf</b>	-0.8 ± 2.7 (1.54 ± 0.07)	-0.6 ± 2.3 (2.34 ± 0.03)	-0.7 ± 2.2 (0.63 ± 0.09)	-1.1 ± 2.1 (2.08 ± 0.26)	-0.9 ± 2.1 (2.54 ± 0.19)	-1.0 ± 2.4 (1.89 ± 0.34)	-1.0 ± 2.6 (0.02 ± 0.32)
<b>MT near int</b>	-0.8 ± 2.6	-0.5 ± 2.3	-0.8 ± 2.0	-1.1 ± 2.3	-1.0 ± 2.4	-0.9 ± 2.6	-1.0 ± 3.2
<b>MT prs int</b>	-0.6 ± 2.4	-0.5 ± 2.2	-0.7 ± 2.4	-1.2 ± 2.3	-0.9 ± 2.4	-0.9 ± 2.5	-0.9 ± 2.6
<b>OHC initial</b>	0.74	0.90	2.00	1.73	1.63	0.77	0.40
<b>OHC IM phys</b>	0.58 ± 0.08	0.36 ± 0.06	0.78 ± 0.07	0.93 ± 0.05	1.30 ± 0.08	0.48 ± 0.10	0.25 ± 0.09
<b>OHC IM bgq</b>	0.52 ± 0.07	0.35 ± 0.05	0.74 ± 0.05	0.94 ± 0.05	1.18 ± 0.07	0.41 ± 0.08	0.20 ± 0.07
<b>OHC TRedf</b>	0.53 ± 0.07 (0.411 ± 0.001)	0.35 ± 0.05 (0.144 ± 0.001)	0.74 ± 0.05 (0.187 ± 0.007)	0.94 ± 0.05 (0.441 ± 0.010)	1.18 ± 0.07 (0.671 ± 0.042)	0.42 ± 0.08 (0.397 ± 0.007)	0.21 ± 0.07 (0.295 ± 0.006)
<b>OHC near int</b>	0.52 ± 0.07	0.38 ± 0.05	0.71 ± 0.06	0.95 ± 0.05	1.20 ± 0.08	0.44 ± 0.09	0.21 ± 0.07
<b>OHC prs int</b>	0.42 ± 0.07	0.32 ± 0.05	0.74 ± 0.06	0.94 ± 0.05	1.16 ± 0.07	0.42 ± 0.08	0.21 ± 0.07
<b>FW initial</b>	-0.85	-1.36	-3.29	-1.64	-1.34	-0.73	-0.65
<b>FW IM phys</b>	-0.09 ± 0.08	0.28 ± 0.08	-0.12 ± 0.07	-0.34 ± 0.07	-0.34 ± 0.09	-0.14 ± 0.11	-0.05 ± 0.07
<b>FW IM bgq</b>	-0.03 ± 0.07	0.27 ± 0.07	-0.10 ± 0.06	-0.36 ± 0.07	-0.25 ± 0.07	-0.07 ± 0.09	-0.02 ± 0.07
<b>FW TRedf</b>	-0.03 ± 0.07 (0.289 ± 0.002)	0.27 ± 0.07 (0.120 ± 0.001)	-0.10 ± 0.06 (0.191 ± 0.004)	-0.36 ± 0.07 (0.032 ± 0.012)	-0.26 ± 0.07 (0.045 ± 0.050)	-0.08 ± 0.09 (0.213 ± 0.007)	-0.01 ± 0.07 (0.177 ± 0.001)
<b>FW near int</b>	-0.03 ± 0.07	0.27 ± 0.07	-0.06 ± 0.06	-0.35 ± 0.07	-0.27 ± 0.08	-0.10 ± 0.10	-0.01 ± 0.07
<b>FW prs int</b>	0.01 ± 0.07	0.28 ± 0.07	-0.08 ± 0.07	-0.35 ± 0.07	-0.25 ± 0.08	-0.08 ± 0.09	-0.01 ± 0.07

**Table S3.** Same as Table S2 but for the 2000-2009 period.

	<b>A10 30°S</b>	<b>A095 24°S</b>	<b>A05 24°N</b>	<b>A03 36°N</b>	<b>A07 55°N</b>
<b>MT initial</b>	18.0	39.3	19.1	31.3	-6.4
<b>MT IM phys</b>	-0.6 ± 3.1	-0.6 ± 3.1	-1.1 ± 2.8	-0.7 ± 2.8	-1.0 ± 3.0
<b>MT IM bgq</b>	-0.6 ± 2.7	-0.6 ± 2.5	-1.0 ± 2.3	-0.6 ± 2.4	-1.1 ± 2.5
<b>MT TRedf</b>	-0.6 ± 2.7 (1.07 ± 0.15)	-0.6 ± 2.5 (5.09 ± 0.36)	-1.0 ± 2.3 (2.68 ± 0.10)	-0.6 ± 2.4 (1.52 ± 0.05)	-1.1 ± 2.5 (0.21 ± 0.13)
<b>MT near int</b>	-0.6 ± 2.7	-0.7 ± 2.5	-1.0 ± 2.3	-0.6 ± 2.4	-1.0 ± 2.5
<b>MT prs int</b>	-0.6 ± 2.9	-0.6 ± 2.8	-1.1 ± 2.6	-0.6 ± 2.5	-1.0 ± 2.5
<b>OHC initial</b>	0.77	1.74	1.13	1.57	0.20
<b>OHC IM phys</b>	0.41 ± 0.06	0.70 ± 0.08	0.97 ± 0.09	0.59 ± 0.12	0.28 ± 0.07
<b>OHC IM bgq</b>	0.43 ± 0.05	0.67 ± 0.06	0.99 ± 0.08	0.53 ± 0.10	0.26 ± 0.06
<b>OHC TRedf</b>	0.43 ± 0.05 (0.338 ± 0.003)	0.67 ± 0.06 (1.956 ± 0.060)	0.98 ± 0.08 (0.367 ± 0.031)	0.53 ± 0.10 (0.315 ± 0.003)	0.26 ± 0.06 (0.219 ± 0.005)
<b>OHC near int</b>	0.42 ± 0.06	0.72 ± 0.07	0.93 ± 0.08	0.60 ± 0.11	0.21 ± 0.07
<b>OHC prs int</b>	0.43 ± 0.06	0.73 ± 0.06	0.97 ± 0.08	0.54 ± 0.10	0.25 ± 0.06
<b>FW initial</b>	-1.04	-2.76	-1.31	-2.29	0.33
<b>FW IM phys</b>	0.19 ± 0.07	-0.01 ± 0.11	-0.24 ± 0.07	-0.05 ± 0.07	-0.08 ± 0.16
<b>FW IM bgq</b>	0.19 ± 0.07	-0.01 ± 0.08	-0.25 ± 0.06	-0.02 ± 0.06	-0.05 ± 0.13
<b>FW TRedf</b>	0.19 ± 0.07 (0.277 ± 0.003)	-0.01 ± 0.08 (1.844 ± 0.088)	-0.25 ± 0.06 (0.062 ± 0.013)	-0.02 ± 0.06 (0.178 ± 0.002)	-0.05 ± 0.13 (0.167 ± 0.010)
<b>FW near int</b>	0.20 ± 0.07	-0.05 ± 0.09	-0.22 ± 0.06	-0.09 ± 0.07	-0.03 ± 0.13
<b>FW prs int</b>	0.19 ± 0.07	-0.05 ± 0.07	-0.23 ± 0.06	-0.04 ± 0.06	-0.05 ± 0.13

**Table S4.** Same as Table S2 but for the 2010-2019 period.

	<b>A10 30°S</b>	<b>A095 24°S</b>	<b>A05 24°N</b>	<b>A02 47°N</b>	<b>A07 55°N</b>
<b>MT initial</b>	25.22	30.5	25.8	2.9	2.4
<b>MT IM phys</b>	-0.7 ± 3.3	-0.8 ± 3.1	-1.0 ± 2.9	-0.9 ± 2.6	-0.9 ± 2.6
<b>MT IM bgq</b>	-0.7 ± 2.7	-1.1 ± 2.5	-0.9 ± 2.3	-0.9 ± 2.2	-1.0 ± 2.1
<b>MT TRedf</b>	-0.7 ± 2.7 (1.25 ± 0.13)	-1.1 ± 2.5 (11.18 ± 0.29)	-0.9 ± 2.3 (4.72 ± 0.10)	-0.9 ± 2.2 (1.73 ± 0.35)	-1.0 ± 2.1 (0.06 ± 0.26)
<b>MT near int</b>	-0.7 ± 3.1	-1.1 ± 2.9	-1.0 ± 2.7	-1.0 ± 2.4	-0.9 ± 2.2
<b>MT prs int</b>	-0.8 ± 3.1	-1.2 ± 2.8	-1.0 ± 2.6	-0.9 ± 2.3	-0.9 ± 2.1
<b>OHC initial</b>	0.99	1.36	1.34	0.69	0.33
<b>OHC IM phys</b>	0.52 ± 0.07	0.66 ± 0.07	1.13 ± 0.07	0.40 ± 0.08	0.29 ± 0.06
<b>OHC IM bgq</b>	0.63 ± 0.07	0.64 ± 0.06	1.15 ± 0.06	0.33 ± 0.07	0.27 ± 0.05
<b>OHC TRedf</b>	0.63 ± 0.07 (0.846 ± 0.001)	0.64 ± 0.06 (1.639 ± 0.068)	1.15 ± 0.06 (0.427 ± 0.030)	0.33 ± 0.07 (0.281 ± 0.009)	0.27 ± 0.05 (0.154 ± 0.006)
<b>OHC near int</b>	0.67 ± 0.07	0.66 ± 0.06	1.16 ± 0.06	0.34 ± 0.07	0.26 ± 0.06
<b>OHC prs int</b>	0.62 ± 0.07	0.66 ± 0.06	1.17 ± 0.06	0.33 ± 0.07	0.26 ± 0.05
<b>FW initial</b>	-1.58	-2.11	-1.72	-0.44	-0.35
<b>FW IM phys</b>	0.07 ± 0.06	0.01 ± 0.09	-0.34 ± 0.03	-0.05 ± 0.13	-0.11 ± 0.13
<b>FW IM bgq</b>	0.01 ± 0.06	0.05 ± 0.07	-0.37 ± 0.03	-0.01 ± 0.11	-0.08 ± 0.12
<b>FW TRedf</b>	0.01 ± 0.06 (0.605 ± 0.001)	0.05 ± 0.07 (1.552 ± 0.108)	-0.37 ± 0.03 (0.277 ± 0.029)	-0.01 ± 0.11 (0.117 ± 0.016)	-0.08 ± 0.12 (0.059 ± 0.005)
<b>FW near int</b>	-0.02 ± 0.06	0.02 ± 0.08	-0.38 ± 0.03	-0.01 ± 0.12	-0.08 ± 0.12
<b>FW prs int</b>	0.01 ± 0.06	0.03 ± 0.08	-0.38 ± 0.03	-0.01 ± 0.11	-0.08 ± 0.12

**Table S5.** Net values within each box of different parameters and properties for different configurations of the inverse model for 1990-99 and the values before the adjustments of the inverse model (initial). The inverse solution applying only mass and salt conservation is noted as IM phys, and IM bgq represents the inverse solution with the added biogeochemical constraints. Positive values of air-sea O<sub>2</sub> fluxes (FO<sub>2</sub>; in kmol s<sup>-1</sup>) indicate an oceanic gain of O<sub>2</sub> within the box, with negative values expressing a loss of O<sub>2</sub> to the atmosphere within the box of contiguous sections. The consumption rate of O<sub>2</sub> in the whole water column for each box (BO<sub>2</sub>; in kmol s<sup>-1</sup>) is positive for oxygen production and negative for oxygen consumption. The net transport of oxygen (kmol s<sup>-1</sup>), nitrate (kmol s<sup>-1</sup>), silicate (kmol s<sup>-1</sup>), phosphate (kmol s<sup>-1</sup>) and total carbon (PgC yr<sup>-1</sup>) is computed as the balance among the transports at the boundaries of the box, integrated vertically. For each variable, the TRedf label indicates a sensitivity test with a 20% variation of the values of the original Redfield ratio using a 100 repetition Montecarlo experiment (Supporting Information Text S3). The values indicate the mean of the magnitude and the mean of the uncertainty, whereas the values within parenthesis indicate the standard deviation of the mean and uncertainty, multiplied by 10<sup>3</sup>. The 'near int' and 'prs int' labels indicate sensitivity tests to compare the results after using different interpolation methods: the former by using a nearest interpolation method instead of linear, and the latter by replacing the neutral density framework by pressure.

	<b>A11-A10</b> <b>55 - 30°S</b>	<b>A10-A09</b> <b>30 - 19°S</b>	<b>A09-A08</b> <b>19 - 11°S</b>	<b>A08-A05</b> <b>11°S - 24°N</b>	<b>A05-A02</b> <b>24 - 47°N</b>	<b>A02-A07</b> <b>47 - 55°N</b>
<b>FO<sub>2</sub> air-sea</b>	259 ± 74	130 ± 39	150 ± 33	479 ± 146	-393 ± 71	-226 ± 105
<b>FO<sub>2</sub> TRedf</b>	284 ± 75 (22.45 ± 0.01)	153 ± 40 (4.40 ± 0.01)	135 ± 33 (6.24 ± 0.01)	558 ± 166 (227.22 ± 0.58)	-330 ± 73 (55.13 ± 0.02)	-430 ± 119 (4.68 ± 0.01)
<b>FO<sub>2</sub> near int</b>	279 ± 75	150 ± 40	133 ± 33	547 ± 166	-327 ± 73	-432 ± 119
<b>FO<sub>2</sub> prs int</b>	284 ± 75	153 ± 40	135 ± 33	531 ± 166	-335 ± 73	-437 ± 119
<b>BO<sub>2</sub></b>	291 ± 117	234 ± 92	170 ± 68	486 ± 265	596 ± 173	89 ± 51
<b>BO<sub>2</sub> TRedf</b>	303 ± 118 (757 ± 206)	233 ± 92 (71 ± 63)	166 ± 68 (148 ± 29)	695 ± 282 (8571 ± 1993)	466 ± 176 (4396 ± 594)	97 ± 51 (353 ± 45)
<b>BO<sub>2</sub> near int</b>	315 ± 119	226 ± 92	162 ± 68	699 ± 284	467 ± 177	96 ± 51
<b>BO<sub>2</sub> prs int</b>	309 ± 118	228 ± 92	167 ± 68	614 ± 282	461 ± 176	96 ± 51
<b>O<sub>2</sub> initial</b>	-4407	2330	6233	-461	418	796
<b>O<sub>2</sub> IM phys</b>	-1040 ± 1077	-1668 ± 920	100 ± 979	-821 ± 1028	-1822 ± 1072	271 ± 1263
<b>O<sub>2</sub> IM bgq</b>	-967 ± 874	-1608 ± 758	-126 ± 779	-1125 ± 794	-1923 ± 839	174 ± 981
<b>O<sub>2</sub> TRedf</b>	-967 ± 873 (323 ± 24)	-1608 ± 758 (4381 ± 13)	-125 ± 779 (1455 ± 56)	-1125 ± 794 (6071 ± 61)	-1923 ± 839 (6601 ± 87)	174 ± 981 (97 ± 146)
<b>O<sub>2</sub> near int</b>	-1112 ± 973	585 ± 958	730 ± 996	-1308 ± 1106	-1105 ± 1093	232 ± 1126
<b>O<sub>2</sub> prs int</b>	-1396 ± 817	-455 ± 719	-260 ± 718	-766 ± 721	-801 ± 793	-754 ± 997
<b>NO<sub>3</sub> initial</b>	-378	390	976	374	193	15
<b>NO<sub>3</sub> IM phys</b>	-64 ± 118	64 ± 102	257 ± 101	301 ± 123	2 ± 112	-4 ± 69
<b>NO<sub>3</sub> IM bgq</b>	-9 ± 94	77 ± 84	234 ± 80	294 ± 97	19 ± 89	-16 ± 55

<b>NO<sub>3</sub> TRedf</b>	-9 ± 94 (661 ± 3)	77 ± 84 (796 ± 5)	234 ± 80 (2403 ± 14)	294 ± 97 (5031 ± 48)	19 ± 89 (3232 ± 40)	-16 ± 55 (118 ± 7)
<b>NO<sub>3</sub> near int</b>	117 ± 113	239 ± 105	91 ± 113	258 ± 142	192 ± 113	-39 ± 82
<b>NO<sub>3</sub> prs int</b>	-85 ± 102	32 ± 200	105 ± 146	61 ± 92	-53 ± 101	-43 ± 90
<b>SiO<sub>4</sub> initial</b>	-839	412	992	-36	77	24
<b>SiO<sub>4</sub> IM phys</b>	-219 ± 344	-145 ± 282	63 ± 243	247 ± 213	-49 ± 160	43 ± 78
<b>SiO<sub>4</sub> IM bgq</b>	-41 ± 245	-72 ± 203	59 ± 181	246 ± 155	-57 ± 116	43 ± 65
<b>SiO<sub>4</sub> TRedf</b>	-41 ± 244 (2330 ± 20)	-72 ± 203 (2532 ± 17)	59 ± 181 (3035 ± 23)	246 ± 154 (6125 ± 53)	-57 ± 116 (4232 ± 49)	43 ± 65 (16 ± 2)
<b>SiO<sub>4</sub> near int</b>	-90 ± 234	147 ± 197	-82 ± 195	131 ± 192	49 ± 138	29 ± 72
<b>SiO<sub>4</sub> prs int</b>	-48 ± 261	-14 ± 182	29 ± 156	44 ± 154	15 ± 99	-15 ± 83
<b>PO<sub>4</sub> initial</b>	-18.8	28.7	52.6	5.1	9.7	0.4
<b>PO<sub>4</sub> IM phys</b>	-1.5 ± 10.9	2.4 ± 7.8	5.9 ± 6.8	1.8 ± 6.6	-5.3 ± 5.6	-1.0 ± 4.6
<b>PO<sub>4</sub> IM bgq</b>	3.1 ± 9.1	4.2 ± 6.6	4.5 ± 5.4	3.5 ± 5.4	-2.5 ± 4.6	-1.7 ± 3.6
<b>PO<sub>4</sub> TRedf</b>	3.1 ± 9.1 (53.2 ± 0.2)	4.2 ± 6.6 (54.0 ± 0.3)	4.5 ± 5.4 (141.7 ± 0.8)	3.5 ± 5.4 (239.1 ± 1.0)	-2.5 ± 4.6 (135.8 ± 0.3)	-1.7 ± 3.6 (8.0 ± 0.5)
<b>PO<sub>4</sub> near int</b>	6.4 ± 10.3	9.5 ± 8.2	7.5 ± 9.2	14.5 ± 11.4	9.8 ± 8.3	-3.0 ± 5.4
<b>PO<sub>4</sub> prs int</b>	2.6 ± 9.0	4.1 ± 7.4	0.4 ± 7.1	-3.9 ± 9.1	-2.8 ± 7.1	-3.6 ± 5.2
<b>CT initial</b>	-11.30	16.85	23.25	0.46	7.56	-0.67
<b>CT IM phys</b>	1.16 ± 1.29	1.80 ± 0.71	-1.78 ± 0.80	-1.98 ± 0.74	-0.80 ± 0.76	-0.97 ± 0.67
<b>CT IM bgq</b>	1.25 ± 1.26	1.72 ± 0.70	-1.82 ± 0.80	-2.25 ± 0.73	-0.83 ± 0.76	-0.92 ± 0.67
<b>CT TRedf</b>	1.25 ± 1.26 (6.41 ± 0.02)	1.72 ± 0.70 (6.62 ± 0.03)	-1.82 ± 0.80 (6.06 ± 0.05)	-2.25 ± 0.73 (19.27 ± 0.04)	-0.83 ± 0.76 (17.02 ± 0.05)	-0.92 ± 0.67 (1.08 ± 0.09)
<b>CT near int</b>	9.24 ± 1.21	4.44 ± 0.61	-13.41 ± 0.63	-1.44 ± 0.46	7.98 ± 0.59	-1.40 ± 0.50
<b>CT prs int</b>	0.29 ± 1.25	0.80 ± 0.68	1.04 ± 0.76	0.24 ± 0.70	-0.08 ± 0.74	0.13 ± 0.66



**Table S6.** Same as Table S5 but for the 2000-2009 period.

	<b>A10-A095</b> <b>30 - 24°S</b>	<b>A095-A05</b> <b>24°S - 24°N</b>	<b>A05-A03</b> <b>24 - 36°N</b>	<b>A03-A07</b> <b>36 - 55°N</b>
<b>FO<sub>2</sub> air-sea</b>	118 ± 29	671 ± 223	-131 ± 33	-379 ± 239
<b>FO<sub>2</sub> TRedf</b>	117 ± 29 (12.80 ± 0.01)	670 ± 223 (768.25 ± 10.02)	-130 ± 33 (10.22 ± 0.01)	-379 ± 239 (13.41 ± 0.02)
<b>FO<sub>2</sub> near int</b>	116 ± 29	576 ± 223	-133 ± 33	-397 ± 239
<b>FO<sub>2</sub> prs int</b>	118 ± 29	562 ± 223	-134 ± 33	-374 ± 239
<b>BO<sub>2</sub></b>	134 ± 53	958 ± 380	275 ± 108	252 ± 117
<b>BO<sub>2</sub> TRedf</b>	134 ± 53 (89 ± 12)	956 ± 379 (3408 ± 4599)	275 ± 108 (1342 ± 124)	251 ± 117 (2876 ± 344)
<b>BO<sub>2</sub> near int</b>	134 ± 53	909 ± 381	266 ± 108	262 ± 118
<b>BO<sub>2</sub> prs int</b>	134 ± 53	720 ± 378	273 ± 108	246 ± 117
<b>O<sub>2</sub> initial</b>	-4257	-6352	-4032	-7202
<b>O<sub>2</sub> IM phys</b>	167 ± 1086	-2644 ± 1070	-1661 ± 1017	1531 ± 1119
<b>O<sub>2</sub> IM bgq</b>	-2 ± 887	-2783 ± 851	-1833 ± 821	791 ± 904
<b>O<sub>2</sub> TRedf</b>	-4 ± 887 (5529 ± 46)	-2832 ± 851 (15890 ± 43)	-1878 ± 821 (8389 ± 23)	793 ± 904 (798 ± 65)
<b>O<sub>2</sub> near int</b>	-257 ± 1128	-2051 ± 948	412 ± 948	-133 ± 1078
<b>O<sub>2</sub> prs int</b>	662 ± 919	-568 ± 852	-547 ± 872	-823 ± 942
<b>NO<sub>3</sub> initial</b>	-414	-339	-117	-524
<b>NO<sub>3</sub> IM phys</b>	12 ± 116	112 ± 131	-20 ± 115	69 ± 78
<b>NO<sub>3</sub> IM bgq</b>	-3 ± 95	99 ± 100	-27 ± 87	20 ± 67
<b>NO<sub>3</sub> TRedf</b>	-3 ± 95 (2322 ± 25)	98 ± 99 (5209 ± 46)	-27 ± 87 (2792 ± 30)	19 ± 67 (417 ± 1)
<b>NO<sub>3</sub> near int</b>	-46 ± 143	-254 ± 113	-261 ± 99	64 ± 100
<b>NO<sub>3</sub> prs int</b>	-72 ± 80	-67 ± 79	4 ± 97	-10 ± 73
<b>SiO<sub>4</sub> initial</b>	-468	-631	195	-299
<b>SiO<sub>4</sub> IM phys</b>	103 ± 285	121 ± 246	-114 ± 170	7 ± 90
<b>SiO<sub>4</sub> IM bgq</b>	59 ± 218	142 ± 182	-111 ± 128	-23 ± 72
<b>SiO<sub>4</sub> TRedf</b>	58 ± 218 (4353 ± 85)	142 ± 182 (9102 ± 97)	-111 ± 128 (3698 ± 30)	-22 ± 72 (297 ± 3)
<b>SiO<sub>4</sub> near int</b>	-81 ± 253	3 ± 196	-190 ± 139	16 ± 105
<b>SiO<sub>4</sub> prs int</b>	21 ± 194	19 ± 207	28 ± 164	-3 ± 158
<b>PO<sub>4</sub> initial</b>	-24.1	-20.4	-5.7	-30.9

<b>PO<sub>4</sub> IM phys</b>	2.0 ± 10.5	8.3 ± 12.0	-2.5 ± 10.2	2.7 ± 6.7
<b>PO<sub>4</sub> IM bgq</b>	0.8 ± 8.8	6.5 ± 9.6	-4.4 ± 8.4	0.6 ± 6.0
<b>PO<sub>4</sub> TRedf</b>	0.8 ± 8.8	6.5 ± 9.6	-4.2 ± 8.4	0.6 ± 6.0
	(164.9 ± 1.4)	(389.3 ± 2.6)	(223.0 ± 1.9)	(37.0 ± 0.3)
<b>PO<sub>4</sub> near int</b>	6.3 ± 11.3	-5.8 ± 9.0	-34.2 ± 7.8	-11.9 ± 8.2
<b>PO<sub>4</sub> prs int</b>	2.7 ± 10.5	3.4 ± 10.3	-2.4 ± 9.7	-5.1 ± 11.9
<b>CT initial</b>	-17.83	-17.37	-10.58	-24.92
<b>CT IM phys</b>	-0.81 ± 0.81	-1.43 ± 0.71	-1.21 ± 11.6	5.45 ± 1.10
<b>CT IM bgq</b>	-0.87 ± 0.80	-0.87 ± 0.70	-0.91 ± 1.16	4.19 ± 1.10
<b>CT TRedf</b>	-0.87 ± 0.80	-0.88 ± 0.70	-0.91 ± 1.16	4.19 ± 1.11
	(4.88 ± 0.50)	(20.99 ± 0.66)	(13.93 ± 0.08)	(0.62 ± 0.04)
<b>CT near int</b>	19.3 ± 0.24	-2.41 ± 0.53	13.39 ± 0.79	14.14 ± 0.63
<b>CT prs int</b>	-0.42 ± 0.76	-0.98 ± 0.88	-1.03 ± 1.15	-0.41 ± 1.09

**Table S7.** Same as Table S5 but for the 2010-2019 period.

	<b>A10-A095</b> <b>30 - 24°S</b>	<b>A095-A05</b> <b>24°S - 24°N</b>	<b>A05-A02</b> <b>24 - 47°N</b>	<b>A02-A07</b> <b>47 - 55°N</b>
<b>FO<sub>2</sub> air-sea</b>	153 ± 36	-32 ± 205	-519 ± 70	-345 ± 133
<b>FO<sub>2</sub> TRedf</b>	149 ± 36 (4.51 ± 0.01)	347 ± 265 (753.38 ± 21.61)	-340 ± 74 (18.40 ± 0.01)	-511 ± 166 (0.38 ± 0.01)
<b>FO<sub>2</sub> near int</b>	151 ± 36	724 ± 265	-332 ± 74	-612 ± 166
<b>FO<sub>2</sub> prs int</b>	149 ± 36	582 ± 265	-347 ± 74	-612 ± 166
<b>BO<sub>2</sub></b>	138 ± 53	801 ± 342	655 ± 178	59 ± 37
<b>BO<sub>2</sub> TRedf</b>	135 ± 53 (79 ± 12)	987 ± 380 (8705 ± 4528)	475 ± 181 (7723 ± 682)	67 ± 37 (91 ± 17)
<b>BO<sub>2</sub> near int</b>	134 ± 53	900 ± 384	482 ± 182	68 ± 37
<b>BO<sub>2</sub> near int</b>	135 ± 53	794 ± 379	488 ± 181	67 ± 37
<b>O<sub>2</sub> initial</b>	-518	-1946	5365	1604
<b>O<sub>2</sub> IM phys</b>	611 ± 1089	-1906 ± 1048	-636 ± 1024	1469 ± 1038
<b>O<sub>2</sub> IM bgq</b>	768 ± 881	-1914 ± 820	-1221 ± 815	1069 ± 851
<b>O<sub>2</sub> TRedf</b>	770 ± 881 (11994 ± 48)	-1909 ± 820 (22627 ± 57)	-1219 ± 815 (7503 ± 105)	1069 ± 851 (1368 ± 134)
<b>O<sub>2</sub> near int</b>	-466 ± 1069	-2139 ± 994	-2175 ± 945	-332 ± 1000
<b>O<sub>2</sub> prs int</b>	675 ± 978	-436 ± 859	-384 ± 839	-333 ± 905
<b>NO<sub>3</sub> initial</b>	-60	-35	493	29
<b>NO<sub>3</sub> IM phys</b>	39 ± 125	90 ± 114	-29 ± 89	14 ± 59
<b>NO<sub>3</sub> IM bgq</b>	-19 ± 102	105 ± 91	-5 ± 73	17 ± 49
<b>NO<sub>3</sub> TRedf</b>	-19 ± 102 (2421 ± 24)	104 ± 91 (4769 ± 40)	-5 ± 73 (1930 ± 18)	17 ± 49 (62 ± 6)
<b>NO<sub>3</sub> near int</b>	-134 ± 166	40 ± 150	106 ± 112	-50 ± 62
<b>NO<sub>3</sub> prs int</b>	27 ± 131	128 ± 147	102 ± 138	-48 ± 59
<b>SiO<sub>4</sub> initial</b>	-24	-330	538	-37
<b>SiO<sub>4</sub> IM phys</b>	139 ± 291	-35 ± 248	-331 ± 166	-98 ± 85
<b>SiO<sub>4</sub> IM bgq</b>	10 ± 193	84 ± 156	-342 ± 109	-76 ± 63
<b>SiO<sub>4</sub> TRedf</b>	30 ± 219 (4582 ± 57)	83 ± 178 (8949 ± 83)	-215 ± 122 (3410 ± 35)	-42 ± 68 (35 ± 2)
<b>SiO<sub>4</sub> near int</b>	-53 ± 268	32 ± 210	-36 ± 132	-39 ± 71
<b>SiO<sub>4</sub> prs int</b>	41 ± 156	53 ± 180	47 ± 159	-16 ± 84
<b>PO<sub>4</sub> initial</b>	-2.9	-3.0	31.8	1.1

<b>PO<sub>4</sub> IM phys</b>	-2.1 ± 10.6	0.0 ± 10.6	-5.6 ± 6.5	-0.5 ± 3.9
<b>PO<sub>4</sub> IM bgq</b>	-3.0 ± 8.4	2.9 ± 8.6	-5.0 ± 5.5	-0.4 ± 3.2
<b>PO<sub>4</sub> TRedf</b>	-3.1 ± 8.4 (226.7 ± 2.7)	2.8 ± 8.6 (348.4 ± 3.1)	-5.0 ± 5.5 (94.5 ± 0.7)	-0.5 ± 3.2 (4.5 ± 0.4)
<b>PO<sub>4</sub> near int</b>	-5.5 ± 11.0	5.7 ± 11.3	3.3 ± 8.5	-4.8 ± 4.1
<b>PO<sub>4</sub> prs int</b>	2.1 ± 12.4	8.3 ± 13.2	7.5 ± 9.6	-3.5 ± 7.9
<b>CT initial</b>	-3.95	-4.52	18.25	-2.13
<b>CT IM phys</b>	1.06 ± 0.77	-0.63 ± 0.62	-0.77 ± 0.64	-1.70 ± 0.53
<b>CT IM bgq</b>	1.22 ± 0.77	0.02 ± 0.62	-0.47 ± 0.63	-1.77 ± 0.52
<b>CT TRedf</b>	1.22 ± 0.77 (14.73 ± 0.04)	0.01 ± 0.62 (23.47 ± 0.10)	-0.47 ± 0.63 (8.40 ± 0.08)	-1.77 ± 0.52 (1.56 ± 0.03)
<b>CT near int</b>	8.13 ± 0.55	19.03 ± 0.39	15.52 ± 0.40	-1.40 ± 0.43
<b>CT prs int</b>	0.55 ± 0.74	0.08 ± 0.60	-0.03 ± 0.63	-0.14 ± 0.52

**Table S8.** Values of net transport of standard  $C_{\text{anth}}$  (in  $\text{PgC yr}^{-1}$ ) for each section for the 1990-99 decade per layer (upper, deep and abyssal) comparing the values obtained by the model described in the manuscript and the sensitivity test performed using a Montecarlo variation of 20% of the mean  $C_{\text{anth}}$  concentration at surface (Supporting Information Text S3). The values indicate the mean of the magnitude and the mean of the uncertainty, whereas the values within parenthesis indicate the standard deviation of the mean and uncertainty, multiplied by  $10^3$ .

	<b>A11 55°S</b>	<b>A10 30°S</b>	<b>A09 19°S</b>	<b>A08 11°S</b>	<b>A05 24°N</b>	<b>A02 47°N</b>	<b>A07 55°N</b>
<b><math>C_{\text{anth}}</math> upper</b>	0.209 ± 0.021	0.208 ± 0.015	0.234 ± 0.013	0.253 ± 0.011	0.206 ± 0.015	0.160 ± 0.025	0.153 ± 0.029
<b><math>C_{\text{anth}}</math> upper mod</b>	0.209 ± 0.021 (0.8 ± 1.3)	0.207 ± 0.015 (8.2 ± 1.7)	0.231 ± 0.013 (29.6 ± 1.2)	0.249 ± 0.011 (33.0 ± 0.9)	0.206 ± 0.015 (3.7 ± 1.4)	0.160 ± 0.026 (3.8 ± 0.1)	0.153 ± 0.029 (0.8 ± 0.1)
<b><math>C_{\text{anth}}</math> deep</b>	-0.055 ± 0.009	-0.041 ± 0.011	-0.075 ± 0.017	-0.076 ± 0.013	-0.077 ± 0.021	-0.082 ± 0.014	-0.066 ± 0.025
<b><math>C_{\text{anth}}</math> deep mod</b>	-0.055 ± 0.009 (0 ± 0)	-0.041 ± 0.011 (0 ± 0)	-0.075 ± 0.017 (0 ± 0)	-0.076 ± 0.013 (0 ± 0)	-0.077 ± 0.021 (0 ± 0)	-0.082 ± 0.014 (0 ± 0)	-0.066 ± 0.025 (0 ± 0)
<b><math>C_{\text{anth}}</math> abyss</b>	0.016 ± 0.006	0.008 ± 0.005	0.012 ± 0.004	0.006 ± 0.004	0.001 ± 0.004	0 ± 0	0 ± 0
<b><math>C_{\text{anth}}</math> abyss mod</b>	0.016 ± 0.006 (0 ± 0)	0.008 ± 0.005 (0 ± 0)	0.012 ± 0.004 (0 ± 0)	0.006 ± 0.004 (0 ± 0)	0.001 ± 0.004 (0 ± 0)	0 ± 0 (0 ± 0)	0 ± 0 (0 ± 0)

**Table S9.** Same as Table S9 but for the 2000-2009 period.

	<b>A10 30°S</b>	<b>A095 24°S</b>	<b>A05 24°N</b>	<b>A03 36°N</b>	<b>A07 55°N</b>
<b>C<sub>anth</sub> upper</b>	0.252 ± 0.016	0.336 ± 0.020	0.216 ± 0.019	0.119 ± 0.029	0.204 ± 0.031
<b>C<sub>anth</sub> upper TRedf</b>	0.252 ± 0.016 (3.8 ± 1.8)	0.337 ± 0.020 (35.1 ± 2.7)	0.190 ± 0.020 (9.9 ± 2.4)	0.120 ± 0.029 (12.5 ± 1.8)	0.204 ± 0.031 (0.2 ± 0.1)
<b>C<sub>anth</sub> deep</b>	-0.063 ± 0.010	-0.093 ± 0.018	-0.089 ± 0.025	-0.062 ± 0.022	-0.116 ± 0.022
<b>C<sub>anth</sub> deep TRedf</b>	-0.063 ± 0.010 (0 ± 0)	-0.094 ± 0.018 (0 ± 0)	-0.095 ± 0.025 (0 ± 0)	-0.062 ± 0.022 (0 ± 0)	-0.116 ± 0.022 (0 ± 0)
<b>C<sub>anth</sub> abyss</b>	0.008 ± 0.004	-0.002 ± 0.007	0.001 ± 0.004	0 ± 0	0 ± 0
<b>C<sub>anth</sub> abyss TRedf</b>	0.008 ± 0.004 (0 ± 0)	-0.002 ± 0.007 (0 ± 0)	0.002 ± 0.004 (0 ± 0)	0 ± 0 (0 ± 0)	0 ± 0 (0 ± 0)

**Table S10.** Same as Table S9 but for the 2010-2019 period.

	<b>A10 30°S</b>	<b>A095 24°S</b>	<b>A05 24°N</b>	<b>A02 47°N</b>	<b>A07 55°N</b>
<b>C<sub>anth</sub> upper</b>	0.404 ± 0.023	0.400 ± 0.019	0.337 ± 0.016	0.258 ± 0.030	0.263 ± 0.031
<b>C<sub>anth</sub> upper TRedf</b>	0.404 ± 0.023 (1.3 ± 2.6)	0.399 ± 0.019 (20.4 ± 2.3)	0.334 ± 0.016 (8.7 ± 0.9)	0.258 ± 0.030 (0 ± 0)	0.263 ± 0.031 (0 ± 0)
<b>C<sub>anth</sub> deep</b>	-0.081 ± 0.011	-0.084 ± 0.012	-0.118 ± 0.017	-0.154 ± 0.018	-0.148 ± 0.028
<b>C<sub>anth</sub> deep TRedf</b>	-0.081 ± 0.011 (0 ± 0)	-0.084 ± 0.012 (0 ± 0)	-0.114 ± 0.017 (0 ± 0)	-0.154 ± 0.018 (0 ± 0)	-0.148 ± 0.028 (0 ± 0)
<b>C<sub>anth</sub> abyss</b>	0.011 ± 0.005	0.004 ± 0.005	0.003 ± 0.003	0 ± 0	0 ± 0
<b>C<sub>anth</sub> abyss TRedf</b>	0.011 ± 0.005 (0 ± 0)	0.004 ± 0.005 (0 ± 0)	0.003 ± 0.003 (0 ± 0)	0 ± 0 (0 ± 0)	0 ± 0 (0 ± 0)

**Table S11.** Literature values of  $C_{\text{anth}}$  uptake from the atmosphere in the North Atlantic, referenced to the year from the study and normalized to 2005 assuming TSS.

	Latitudes	Reference year	Uptake (Pgc yr <sup>-1</sup> )	Uptake (norm 2005; Pgc yr <sup>-1</sup> )
<b>OGCM</b>				
Mikaloff Fletcher et al., (2006)	44 - 31°S	1995	-0.05 ± 0.01	-0.06 ± 0.01
	31 - 18°S	1995	-0.03 ± 0.01	-0.04 ± 0.01
	18°S - 0°	1995	-0.09 ± 0.01	-0.11 ± 0.01
	0° - 18°N	1995	-0.04 ± 0.01	-0.05 ± 0.01
	18 - 36°N	1995	-0.04 ± 0.01	-0.05 ± 0.01
	36 - 49°N	1995	-0.13 ± 0.01	-0.16 ± 0.01
	49 - 76°N	1995	-0.09 ± 0.01	-0.11 ± 0.01
	76°N - BS	1995	-0.01 ± 0.01	-0.01 ± 0.01
Racapé et al., 2018)	25 - 40/60°N	2003-2011	-0.156 ± 0.008	-0.150 ± 0.008
	40/60°N - BS	2003-2011	-0.044 ± 0.003	-0.042 ± 0.003
<b>OCIM</b>				
DeVries, (2014)	35°S - 0°	2012	-0.14	-0.12
	0° - 30°N	2012	-0.08	-0.07
	30 - 60°N	2012	-0.27	-0.24
	60°N - BS	2012	-0.07	-0.06
DeVries et al., (2017)	35 - 18°S	1990-1999	-0.03 ± 0.01	-0.04 ± 0.01
	18°S - 18°N	1990-1999	-0.11 ± 0.01	-0.13 ± 0.01
	18 - 35°N	1990-1999	-0.05 ± 0.01	-0.06 ± 0.01
	35 - 55°N	1990-1999	-0.13 ± 0.01	-0.16 ± 0.01
	55°N - BS	1990-1999	-0.08 ± 0.01	-0.10 ± 0.01
	35 - 18°S	2000-2009	-0.04 ± 0.01	-0.04 ± 0.01
	18°S - 18°N	2000-2009	-0.13 ± 0.01	-0.13 ± 0.01
	18 - 35°N	2000-2009	-0.06 ± 0.01	-0.06 ± 0.01
	35 - 55°N	2000-2009	-0.18 ± 0.01	-0.18 ± 0.01
	55°N - BS	2000-2009	-0.09 ± 0.01	-0.09 ± 0.01
<b>Hydrographic estimations</b>				
Álvarez et al., (2003)	24 - 40/60°N	1995	-0.12 ± 0.10	-0.14 ± 0.12



	40/60°N - BS	1995	-0.07 ± 0.06	-0.08 ± 0.07
Macdonald et al., (2003)	30 - 10°S	1992-1998	-0.18	-0.22
	10°S - 25°N	1992-1998	-0.16	-0.19
	25 - 78°N	1992-1998	-0.02	-0.02
Pérez et al., (2013)	25 - 40/60°N	2004	-0.12 ± 0.05	-0.12 ± 0.05
	40/60 - 63/66°N	2004	-0.016 ± 0.012	-0.016 ± 0.012
	63/66 - 78°N	2004	0.006 ± 0.021	0.006 ± 0.021
	78°N - BS	2004	0.004 ± 0.009	0.004 ± 0.009
	25°N - BS	2004	-0.14 ± 0.05	-0.14 ± 0.05
Rosón, (2003)	30 - 10°S	1990-1999	-0.212	-0.258
	10°S - 25°N	1990-1999	-0.182	-0.222
	25°N - BS	1990-1999	0.049	0.060
Zunino et al., (2015)	7.5 - 25°N	1992 - 2011	-0.232 ± 0.022	-0.248 ± 0.023

## References to Supporting Information

- Álvarez, M., Ríos, A. F., Pérez, F. F., Bryden, H. L., & Rosón, G. (2003). Transports and budgets of total inorganic carbon in the subpolar and temperate North Atlantic. *Global Biogeochemical Cycles*, 17(1), 1–21. <https://doi.org/10.1029/2002GB001881>
- Anderson, L. A. (1995). On the hydrogen and oxygen content of marine phytoplankton. *Deep Sea Research, Part I*, 42(9), 1675–1680.
- Brown, P. J., McDonagh, E. L., Sanders, R., Watson, A. J., Wanninkhof, R., King, B. A., et al. (2021). Circulation-driven variability of Atlantic anthropogenic carbon transports and uptake. *Nature Geoscience*. <https://doi.org/10.1038/s41561-021-00774-5>
- Caínzos, V., Hernández-Guerra, A., McCarthy, G. D., McDonagh, E. L., Cubas Armas, M., & Pérez-Hernández, M. D. (2022). Thirty Years of GOSHIP and WOCE Data: Atlantic Overturning of Mass, Heat, and Freshwater Transport. *Geophysical Research Letters*, 49(4). <https://doi.org/10.1029/2021GL096527>
- Cunningham, S. A. (2005). *RRS "Discovery" Cruise D279, 04 Apr - 10 May 2004. A Transatlantic hydrography section at 24.5N. Cruise Report of the Southampton Oceanography Centre*. Southampton, UK.
- DeVries, T. (2014). The oceanic anthropogenic CO<sub>2</sub> sink: Storage, air-sea fluxes, and transports over the industrial era. *Global Biogeochemical Cycles*, 28(7), 631–647. <https://doi.org/10.1002/2013GB004739>
- DeVries, T., Holzer, M., & Primeau, F. (2017). Recent increase in oceanic carbon uptake driven by weaker upper-ocean overturning. *Nature*, 542(7640), 215–218. <https://doi.org/10.1038/nature21068>
- Fu, Y., Li, F., Karstensen, J., & Wang, C. (2020). A stable Atlantic Meridional Overturning Circulation in a changing North Atlantic Ocean since the 1990s. *Science Advances*, 6(48), eabc7836. <https://doi.org/10.1126/sciadv.abc7836>
- Ganachaud, A. S. (2003). Large-scale mass transports, water mass formation, and diffusivities estimated from World Ocean Circulation Experiment (WOCE) hydrographic data. *Journal of Geophysical Research*, 108(C7). <https://doi.org/10.1029/2002jc001565>
- Gruber, N., Clement, D., Carter, B. R., Feely, R. A., van Heuven, S., Hoppema, M., et al. (2019). The oceanic sink for anthropogenic CO<sub>2</sub> from 1994 to 2007. *Science*, 363(6432), 1193–1199. <https://doi.org/10.1126/science.aau5153>
- Jeansson, E., Olsen, A., Eldevik, T., Skjelvan, I., Omar, A. M., Lauvset, S. K., et al. (2011). The Nordic Seas carbon budget: Sources, sinks, and uncertainties. *Global Biogeochemical Cycles*, 25(4), GB4010. <https://doi.org/10.1029/2010GB003961>
- Johnson, K. M., Wallace, D. W. R., Wilke, R. J., & Goyet, C. (1995). *Carbon Dioxide, Hydrographic, and Chemical Data Obtained During the R/V Meteor Cruise 15/3 in the South Atlantic Ocean (WOCE Section A9, February - March 1991)*. ORNL/CDIAC-82, NDP-051. Carbon Dioxide Information Analysis Center, Oak Ridge National Laboratory, Oak Ridge, Tennessee. <https://doi.org/10.3334/CDIAC/otg.ndp051>
- Johnson, K. M., Schneider, B., Mintrop, L., Wallace, D. W. R., & Kozyr, A. (1998). *Carbon Dioxide, Hydrographic, and Chemical Data Obtained During the R/V Meteor Cruise 22/5 in the South Atlantic Ocean (WOCE Section A10, December-1992 January 1993)*. ORNL/CDIAC-113, NDP-066. Carbon Dioxide Information Analysis Center, Oak Ridge National Laboratory, U.S. Department of Energy, Oak Ridge, Tennessee.
- Johnson, K. M., Wills, K., Koertzing, A., Neill, C., & Wallace, D. W. R. (2002). *Carbon Dioxide, Hydrographic, and Chemical Data Obtained During the R/V Meteor Cruise 28/1 in the South Atlantic Ocean (WOCE Section A8, March 29 - May 12, 1994)*. ORNL/CDIAC-135, NDP-079. (A. Kozyr & T. W. Beaty, Eds.). Carbon Dioxide Information Analysis Center, Oak Ridge National Laboratory, U.S. Department of Energy, Oak Ridge, Tennessee.
- Macdonald, A. M., Baringer, M. O., Wanninkhof, R., Lee, K., & Wallace, D. W. R. (2003). A 1998–1992 comparison of inorganic carbon and its transport across 24.5°N in the Atlantic. *Deep Sea Research Part II: Topical Studies in Oceanography*, 50(22–26), 3041–3064. <https://doi.org/10.1016/j.dsr2.2003.07.009>
- Maze, G., Mercier, H., Thierry, V., Memery, L., Morin, P., & Perez, F. F. (2012). Mass, nutrient and oxygen budgets for the northeastern Atlantic Ocean. *Biogeosciences*, 9(10), 4099–4113. <https://doi.org/10.5194/bg-9-4099-2012>
- McDonagh, E. L. (2007). *RRS Charles Darwin Cruise CD171, 01 May - 15 Jun 2005. A trans-Atlantic hydrographic section at 36N* (Vol. Southampton).
- Mikaloff Fletcher, S. E., Gruber, N., Jacobson, A. R., Doney, S. C., Dutkiewicz, S., Gerber, M., et al. (2006). Inverse estimates of anthropogenic CO<sub>2</sub> uptake, transport, and storage by the ocean. *Global Biogeochemical Cycles*, 20(2), GB2002. <https://doi.org/10.1029/2005GB002530>

- Millero, F. J., Fiol, S., Campbell, D. M., Parrilla, G., Allison, L. J., & Kozyr, A. (2000). *Carbon Dioxide, Hydrographic, and Chemical Data Obtained During the R/V Hesperides Cruise in the Atlantic Ocean (WOCE Section A5, July 14 - August 15, 1992)*. ORNL/CDIAC-125, NDP-074. Carbon Dioxide Information Analysis Center, Oak Ridge National Laboratory, U.S. Department of Energy, Oak Ridge, Tennessee.
- Müller, J. D., Gruber, N., Zhu, D., Gregor, L., Carter, B., Pérez, F. F., et al. (2022). Decadal evolution of the oceanic sink for anthropogenic carbon from 1994 to 2014. *Ocean Science Meeting 2022*.
- Pérez, F. F., Mercier, H., Vázquez-Rodríguez, M., Lherminier, P., Velo, A., Pardo, P. C., et al. (2013). Atlantic Ocean CO<sub>2</sub> uptake reduced by weakening of the meridional overturning circulation. *Nature Geoscience*, 6(2), 146–152. <https://doi.org/10.1038/ngeo1680>
- Racapé, V., Zunino, P., Mercier, H., Lherminier, P., Bopp, L., Pérez, F. F., & Gehlen, M. (2018). Transport and storage of anthropogenic C in the North Atlantic Subpolar Ocean. *Biogeosciences*, 15(14), 4661–4682. <https://doi.org/10.5194/bg-15-4661-2018>
- Rosón, G. (2003). Carbon distribution, fluxes, and budgets in the subtropical North Atlantic Ocean (24.5°N). *Journal of Geophysical Research*, 108(C5), 3144. <https://doi.org/10.1029/1999JC000047>
- Sabine, C. L., Feely, R. A., Gruber, N., Key, R. M., Lee, K., Bullister, J. L., et al. (2004). The Oceanic Sink for Anthropogenic CO<sub>2</sub>. *Science*, 305(5682), 367–371. <https://doi.org/10.1126/science.1097403>
- Schuster, U., Watson, A. J., Bakker, D. C. E., de Boer, A. M., Jones, E. M., Lee, G. A., et al. (2014). Measurements of total alkalinity and inorganic dissolved carbon in the Atlantic Ocean and adjacent Southern Ocean between 2008 and 2010. *Earth System Science Data*, 6(1), 175–183. <https://doi.org/10.5194/essd-6-175-2014>
- Tanhua, T., Jones, E. P., Jeansson, E., Jutterström, S., Smethie, W. M., Wallace, D. W. R., & Anderson, L. G. (2009). Ventilation of the Arctic Ocean: Mean ages and inventories of anthropogenic CO<sub>2</sub> and CFC-11. *Journal of Geophysical Research*, 114(C1), C01002. <https://doi.org/10.1029/2008JC004868>
- Uchida, H., Fukasawa, M., & Murata, A. (2005). *WHP P6, A10, I3/I4 REVISIT DATA BOOK Blue Earth Global Expedition 2003 (BEAGLE2003)*. Volume 1,2. JAMSTEC Publication.
- Wunsch, C. (1996). *The Ocean Circulation Inverse Problem*. Cambridge, USA: Cambridge University Press.
- Zunino, P., Pérez, F. F., Fajar, N. M., Gualart, E. F., Ríos, A. F., Pelegrí, J. L., & Hernández-Guerra, A. (2015). Transports and budgets of anthropogenic CO<sub>2</sub> in the tropical North Atlantic in 1992-1993 and 2010-2011. *Global Biogeochemical Cycles*, 29(7), 1075–1091. <https://doi.org/10.1002/2014GB005075>